Computational Modeling of Droplet Impact Dynamics on Solid Substrates

Pratulya Rajan Saravanan Manikkam

Thesis submitted to the Faculty of the

Virginia Polytechnic Institute and State University

in partial fulfillment of the requirements for the degree of

Master of Science

in

Aerospace Engineering

Olivier Coutier-Delgosha, Chair

K. Todd Lowe

Eric G. Paterson

December 6, 2022

Blacksburg, Virginia

Keywords: Rebound, HRIC, VOF, Contact Angles

Computational Modeling of Droplet Impact Dynamics on Solid Substrates

Pratulya Rajan Saravanan Manikkam

ABSTRACT

A computational model is developed to simulate the impact dynamics of a droplet on solid substrates with the purpose of predicting the droplet spreading characteristics over time. Previous studies focused on finding relations between the impact parameters and outcome dynamics. A modified approach like the one used in this project revolves around modeling the moving contact lines at the interface in a multiphase flow environment. Focusing on research from an aircraft de-icing point of view, this study is considered a prerequisite in understanding the physics of droplet impact. The primary focus is on extending the application to incorporate super-cooled environments. Development of the model involved the use of the Volume-of-Fluid function coupled with the High-Resolution Interface Capturing scheme to model the moving contact line. The evolution of the moving contact line is modeled with contact angles as their inputs to understand the effect of the surface tension forces. Contact angle modeling is based on the Blended-Kistler method, which captures the contact angle evolution based on the surface tension and capillary number. Preliminary validation performed on the model proves its effectiveness in accurately simulating the impact behavior when compared to the literature, where the spread diameter and height agree well with experiments. The validated model is also compared to the in-house experiments performed at the Cavitation and Multiphase flow laboratory using different substrate materials. The substrates each show unique behavior - Impact on Glass results in the droplet depositing on the surface. Aluminum results in a full rebound and PET-G, results in a drop ejection.

Based on inputs from the experiments - contact angles, spread diameter, and the maximum spread β, show good agreement in comparison to the literature.

Computational Modeling of Droplet Impact Dynamics on Solid Substrates

Pratulya Rajan Saravanan Manikkam

GENERAL AUDIENCE ABSTRACT

Computational model developed to simulate the impact dynamics of the droplet on solid surfaces, which predicts the evolution of the droplet over time in order to analyze the effect of the surface and properties of the fluid on the behavior of the droplet on impact. Focusing on research from an aircraft de-icing point of view, this study is considered a pre-requisite in understanding the physics of droplet impact, with potential scope in extending the simulation to applications at temperatures lower than 0° C. A model developed with the help of basic governing equations in fluid mechanics helps capture the effect of interactions between different physical states. The angle at which the droplet interacts with the surface (Contact Angle) and the diameter evolution (d/D) help us understand the effectiveness of the model to simulate droplet impact. Preliminary validation of the model is performed with respect to the literature where the droplet diameter evolution and the height variation match well with the experiments, which was the major criterion in determining the accuracy of the model. This model is compared to the in-house experiments performed at the Cavitation and Multiphase flow laboratory on different surfaces such as Glass, Aluminum, and Plastic (PET-G). The surfaces each show unique behavior with impact on Glass having the droplet deposit on the surface, aluminum resulting in the droplet bouncing after hitting the surface, and PET-G resulting in a small droplet being ejected from the bigger droplet which eventually deposits on the surface. Conclusions from the comparison between the experiments and the numerical simulation show how the model is effective in capturing the impact behavior on

surfaces like glass in comparison to surfaces like Aluminum in this case that repels water.

This thesis is dedicated to my family and friends for their endless love, support and encouragement.

Acknowledgments

I would like to acknowledge the efforts of my parents and family, for supporting me throughout and providing me the opportunity to pursue my Master's in Aerospace Engineering.

I would like to express my deepest gratitude towards my advisor Dr. Olivier Coutier-Delgosha for funding me during the Summer of 2021, guiding me throughout the project, and providing me with great advice and insight into topics that were crucial in understanding the results.

I am extremely grateful to the members of my committee Dr. Todd K. Lowe and Dr. Eric G. Paterson for their promptness in response and for helping me finalize the project.

I wish to extend my special thanks to Joe Ghossein at the Cavitation and Multiphase Flow Laboratory (Virginia Tech), and Chinmay Kendurkar at the Aerospace Structures and Materials Laboratory (Virginia Tech) for assistance with conducting experiments and data collection that have been used in validating and development of the numerical model.

I could not have undertaken this journey without the financial support from the Department of Chemistry, which funded me for three semesters. I would like to extend my special thanks to Dr. John Morris, who provided me with the opportunity to be funded as a GTA.

Lastly, I wish to thank the Aerospace and Ocean Engineering Department and the Graduate School at Virginia Tech for technical support and assistance throughout the duration of my course. I would also like to show my appreciation to the professors for setting up challenging courses and helping me strengthen my concepts.

Contents

List of Figures xii

List of Tables xvi

List of Abbreviations xix

1 Introduction 1

1.1 Motivation 1

1.2 Literature Review 2

1.2.1 Experiments 3

1.2.2 Spreading and Receding Dynamics after Impact 5

1.2.3 Behaviour of Droplets on Splashing 9

1.2.4 Recent Efforts in Modeling Flows 10

1.3 Objectives 12

1.3.1 Setup and Verification of model based on prior experimentation . . . 13

1.3.2 Model Configurations 13

1.3.3 Model Test and Validation 14

2 Simulation of Impact Dynamics of Droplet 15

2.1 Introduction 15

2.2 Methodology 16

2.2.1 High-Resolution Interface Tracking (HRIC) 19

2.2.2 Contact Angle Modeling 22

2.3 Experimental Setup and Computational Domain 24

2.3.1 Experimental Setup 24

2.3.2 Computational Domain 25

2.4 Model Setup: Its physical parameters and constants 25

2.5 Chapter Summary 28

3 Verification and Preliminary Validation of Model **29**

3.1 Introduction 29

3.2 Model Comparison to Baseline Experiment 30

3.2.1 Introduction to Sikalo et al. Experiments 30

3.2.2 Baseline Experiments 30

3.2.3 Numerical Simulation 31

3.3 Methodology for parametric variation 36

3.3.1 Variation of CFL condition 36

3.3.2 Variation of Grid Refinement Level 38

3.4 Effect of varying CFL Condition 40

3.4.1 Qualitative Comparison 40

3.4.2 Quantitative Comparison 41

3.5 Effect of varying Grid Refinement Level 45

3.5.1 Qualitative Comparison 45

3.5.2 Quantitative Comparison 47

3.6 Chapter Summary 52

4 In-house experimentation and data acquisition 54

4.1 Introduction 54

4.2 Experiments 55

4.2.1 Experimental Set-up 55

4.2.2 Configurations 56

4.3 Data Acquisition 57

4.3.1 Methodology 57

4.3.2 Results 62

4.4 Chapter Summary 66

5 Numerical Simulation based on in-house experimentation 68

5.1 Introduction 68

5.2 Numerical Simulation results: Glass 68

5.3 Numerical Simulation Results: Aluminum plate 73

5.4 Numerical Simulation Results: PETG plate 79

5.5 Chapter Summary 84

6 Conclusion and Future Work **85**

6.1 Conclusion 85

6.2 Future Work 89

Bibliography **91**

Appendices **101**

Appendix A Simulation Set-up **102**

Appendix B Appendix B **112**

B.1 Mistakes to Avoid 112

List of Figures

1.1 Morphology of drop impact on a dry surface (From Rioboo, 2001) 4

1.2 Simulation behavior (right) and experimental image (left) during the receding phase of droplet impact Šikalo et al. [67] 8

2.1 Interface between two fluids and parameters used in HRIC scheme 20

2.2 Visualization of the contact line and contact angle θ used in determining the surface tension and wettability characteristics 22

2.3 Geometry of the domain 26

2.4 Different geometrical regions of the computational domain 26

3.1 Droplet impact evolution comparison between experiments (left) and simulation (right) 32

3.2 Comparison of time-varying experimental diameter ratio with numerical simulation and Sikalo's calculations 34

3.3 Comparison of time-varying experimental height ratio with numerical simulation 35

3.4 Visualization of the droplet evolution on impact for CFL Condition number 0.1 40

3.5 Visualization of the droplet evolution on impact for CFL Condition number 0.4 40

3.6 Visualization of the droplet evolution on impact for CFL Condition number 0.8 41

3.7 Droplet diameter ratio evolution over time compared to baseline experiment for different CFL Condition Numbers(CN) 42

3.8 Droplet Height Ratio evolution over time compared to baseline experiment for different CFL Condition Numbers (CN) 44

3.9 Visualization of the droplet meshing at the different refinement levels at time 0ms 46

3.10 Zoomed in view of initial droplet meshing at the interface for refinement level 2 (left) and refinement level 5 (right) 47

3.11 Mesh size evolution over non-dimensional time for different refinement levels 48

3.12 Time-Step size evolution over non-dimensional time for different refinement levels 49

3.13 Mesh size and time-step size plot comparison showing the phases of the droplet impact varied over time τ 50

3.14 Evolution of the Droplet diameter ratio over non-dimensional time for different refinement levels compared with the baseline experiments 51

4.1 Experimental Setup from Multiphase Flow Lab (right) and experimental setup schematic as seen in Roisman [43] (left) 55

4.2 Droplet Diameter measurement tool using image processing 58

4.3 Experimental ACA/RCA and stagnant contact angle measurement setup . . 59

4.4 Experimental ACA/RCA and stagnant contact angle measurement setup* . 60

4.5 Measurement of contact angle of experimental data using image processing tool as an alternative method 61

4.6 Droplet evolution on glass substrate observed in experiments 64

4.7 Droplet evolution on coated aluminum substrate observed in experiments . . 65

4.8 Droplet evolution on PET-G substrate observed in experiments 67

5.1 Droplet evolution regime based on numerical simulation on glass substrate compared with the experiments at similar time intervals 69

5.2 Diameter evolution comparison between in-house experiment and numerical simulation for glass substrate 70

5.3 Contact Angle evolution comparison between in-house experiment and numerical simulation for glass substrate 71

5.4 Droplet evolution regime based on numerical simulation on aluminum substrate compared with the experiments at similar time intervals 74

5.5 Diameter evolution comparison between in-house experiment and numerical simulation for aluminum substrate 75

5.6 Contact Angle evolution comparison between in-house experiment and numerical simulation for aluminum substrate 77

5.7 Droplet evolution regime based on numerical simulation (color) on PET-G substrate compared with the experiments (grayscale) at similar time intervals 79

5.8 Diameter evolution comparison between in-house experiment and numerical simulation for PET-G substrate 80

5.9 Contact Angle evolution comparison between in-house experiment and numerical simulation for PET-G substrate 82

A.1 Image showing the tree for geometry of the model 103

A.2 Image showing the different input parameters required in defining the drop zone 104

A.3 Image showing the different input parameters required in defining the splash zone 104

A.4 Image showing the different steps in setting up the model 105

A.5 Image shows the setup for an adaptive mesh model 105

A.6 Image shows the setup for an adaptive time-step model 106

A.7 Image shows the setup for the multiphase equation of state model 106

A.8 Image shows the setup for the volume of fluid model 107

A.9 Image shows the definition of the reference parameters 107

A.10 Image shows the definition of the initial conditions 108

A.11 Image shows the definition of the contact angle modeling 108

A.12 Image shows the definition of the thresholds defined in the derived parts . . 109

A.13 Image shows the definition of the VOF and multi-stepping methods 109

A.14 Image shows the definition of the droplet parameters 110

A.15 Image shows the definition of the maximum inner iterations as part of the stopping criterion 110

List of Tables

1.1 Models from literature for Spread factor β as function of non-dimensional impact parameters 6

1.2 Classification and the general trend of impact parameters observed for different impact scenarios [62] 11

2.1 Boundary Conditions for the Computational Domain 25

2.2 Material Properties 27

2.3 HRIC Scheme Parameters 27

3.1 Experimental parameters for droplet sized 2.45mm 31

3.2 Simulation input parameters 31

3.3 Stopping criterion used in simulation setup 32

3.4 Modeling parameters for numerical simulation setup for vary CFL Conditions 37

3.5 Modeling parameters for numerical simulation setup for vary CFL Conditions 39

3.6 Absolute percentage error comparison of Numerical diameter and height data with experimental diameter and height for varying CFL Condition numbers . 45

3.7 Variation of the cell count at time t=0 ms, for different refinement levels . . 48

3.8 Numerical error percentage for droplet diameter evolution from simulation compared to the baseline experiment 52

4.1 Experimental cases with materials properties 56

4.2 Camera common configurations used in data acquisition 57

4.3 Droplet behaviors observed on substrates of different materials 62

4.4 Uncertainty quantification of experimental data taken with respect to measurement on the three different materials 63

4.5 Percentage uncertainty of experimental data taken with respect to measurement on different materials 63

4.6 Impact parameters results obtained from experiments for glass 64

4.7 Impact parameters results obtained from experiments for aluminum 65

4.8 Impact parameters results obtained from experiments for PET-G 66

5.1 Non-Dimensional parameters evaluated to calculate the maximum spread rates 72

5.2 Different maximum spread (β) rate empirical models from the literature compared to the maximum spread rate from numerical simulation 72

5.3 Non-Dimensional parameters evaluated to calculate the maximum spread rates 78

5.4 Different maximum spread rate(β) empirical models from the literature compared to the maximum spread rate from numerical simulation 78

5.5 Non-Dimensional parameters evaluated to calculate the maximum spread rates for PET-G substrate 81

5.6 Different maximum spread rate(β) empirical models from the literature compared to the maximum spread rate from numerical simulation for PET-G substrate 82

6.1 Wall-time variation of the simulation case for different CFL numbers 86

6.2 Wall-time variation of the simulation case for different refinement levels . . . 86

List of Abbreviations

ACA Advancing Contact Angle

CA Contact Angle

CFD Computational Fluid Dynamics

CFL Courant Freidrich-Lewy

CN Condition Number

DI Diffusion Interface

FOU First Order Upwiniding

FT Front Tracking

GR Grid Refinement

HRIC High Resolution Interface-Capturing

LS Level-Set

MCL Moving Contact Line

RCA Receding Contact Angle

SLD Super-cooled Large Droplets

VOF Volume of Fluid

Chapter 1

Introduction

1.1 Motivation

There has been extensive research in the field of droplet dynamics, its impact, and its characteristics for solving higher-order problems, one such problem is the icing hazards encountered by aircraft flying at higher altitudes. Moisture in the air condenses to form droplets that are found to freeze on the surfaces of an aircraft, causing hazardous effects on aircraft wings, fuselages, and control surfaces.

By studying the impact dynamics of droplets, the physics behind the expanding and receding phases of the impact dynamics can be understood with various different approaches as mentioned by et. al, in this case, the contact angle method. Experiments can be performed to simulate the impact of a droplet on different surfaces to identify its spreading rate, wettability of the surface, and roughness characteristics to predict the behavior of the droplet in different environments.

For the purpose of validating the experiments and understanding the behavior numerically, calculations can be performed with the help of Computational Fluid Dynamics - whilst varying the different numerical parameters such as the time-step, Courant-Freidrich Lewy (CFL) number, mesh refinement, etc.

Current solutions involve the use of liquids which is usually heated solutions of glycol-water

that are sprayed before take-off, the secondary gel-like substance which is a mixture named propylene-glycol having a freezing temperature well below 0 degrees Celsius, remains on the surfaces until take-off. In commercial aircraft, there are tubes that extend through the length of the fuselage and wings which supply heat in the form of air that is bled through the aircraft engines, which provide sufficient heat in-order to melt ice. All these methods consist of major drawbacks with regard to their effectiveness (de-icing fluids are temporary solutions) and efficiency (heated tubes reduce the aircraft's overall efficiency by including air from the turbine and increasing the overall weight of the aircraft).

The industry seeks newer methods, with extensive research going on in this field, one such way includes the identification of surface properties such as roughness to generate hydrophobic surfaces that will prevent the accretion of ice on wings by dispersing the moisture, another novel approach may involve the use of piezoelectric sensors to generate vibrations at low amplitudes in-order not to induce stress on the aircraft surfaces.

1.2 Literature Review

The study of droplet impact on solid surfaces has been on for decades and early studies involve conclusions on the significance of the impact velocity, size of the droplet, and relative direction. These observations are made based on the properties of the liquid such as density, viscosity, and various other non-newtonian effects for complex fluids along with surface properties such as wettability, roughness, and non-isothermal effects such as evaporation, condensation, etc, to determine the impact dynamics. To effectively determine a governing model and understand the dynamic effects, the following dimensionless parameters are defined:

$$We = \frac{\rho D V_0^2}{\sigma} \qquad \text{(Weber No.)} \tag{1.1}$$

$$Re = \frac{\rho D V_0}{\mu} \qquad \text{(Reynolds No.)} \tag{1.2}$$

$$Oh = \frac{\mu}{(\rho \sigma D)^{0.5}} \qquad \text{(Ohnesorge No.)} \tag{1.3}$$

$$Bo = \frac{\rho g D^2}{\sigma} \qquad \text{(Bond No.)} \tag{1.4}$$

$$Ca = \frac{V \mu}{\sigma} \qquad \text{(Capillary No.)} \tag{1.5}$$

$$Fr = \frac{V_0^2}{gD} = \frac{We}{Bo} \quad \text{(Froude No.)} \tag{1.6}$$

where, ρ,μ,σ denote the liquid density, dynamic viscosity, and surface tension, respectively, D and V_0 the drop diameter and impact velocity, respectively.

1.2.1 Experiments

In 2001, Rioboo et al. [41] conducted a set of experiments for droplet impact on drywall, with outcomes including deposition, droplet splashing, corona splash, receding break-up, partial rebound, and a complete rebound, as seen in Fig.1.

In a continued study, Rioboo et al. [40] made observations on the deposition of droplets and determined its two phases: the kinematic and deposition phase, during the kinematic phase the non-dimensional time $\tau(\equiv \mathrm{t}V_0/\mathrm{D})$ <0.1, the radius of the base of the droplet was proportional to $\sim t^{1/2}$, independent of the physical properties of the liquid and surface, however, the liquid and surface properties play a role in the deposition stage. The author does not provide the reason for why τ<0.1 was chosen to be the time of transition between the two phases. Sikalo et al. [51] in 2002, performed similar experiments and concluded that

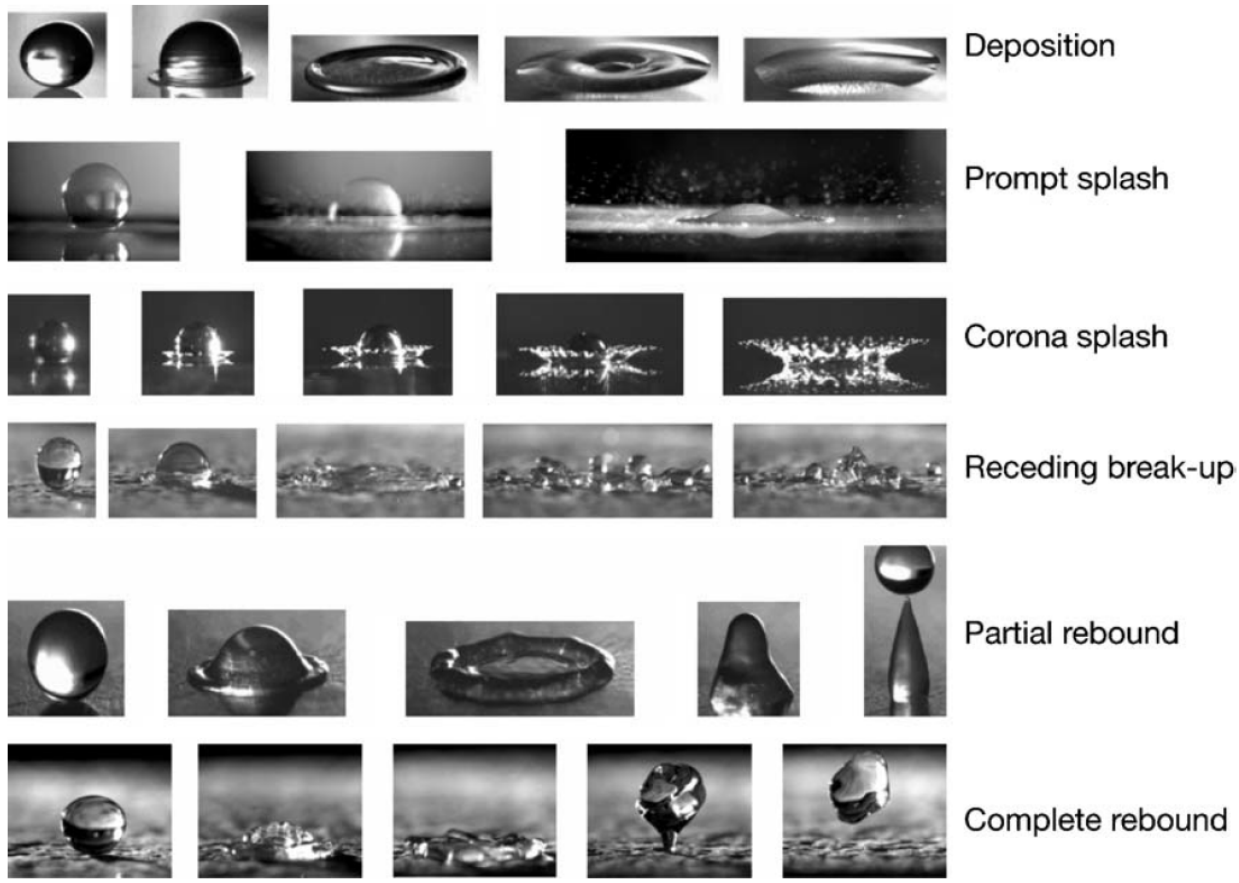

Figure 1.1: Morphology of drop impact on a dry surface (From Rioboo, 2001)

for a simple deposition (with no rebound or receding phase), for lower impact velocities, the maximum spread factor of the droplet base ranged from 1.25 to 5, i.e., $1.25 \leq (\beta = 2R_{max}/D) \leq 5$. These experimental results agree well with a prior empirical model proposed by Scheller and Bousfield [47] where:

$$\beta = 0.61(Re^2 Oh)^{0.166} = 0.61(\frac{We}{Oh})^{0.166} \tag{1.7}$$

1.2.2 Spreading and Receding Dynamics after Impact

During the kinematic stage, a major fraction of the kinetic energy in the droplet is dissipated, and when there is no splashing - the behavior of the droplet is believed to be dependent on the surface properties such as wettability and roughness Bayer and Megaridis [4], Yokoi et al. [65] and non-isothermal effects Yarin [62] with smooth spreading or receding, the breakup of tiny droplets during receding and rebounding as possible outcomes of impact. The maximum spread factor (β) is one of the major parameters that researchers try to correlate with the different drop parameters. Most research focused on droplet impact on solid substrates from 1990 to 2010 focuses on the correlation of the Maximum Spread Factor, as seen in Rioboo et al. [40], Roisman et al. [44], Roisman [43], Eggers et al. [16], Chandra and Avedisian [8], Pasandideh-Fard et al. [33], Range and Feuillebois [35], Clanet et al. [11], Fedorchenko et al. [17], Ukiwe and Kwok [56], Vadillo et al. [57]. The empirical relations proposed for the Maximum Spread Diameter are summarized in Table 1.1.

All the models proposed in table 1.1. are known to show reasonable agreement with experimental data or numerical simulations presented by the authors. As observed by most researchers, for a varied range of impact velocities, it is difficult to differentiate between the various scaled equations presented in table 1.1. At higher impact velocities, splashing occurs, hence no relation can be identified in this phase. However, most models have differentiated between the two phases (viscous and inertial) for β, wherein the viscous regime, the maximum value of β can be obtained by balancing the viscous dissipation with the kinetic energy ($\beta \propto Re^{1/5}$). In the inertial regime, the maximum value of β is estimated by a complex relationship between inertia and capillary forces with a correction factor due to the viscous dissipation and effect of wettability. Models in the inertial regime involve the use of the Weber number instead of the Reynolds number. Newer research is focused on the time evolution of the boundary layer between the liquid and the substrate (moving contact line), as

Table 1.1: Models from literature for Spread factor β as function of non-dimensional impact parameters

Model	Expression	Details
Scheller & Bousfield(1995)	$\beta \sim 0.61(Re^2Oh)^{1/6}$ $= 0.61Re^{1/5}(WeRe^{-2/5})^{1/6}$	Empirical law from experimental results
Pasandideh-Fard et al. (1996)	$\beta = \sqrt{\frac{We+12}{3(1-cos\theta_a+4(\frac{We}{\sqrt{Re}})}}$	Energy balance with contact angle
Ukiwe & Kwok (2005)	$(We+12)\beta =$ $8+\beta^3\left(3(1-cos\theta_d)+4\frac{We}{\sqrt{Re}}\right)$	Extension of above model, with spreading dynamic contact angle
Clanet et al. (2004)	$\beta \propto We^{1/4}$	Impact capillary length used for mass balance
Roisman (2009)	$\beta \sim 0.87Re^{1/5}$ $-0.4Re^{2/5}We^{-1/2}$	Viscous boundary layer dynamic model used to predict droplet spreading
Eggers et al. (2010)	$\beta = Re^{1/5}f(P)$	Similar to Roisman's $P = WeRe^{-2/5}$, approach; is the impact number

researchers believe an understanding of this dynamic would be able to resolve the difference between the empirical relations in the viscous and inertial regimes, and lay down a basis to work on more advanced impact techniques (angled impacts, inclusion of non-isothermal effects such as a super-cooled droplet or substrate to simulate an icing environment). The velocity of the moving contact line and the dynamic contact angle plays a significant role

in determining the characteristics of the receding phase Roisman et al. [42], Marengo et al. [28], Snoeijer and Andreotti [52], Sui and Spelt [55], Gordillo et al. [18], for which effective methods can be modeled based on different cases.

During the spreading phase (when there is no splashing), as the droplet expands to its maximum diameter, in the case of millimeter-sized droplets, the contact line starts receding after a short interval (order of milliseconds) as mentioned by Yarin [62].

Depending on the impact velocity, the droplet takes a circular shape (like a doughnut) - where the liquid is concentrated at the rims of the droplet or gets stretched out to form a very thin but uniform lamella in the center. Rioboo et al. [40] proposed that the maximum and minimum diameter of the droplet could be defined for a given volume of the droplet, as:

$$\frac{d_i}{D} = 2[\frac{sin^3\theta_i}{2(1-cos\theta_i)(2-cos\theta_i-cos^2\theta_i)}]^{1/3} \tag{1.8}$$

where $d_i = d_a$ (max. diameter) corresponds to $\theta_i = \theta_{adv}$ (average advancing contact angle) and $d_i = d_r$ (minimum diameter) corresponds to $\theta_i = \theta_{rec}$ (average receding contact angle). The above equation 1.8 is valid only for low impact velocities as for higher impact velocities the higher kinetic energy forces the droplet to spread beyond d_a and recede to a magnitude lower than d_r (in cases of no splash). If the surface is non-wettable ($\theta_{adv} \rightarrow 180°$) Rioboo et al. [40], during the receding phase, the droplet leaves some tiny droplets behind as the lamella breaks up into a number of fingers with each of them having the ability to break-up further due to capillary instability Yarin [62].

Once the droplet reaches its maximum spread diameter, the rim of the spreading droplet starts to recede, the kinetic energy that was not dissipated during impact, causes the droplet to have a high receding velocity. This causes the inner rims of the droplet to collide at its center leading to an upward motion of the liquid, resulting in a phenomenon known as

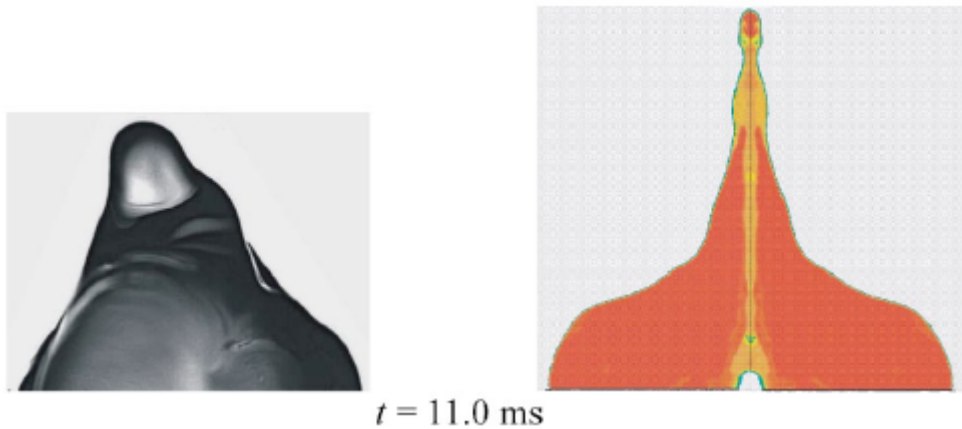

Figure 1.2: Simulation behavior (right) and experimental image (left) during the receding phase of droplet impact Šikalo et al. [67]

jetting, seen in figure 1.2. It has been observed in many studies conducted on droplet impact on solid substrates, mainly by Šikalo et al. [67] and Roisman et al. [42]. Schiaffino and Sonin [48] observed that jetting can lead to a complete rebound on hydrophobic surfaces due to the momentum of the spreading droplet after impact.

Different results can be obtained by modifying the surface properties of the substrate (adding roughness patterns, holes, coatings to vary wettability, etc.), by varying the outcomes of droplet impact, studies can be correlated to support applications such as prevention of icing of aircraft components, enhancing heat-transfer processes, etc as observed in literature by Reyssat et al. [38], Schutzius et al. [49], Brunet et al. [7], Lee et al. [23], Sahu et al. [46], Liu and Kim [25], Bird et al. [5], Moevius et al. [29], Yeong et al. [63]. These surface properties can be achieved with the help of new additive micro- and nano-fabrication techniques, with various patterns and substrates of varied roughness implemented throughout this study.

1.2.3 Behaviour of Droplets on Splashing

Droplets with higher impact velocities tend to be subjected to the phenomenon of splashing, considering velocities below 30m/s as the compressibility effects become dominant at this stage as noted by Pros and Oguz [34] and Li and Thoroddsen [24]. Droplets mainly undergo two types of splashing, depending on the surface tension and roughness characteristics, during the kinetic stage. In cases of high surface roughness, which corresponds to higher surface tension between the liquid and the substrate, the majority of the droplet is subject to remain on the substrate wall observed by Xu et al. [61], only minuscule droplets at the periphery of the liquid lamella tend to break up and detach from the bigger droplet, since the kinetic energy is at the periphery is large enough to overcome the internal cohesion forces of the liquid droplet. The other type of splashing behavior occurs when the surface tension between the liquid and the substrate is lower, resulting in the ability of the liquid lamella to detach from the substrate wall, which results in a phenomenon called the Corona splash as observed in figure 1.1. This splashing phenomenon can be suppressed by the reduction in pressure of the surrounding medium (gas), as found by Xu et al. [60]. Mundo et al. [30] characterized a parameter to determine a threshold for the splashing of a droplet when impacted on a solid substrate under normal atmospheric conditions, the parameter known as the splashing parameter:

$$K = We^{0.5}Re^{0.25} \tag{1.9}$$

In which the threshold for the splashing parameter K = 657.48, after which splashing behavior is observed. Cossali et al. [12], came up with a different relation for the splash parameter, where:

$$K = 649 + 3.76/R_{nd}^{0.63} \tag{1.10}$$

Recently, more studies have focused on finding this critical value for K, while considering different impact scenarios to determine the underlying mechanism of a droplet splash. However, even to date, no such unified model exists (Wal et al. [58], Roisman et al. [45]). Many researchers believed that a unified model cannot exist due to the randomness in the roughness characteristics of the substrate material being used. Current studies are focused on finding the cause for the levitation of the tip of the lamella as the droplet spreads along the substrate, which is one of the uncertainties that need to be eliminated to focus on the main parameters that might affect the outcome of a droplet splashing (Latka et al. [22], Stevens [54], Riboux and Gordillo [39], Liu and Kim [25]). A generalized trend of droplet impact outcomes can be summarized as follows in table 2:

1.2.4 Recent Efforts in Modeling Flows

In recent times, the focus in droplet research has shifted from finding a relation between the impact parameters and outcome dynamics to modeling the moving contact lines in the multiphase flow environment (2 phases), using a wide range of continuum surface models (Bonn et al. [6], Snoeijer and Andreotti [52], [50]). These Moving Contact Line (MCL) models can be coupled with different Computational Fluid Dynamics (CFD) methods, either finite-volume (Afkhami and Bussmann [1], Dupont and Legendre [15], Josserand et al. [21], Renardy et al. [37] Renardy et al. 2001) or finite-element methods (Bao et al. [3], Christodoulou and Scriven [10], Hadjiconstantinou and Patera [19], Lowndes [26], [59]) to specify the boundary conditions at the solid walls which determine the evolution of the interface and velocity fields instead of restricting it to a certain type of wetting condition with constant dynamic contact angles, done to simulate the multiphase flow that governs the droplet impact dynamics. With new MCL models being implemented, current studies are getting closer to understanding the mechanism of droplet impact dynamics, to accurately

Table 1.2: Classification and the general trend of impact parameters observed for different impact scenarios [62]

Parameter Increase	Deposition	Prompt splash	Corona splash	Receding breakup	Partial rebound	Complete rebound
$\mathbf{V_0}$	↓	↑	↑	↑	↑	
$\mathbf{D}$	↓	↑				
$\boldsymbol{\sigma}$		↓	↓	↑	↑	↑
$\boldsymbol{\mu}$	↑	↓	↓	↓		
$\mathbf{R_a}$	↓	↑	↓			
$\mathbf{R_w}$		↓				
$\boldsymbol{\theta_{rec}}$			↑	↑	↑	

simulate different types of impacts, which can provide solutions to solving complex problems that involve such phenomena such as preventing the formation of ice on aircraft, industrial paint coating, inkjet printing, etc. Some combinations of MCL and CFD methods being recently proposed have an acceptable level of accuracy when compared to experimental data, these methods include Level-Set (LS), Volume-Of-Fluid (VOF), Front Tracking (FT), and diffuse interface (DI) methods.

For Level-Set (LS) method, a signed function $\psi(x,t)$ is used to capture the interface between the moving fluid and the wall, whose sign is distinguished between two phases. The method

itself is not new. However, due to its simplicity, LS has recently been implemented coupled with different MCL models such as slip and static contact angle (Chen et al. [9], Ding and Spelt [14], Spelt [53] Sui and Spelt [55]), kinetic model (Deganello et al. [13]), and macroscale model with contact angle hysteresis (Park and Kang [32], [53]) to simulate the impact dynamics.

For Volume-Of-Fluid (VOF) method, a volume fraction function is used to track the interface position. Recent development in VOF methods allow it to be coupled with the MCL model to simulate droplet impact outcome (Josserand et al. [21], Yokoi [64]) or spreading/receding dynamic (Afkhami et al. [2], Dupont and Legendre [15], Renardy et al. [36]) where theoretical works and example simulations are provided. Despite different possible MCL models being utilized the, VOF method commonly imposes a gradient of volume fraction at the contact line as a function of contact angle.

In more recent studies, methods such as the Front-Tracking and Diffuse Interface have become popular. Front -Tracking involves incorporating dynamically varying or macroscale contact angles to model the MCL (Manservisi and Scardovelli [27], Muradoglu and Tasoglu [31]). Whereas, the Diffuse Interface replaces the mathematical interface with a finite thickness interface whose evolution involves a dissipative term to maintain the profile of the interface. There are a variety of MCL models that have been derived to specify the boundary conditions for the diffuse interface method (Ding and Spelt [14], Yue and Feng [66]) which have shown promising results.

1.3 Objectives

Droplet Impact Dynamics is a well-researched field, ongoing studies focus on understanding the significance of contact angles and MCLs to understand droplet behavior after impact.

For ice accretion or de-icing on aircraft, as a pre-requisite, more research must be focused on the physics of the droplet impact and nucleation phases. This thesis aims at understanding the behavior of droplets on impact from a computational simulation point of view, with the help of VOF and Contact angle modeling, validated with prior experiments from (Šikalo et al. [67]) and compared to experimental results obtained from the Cavitation and Multiphase flow lab at Virginia Tech.

1.3.1 Setup and Verification of model based on prior experimentation

The first phase of the project involves the development of a setup for a computational model that will work on predicting the droplet impact dynamics. This model will be verified with the experiments performed in Šikalo et al. [67], due to its similarity with the experimental set-up in the multiphase flow laboratory at Virginia Tech. The experiments by Šikalo et al. [67] do not take into account cases with droplet rebound or jetting behavior. Hence, the experimental results from the Multiphase Flow laboratory are valuable for validating the accuracy of the model.

1.3.2 Model Configurations

Once the basic setup of the model is concluded, the study of its distinct numerical parameters is conducted. Since the calculation being performed is implicit, the number of inner iterations is fixed, along with the convergence criterion for the residual equations.

Apart from these parameters, two key parameters affect the simulation more significantly than the others. The Courant-Friedrichs-Lewy Condition Number (CFL) and the Grid Refinement (GR) level are these key parameters, which will be the main focus of Chapter 3.

1.3.3 Model Test and Validation

The final objective involves Testing the model with different morphology of droplet dynamics, such as deposition, rebounding, and ejection.

Experiments performed in the multiphase flow laboratory provide the experimental data for cases with different solid substrate materials, as a consequence having different wettability and contact angles. Chapter 4 will focus on this objective where plates of substrate materials such as Glass, Aluminum, and PETG are experimented upon, depicting different impact behavior such as deposition, partial or complete rebound, and jetting, respectively.

Chapter 2

Simulation of Impact Dynamics of Droplet

2.1 Introduction

This chapter will talk about the governing equations and solver configuration that is used in the development of the HRIC-contact angle-based model for the simulation of droplet impact dynamics on StarCCM+. Numerical Simulation of droplet impact on solid substrates has been an ongoing research topic with the focus shifting towards modeling the moving contact line (Afkhami and Bussmann [1], Dupont and Legendre [15], Josserand et al. [21], Renardy et al. [36]).

One such proven method to simulate droplet impact is the Volume-of-Fluid method as described in section 1.2.4, this method involves the use of a volume fraction function to track the interface position and allows coupling with the MCL model to simulate droplet impact outcomes. In 1981, Hirt and Nichols came up with this interface boundary tracking method i.e., the Volume-of-fluid method that is still being used in modeling moving boundaries for immiscible fluids, in this case, air and liquid media.

2.2 Methodology

The governing equations form the basis of the VOF function algorithm. The in-compressible formulation for the Navier-Stokes equations is depicted in cartesian coordinates for the three-dimensional flow:

Continuity Equation

$$\frac{\partial p}{\partial t} + \frac{\partial(\rho u)}{\partial x} + \frac{\partial(\rho v)}{\partial y} + \frac{\partial(\rho w)}{\partial z} = 0 \tag{2.1}$$

x-momentum

$$\frac{\partial(\rho u)}{\partial t} + \frac{\partial(\rho u^2)}{\partial x} + \frac{\partial(\rho uv)}{\partial y} + \frac{\partial(\rho uw)}{\partial z} = -\frac{\partial p}{\partial x} + [\frac{\partial}{\partial x}(\mu\frac{\partial u}{\partial x}) + \frac{\partial}{\partial y}(\mu\frac{\partial u}{\partial y}) + \frac{\partial}{\partial z}(\mu\frac{\partial u}{\partial z})] + S_u \tag{2.2}$$

y-momentum

$$\frac{\partial(\rho v)}{\partial t} + \frac{\partial(\rho uv)}{\partial x} + \frac{\partial(\rho v^2)}{\partial y} + \frac{\partial(\rho vw)}{\partial z} = -\frac{\partial p}{\partial y} + [\frac{\partial}{\partial x}(\mu\frac{\partial v}{\partial x}) + \frac{\partial}{\partial y}(\mu\frac{\partial v}{\partial y}) + \frac{\partial}{\partial z}(\mu\frac{\partial v}{\partial z})] + S_v \tag{2.3}$$

z-momentum

$$\frac{\partial(\rho w)}{\partial t} + \frac{\partial(\rho uw)}{\partial x} + \frac{\partial(\rho vw)}{\partial y} + \frac{\partial(\rho w^2)}{\partial z} = -\frac{\partial p}{\partial z} + [\frac{\partial}{\partial x}\left(\mu\frac{\partial w}{\partial x}\right) + \frac{\partial}{\partial y}(\mu\frac{\partial w}{\partial y}) + \frac{\partial}{\partial z}(\mu\frac{\partial w}{\partial z})] + S_w \tag{2.4}$$

where, the density of the fluid is defined as 'ρ', fluid velocity in x,y and z-direction are defined as 'u','v', and 'w' respectively, with pressure defined as 'p', and viscosity defined as 'μ'. 'S_u', 'S_v', and 'S_w', are the source terms that consist of the contributions from the surface tension force.

The VOF method is solved using the one-fluid formulation approach, where the continuity

and momentum equations are solved with a 1-D system in the whole domain in the presence of two phases.

In this approach, a term consisting of the volume fraction is introduced. The magnitude of this volume fraction determines the type of fluid present in the interface and is considered the most crucial parameter in determining the interface characteristics. The volume fraction for an interface 'i' is given as the ratio of the volume of phase 'i' in the cell to the actual volume of the cell.

$$\alpha_i = \frac{V_i}{V} \tag{2.5}$$

Thus, the cumulative volume fraction of the phases can be defined as:

$$\sum_{i=1}^{N} \alpha_i = 1 \tag{2.6}$$

where N defines the number of phases.

The phase contribution from the various different liquids can be determined by the magnitude of the volume fraction:

- $\alpha_i = 0 \Rightarrow$ phase i does not exist in cell
- $\alpha_i = 1 \Rightarrow$only phase i exists in the cell
- $0 < \alpha_i < 1 \Rightarrow$ depicts the presence of an interface in the cell The simplified governing equations can be given as:

Continuity:

$$\frac{\partial p}{\partial t} + \nabla.(\rho u) = 0 \tag{2.7}$$

The source term 'S' present in equations 2.2, 2.3 and 2.4 can be defined as the function of the surface tension force:

$$S_i = \sigma\kappa\eta + \nabla_s\sigma \tag{2.8}$$

This equation can be further broken down to derive the effect of the surface tension force in the bulk volume in comparison to the force acting in the interface.

For a constant surface tension force acting across the volume:

$$\nabla_s\sigma = 0 \tag{2.9a}$$

Therefore, equation 2.8 becomes:

$$S_i = \sigma\kappa\eta \tag{2.9b}$$

Momentum:

$$\rho\left(\frac{\partial u_i}{\partial t} + u_j\frac{\partial u_i}{\partial x_j}\right) = -\frac{\partial \rho}{\partial x_j} + \frac{\partial}{\partial x_j}\left[\mu\left(\frac{\partial u_i}{\partial x_j} + \frac{\partial u_j}{\partial x_i}\right)\right] + S_i \tag{2.10a}$$

Using equation 2.9, we get:

$$\rho\left(\frac{\partial u_i}{\partial t} + u_j\frac{\partial u_i}{\partial x_j}\right) = -\frac{\partial \rho}{\partial x_j} + \frac{\partial}{\partial x_j}\left[\mu\left(\frac{\partial u_i}{\partial x_j} + \frac{\partial u_j}{\partial x_i}\right)\right] + \sigma\kappa\eta \tag{2.10b}$$

The volume fraction can be defined as a function of the continuity equation where the density function is replaced with the volume fraction in the cell:

$$\frac{\partial \alpha}{\partial t} + \nabla.(\alpha u) = 0 \tag{2.11}$$

The corresponding density and viscosity relations are calculated as functions of the volume fraction:

Density:

$$\rho(\overline{\alpha}) = \overline{\alpha}\rho_1 + (1 - \overline{\alpha})\rho_2 \tag{2.12}$$

where ρ_1 and ρ_2 are the densities of liquids phase 1 and phase 2 respectively.

Viscosity:

$$\mu(\overline{\alpha}) = \overline{\alpha}\mu_1 + (1 - \overline{\alpha})\mu_2 \tag{2.13}$$

The VOF function is solved as a system of these equations in order to track the interface as seen in fig. 2.1. For the solution of the VOF function, general interface capturing schemes are used, as discussed in the literature. StarCCM+ utilizes a unique interface tracking scheme known as the High-Resolution Interface Capturing (HRIC) method that is efficient in predicting the convective transport of interfacial fluids that are immiscible, thereby tracking sharp interfaces.

2.2.1 High-Resolution Interface Tracking (HRIC)

This HRIC scheme operates on the normalized variable diagram (NVD), where the face value of the volume fractions is normalized and calculated such as:

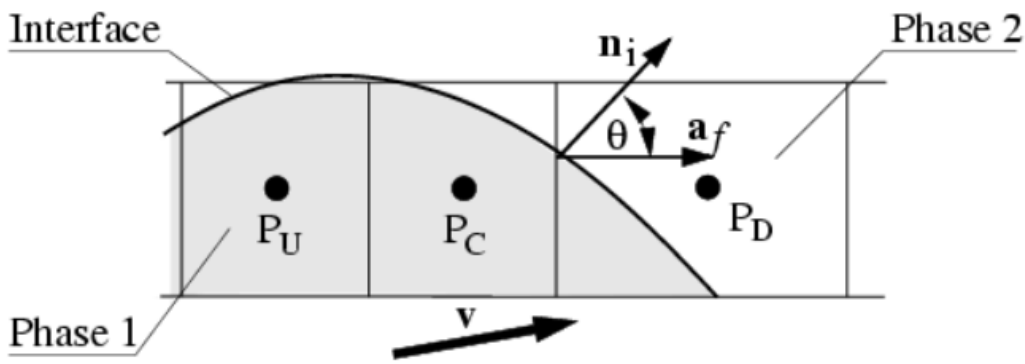

Figure 2.1: Interface between two fluids and parameters used in HRIC scheme

$$\zeta_f = \begin{cases} \zeta_C, & \text{if } \zeta_C < 0 \\ 2\zeta_C, & \text{if } 0 \leq \zeta_C < 0.5 \\ 1, & \text{if } 0.5 \leq \zeta_C < 1 \\ \zeta_C, & \text{if } 1 \leq \zeta_C \end{cases} \tag{2.14}$$

The local courant number in the cell is used as the correction factor for ζ_f :

$$Co = \frac{v.a_f}{V}\delta t \tag{2.15}$$

where a_f is the cell surface vector and V is the volume of the phase-corrected cell.

According to the one-fluid approach, the fluid that is transported into the adjacent cell during a time-step is less than or equal to the donor cell fluid volume. These corrections are made based on the following conditions:

$$\zeta_f^* = \begin{cases} \zeta_f, & \text{if } Co < Co_l \\ \zeta_C + (\zeta_f - \zeta_C)\,\frac{Co_u - Co}{Co_u - Co_l}, & \text{if } Co_l \leq Co < Co_u \\ \zeta_C, & \text{if } Co_u \leq Co \end{cases} \tag{2.16}$$

Correction factor ζ_C is evaluated for the 3 different cases of the Courant correction number. Coupling of First-Order Upwinding (FOU) and HRIC schemes are used based on the correction condition. This allows for a much more smooth interface capturing and avoids the sharp edges when re-creating the flow using the VOF function.

As seen in figure 2.1, the angle θ is an important factor that must be considered in interface tracking and the movement of the contact line. The final correction in this normalized face value for the volume fraction can be given as:

$$\zeta_f^{*^*} = \zeta_f^*(cos\theta)^{C_\theta} + \zeta_C\left(1 - (cos\theta)^{C_\theta}\right) \tag{2.17}$$

The default value for this angle factor C_θ is 0.05. Considering a free-surface condition the HRIC scheme volume fraction can be expressed as a function of the corrected face-value '$\zeta_f^{*^*}$', upwind volume fraction 'α_U' and downwind volume fraction 'α_D':

$$\alpha_f^{HRIC} = \zeta_f^{*^*}(\alpha_D - \alpha U) + \alpha_U \tag{2.18}$$

The HRIC scheme hence allows for a smooth capturing of the interface using a coupling of upwind and downwind methods that allow for higher resolutions and lower computational times as the calculations are performed altogether in the same time step.

2.2.2 Contact Angle Modeling

The contact angle θ as seen in figure 2.2 proves to be an important factor in the determination of the surface tension force between the liquid and the solid substrate. This surface tension force σ is crucial in determining the spreading characteristics and contact angle propagation of the droplet. Generally, the stagnant contact angle is found and linked with the surface tension forces between the phases using 2.19, known as Young's equation. As seen in 2.2a

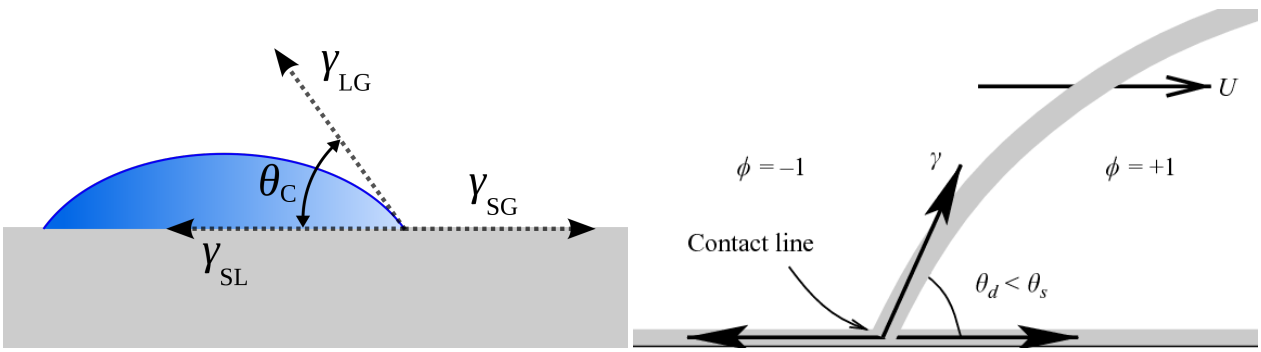

(a) Stagnant droplet on the surface to determine equilibrium contact angle

(b) Contacting droplet characteristics and schematic

Figure 2.2: Visualization of the contact line and contact angle θ used in determining the surface tension and wettability characteristics

Young's equation can be formulated as a function of the contact angle with respect to the surface tension between the liquid-gas, solid-gas, and solid-liquid phases, which is expressed as:

$$\gamma_{sv} = \gamma sl + \gamma_{lv} \cdot cos\theta \tag{2.19}$$

When the droplet is spreading the contact angle varies with respect to time due to the significance of the velocity in inertia and capillary-dominated flows. This time-varied contact angle is known as the dynamic contact angle which can be resolved using Kistler correlation method, implemented on StarCCM+.

The motion of the fluid along the surface is defined using the three contact lines as shown

in figure 2.2b, which is expressed as:

$$V = -(V \cdot \hat{n}_t) \tag{2.20a}$$

The velocity function in equation 2.20a is used to calculate the capillary number that will be utilized in Kistler's correlation function. The capillary number is given by equation 1.5 re-iterated below:

$$Ca = \frac{V\mu}{\sigma}$$

The Contact angle using the Kistler correlation is defined as θ_k on StarCCM+:

$$\theta_k = f_{Hoff}\left(Ca + f_{Hoff}^{-1}(\theta_s)\right) \tag{2.20b}$$

where, the Hoffman function f_{Hoff} is expressed as:

$$f_{Hoff}(x) = cos^{-1}\left(1 - 2tanh\left(5.16\left(\frac{x}{1 + 1.31x^{0.99}}\right)^{0.706}\right)\right) \tag{2.20c}$$

For the inverse of the Hoffman function, StarCCM+ uses a modified definition to achieve the closed form where $x^{0.99}$ becomes x. θ_s is the static contact angle input and Capillary number (Ca) is defined using 1.5 To improve accuracy in StarCCM+ a stability criterion is introduced, that provides for a range of input for the Ca number, resulting in a blend between the equilibrium contact angle and the dynamic contact angle as found by Kistler. The Ca range bounds are:

$$-Ca_{eq} < Ca < Ca_{eq} \tag{2.20d}$$

The dynamic contact angle can be defined as:

$$\theta_d = f\theta_e + (1 - f)\theta_k \tag{2.20e}$$

where θ_e is defined as the equilibrium contact angle which will be a user input, and f is the Capillary range factor which can be given as:

$$f = 0.5 + 0.5cos\left(\frac{Ca}{Ca_{eq}}\right) \cdot \pi \tag{2.20f}$$

2.3 Experimental Setup and Computational Domain

2.3.1 Experimental Setup

The computational domain has been modeled to closely resemble the standard experimental set-up for droplet impact on solid substrates. Figure 2.2, shows the experimental domain and the different instruments that are designed to facilitate the droplet impact experimental setup.

The setup consists of a micro-pump that will apply pressure to the syringe containing the liquid in order to dispense the liquid in the form of droplets of varying diameters, with the help of different configurations of needles. The impact plate is the location where the droplet impacts and its behavior is observed, which would be different based on the drop height, droplet diameter, and wettability (material) of the substrate for a type of liquid. A high-speed camera is used to record the morphology of the droplet.

Table 2.1: Boundary Conditions for the Computational Domain

Region	**Boundary Condition**
Impact Wall	Contact Angle
Plane of Symmetry	Symmetry
Outlet	Pressure Outlet

2.3.2 Computational Domain

The experimental setup provides the basis for the design of the computational domain, as seen in figure 2.3. The computational domain consists of a drop impact plate (drop area), located on the drop impact wall which acts as a solid substrate that helps observe the behavior of the droplet on impact. The physical boundary condition governing the impact wall is the contact angle that is specified.

The outlet boundary condition is satisfied with the use of a pressure outlet and there is a plane of symmetry as seen in table 2.1

Furthermore, the setup of the model involves the definition of its physical parameters, constants, and other reference parameters that will be obtained from the literature (Sikalo, Roisman), which will further be discussed in section 2.4

2.4 Model Setup: Its physical parameters and constants

Having spoken about the equations that are being solved, the experimental setup, and the computational domain, inputs need to be provided to the numerical simulation in the form of physical parameters and constants that are obtained from previous experimentation.

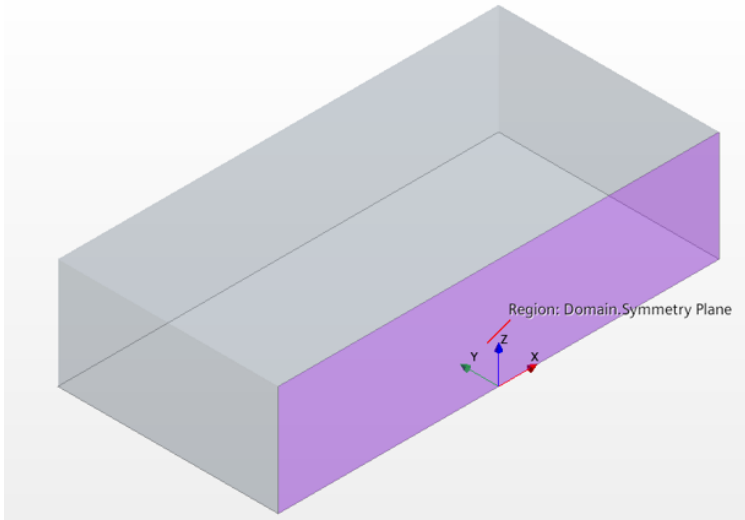

Figure 2.3: Geometry of the domain

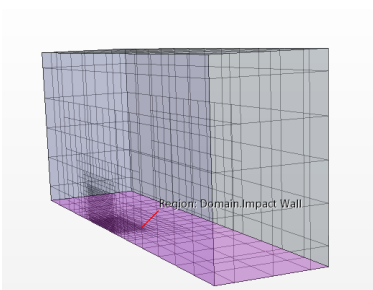

(a) The Impact Wall

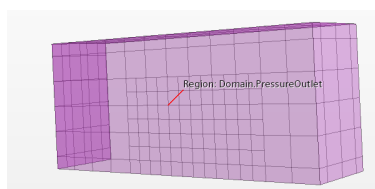

(b) Outlet Pressure Zones

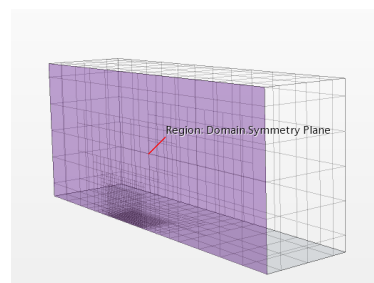

(c) Symmetry Plane

Figure 2.4: Different geometrical regions of the computational domain

These parameters are pivotal in understanding and controlling the type of droplet impact behavior being observed.

Foremost, the properties of the two interfaces, air, and water are defined as seen in table 2.2, these parameters are unique to the phase and do not vary at the interface. Certain parameters play a major role in affecting results during phase interaction, these are the multiphase interaction parameters such as the surface tension (ability of the liquid to minimize its surface area) and Interface Artificial Viscosity, which again depends on the type of fluid.

Apart from these physical parameters, in numerical simulations, certain mathematical rela-

Table 2.2: Material Properties

Parameter	**Value**
Water Density	$1000\ kg/m^3$
Water Dynamic Viscosity	$9.6305 * 10^{-4} Pa - s$
Air Density	$1.2\ kg/m^3$
Air Dynamic Viscosity	$1.85508 * 10^{-5} Pa - s$
Surface Tension	$0.0729\ N/m$
Interface Artificial Viscosity	0.2

tions coupled with physical interpretation play a major role in determining the outcome of a simulation. In Star CCM+ (solver), there is the implementation of the High-Resolution Interface Capturing Scheme (HRIC) with the use of the VOF function, which consists of parameters such as the sharpening factor, angle factor, upper and lower limits for the CFL condition as seen in table 2.3. CFL is a function of the time step and grid size acts as a defining parameter in carrying out an accurate CFD simulation.

Table 2.3: HRIC Scheme Parameters

Parameter	**Value**
Sharpening Factor	0
Angle Factor	0.05
Lower CFL Limit	0.1
Upper CFL Limit	0.5

The basic setup for the simulation involves a CFL range of 0.1 to 0.9, of which CFL values over 0.5 were not considered due to their inaccuracy in recreating the impact characteristics of the droplets, details of which will be discussed in chapter 3.

2.5 Chapter Summary

A general idea of the governing equations used in solving the problem and their origins were explained to provide a background for the VOF and MCL models in use. With an emphasis on the use of interface tracking and contact angling. An overview of the experimental set-up designed in the multiphase flow lab (figure 2.1 provides the basis for the development of the computational domain which is shown in figure 2.3, along with the boundary conditions. A basic set-up of the model, with the material properties and numerical parameters, is discussed to determine the inputs for the model. A brief overview of the baseline experiments by Sikalo et al. provides the experimental input parameters that allow the modeling of the impact parameters and recreation of the droplet dynamics. Quantitative and Qualitative analysis is performed with a comparison of the droplet height ratio (h/D) and droplet diameter ratio (d/D) with the baseline experiment. Observations are conclusive in showing the percentage variation between the droplet diameter evolution quantified from the simulations and the baseline experiment to be 9.05% whilst, the numerical droplet height characteristics vary by about 3.05% when compared to the baseline experiment.

Conclusions can be made about the accuracy of the model to be well in agreement with the experimentation and being suited for further parametric variation to further test its accuracy and robustness with varying numerical parameters and considering different experimental cases as will be seen in Chapters 3 and 4.

Chapter 3

Verification and Preliminary Validation of Model

3.1 Introduction

This chapter discusses details about the methods followed in determining the variation of numerical parameters to test the robustness of the model. Qualitative and quantitative analysis is performed to compare the effect of variation of CFL and Grid Refinement, in the prediction of the droplet impact characteristics. Conclusions will be drawn from the variation of these key parameters (CFL and Grid Refinement) in their effect on the numerical simulation, which will be compared again to the baseline experimentation to try to determine the best CFL condition and grid refinement to proceed with in order to reduce the number of cases that would be required in comparing the experiments performed in the multiphase flow lab with the computational model.

3.2 Model Comparison to Baseline Experiment

3.2.1 Introduction to Sikalo et al. Experiments

The study in focus here is the 'Dynamic contact angle of spreading droplets (2005) by Šikalo et al. [67]. Certain conclusions made in this study are relevant to current research focused on modeling the impact dynamics of droplets. The authors pointed out the use of a total energy balance being the most used theoretical model but also point out that the VOF model has shown great promise in simulating droplet impacts. Efforts have seen most research predicting the inertial dominated motion well but lacking in the prediction of the receding phase, which is of primary focus in this study.

The authors concluded that the effect of the static contact angle on the simulation has no effect in comparison to the coupled dynamic contact angle for larger ranges of experimental data, which makes the contact angle one of the boundary conditions for the simulation.

3.2.2 Baseline Experiments

Sikalo et al. performed a set of experiments in which one case has been shown to agree well with their computational model, which is data from their 7th experiment. The impact of water droplets on a solid substrate of wax, the configuration of the experiment as seen in table 3.1:

Experimental data from Sikalo's Experiment 7 is used as the baseline to compare with the model. Model parameters are defined as seen in table 3.2, where the input data for velocity, droplet diameter, advancing, and receding contact angles are experimental values from the baseline.

Table 3.1: Experimental parameters for droplet sized 2.45mm

Experiment	**Liquid**	**Substrate**	**Impact velocity (m/s)**	**We**	**Re**
Exp. 7	Water	Wax	1.64	90	4010

3.2.3 Numerical Simulation

Default numerical parameters are set for validating the model with the baseline. A grid refinement of level 3, generates a cell count of the order 10^4 and an average time-step CFL condition set to 0.5 with a minimum cell size set to 10^{-6}.

Table 3.2: Simulation input parameters

Parameter	Droplet Diameter (D_o) (mm)	Impact Velocity (m/s)	Adv. CA(θ_a)	Rec. CA(θ_r)
Value	2.45	1.64	105°	95°

As seen in table 2.5, input for Advancing Contact Angle (ACA) and Receding Contact Angle (RCA) of 105° and 95° are provided, which will act as the input for the Blended Kistler CA hysteresis model as observed in equation 2.20e, reiterated below.

$$\theta_d = f\theta_e + (1 - f)\theta_k$$

The convergence criterion for the simulation after multiple iterative tries has been configured as seen in table 3.3:

Table 3.3: Stopping criterion used in simulation setup

Quantity	Continuity	X-Momentum	Y-Momentum	Z-Momentum	Water	Maximum Inner Iterations
Limit	$1e-4$	$1e-4$	$1e-4$	$1e-4$	$1e-4$	50

Qualitative Comparison

As observed from the quantitative data, the numerical simulation works to a good extent in capturing the diameter and height evolution of the droplets. Along with the quantifiable

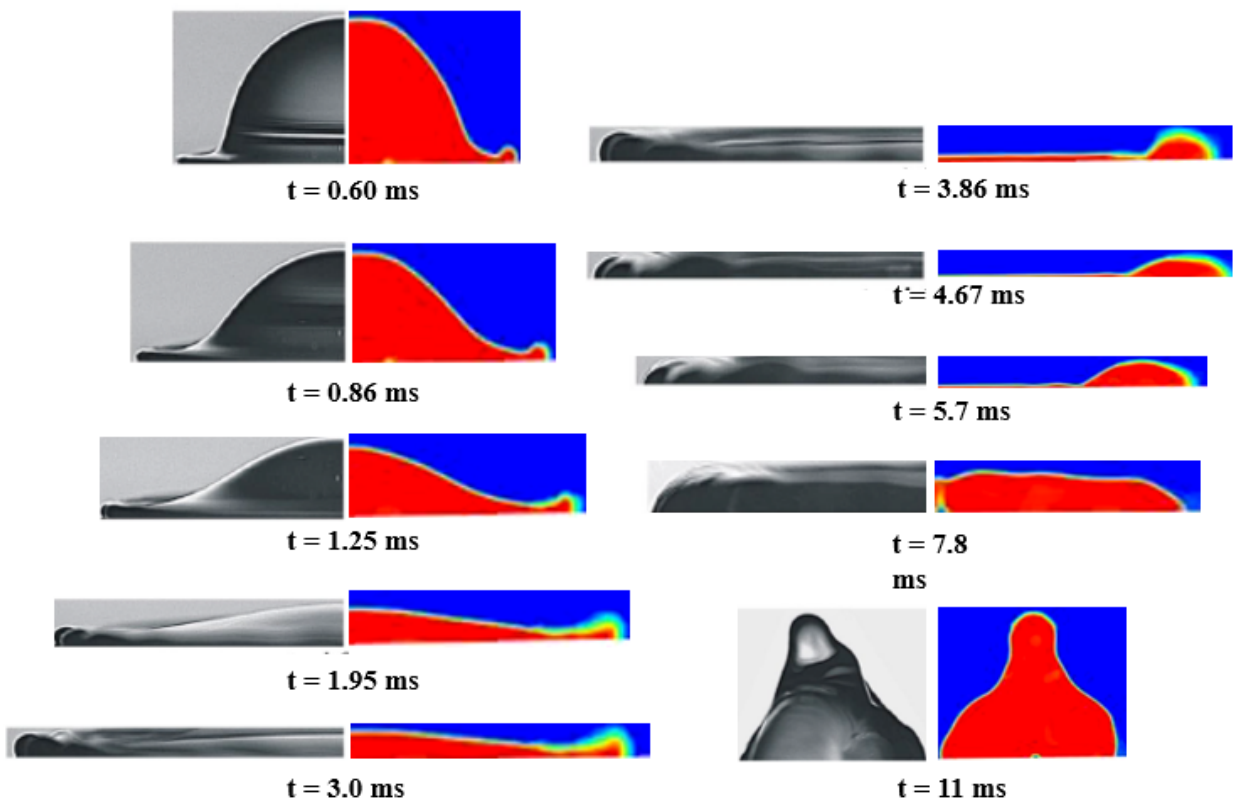

Figure 3.1: Droplet impact evolution comparison between experiments (left) and simulation (right)

data, using the scene animation feature, images are extracted from StarCCM+, as seen in

figure 3.1. On the left side of each sub-image, in the grayscale is the experimental droplet imaging as published in Sikalo et al., and on the right side of each sub-image is the front-view image of the droplet obtained from the numerical simulation.

Initial observations show a similar trend of evolution between the time-varied images between the experiments and the simulation. On further examination of the time-varied images in figure 3.1, it is clear that at time 't = 0.60 ms' the droplet diameter is marginally lesser and height slightly bigger on the numerically simulated droplet image whereas, with the progression of time, we see a trend where the droplet diameter is slightly over-predicted and the droplet height is under-predicted in comparison to the experiments. This trend is in agreement with the quantitative analysis as seen in the graphs in figures 3.2 and 3.3.

Quantitative Comparison

Post-processing of the results from the simulation shows promising results as observed in figure 3.3, where the non-dimensional time (tau) is plotted against the droplet diameter ratio for the experimental data obtained from Sikalo et al., calculations from Sikalo et al. and Numerical results from the model. The graph in figure 3.2 characterizes the spreading and receding dynamics of the droplet, which can be used to quantitatively compare the experiments with the numerical simulation.

Observations from the graph in figure 3.2 show the diameter ratio to be 1 in the beginning as expected at $\tau = 0$. All the curves have a similar trend, with the Numerical (blue curve) and the Calculation: Sikalo(2005) (dotted yellow curve) showing a good agreement with the experiments. The error between the Numerical and the Experimental data is found to be 9.05% which is estimated by calculating the absolute difference between the points on the plot and averaging them to get the absolute percentage error, meaning the numerical

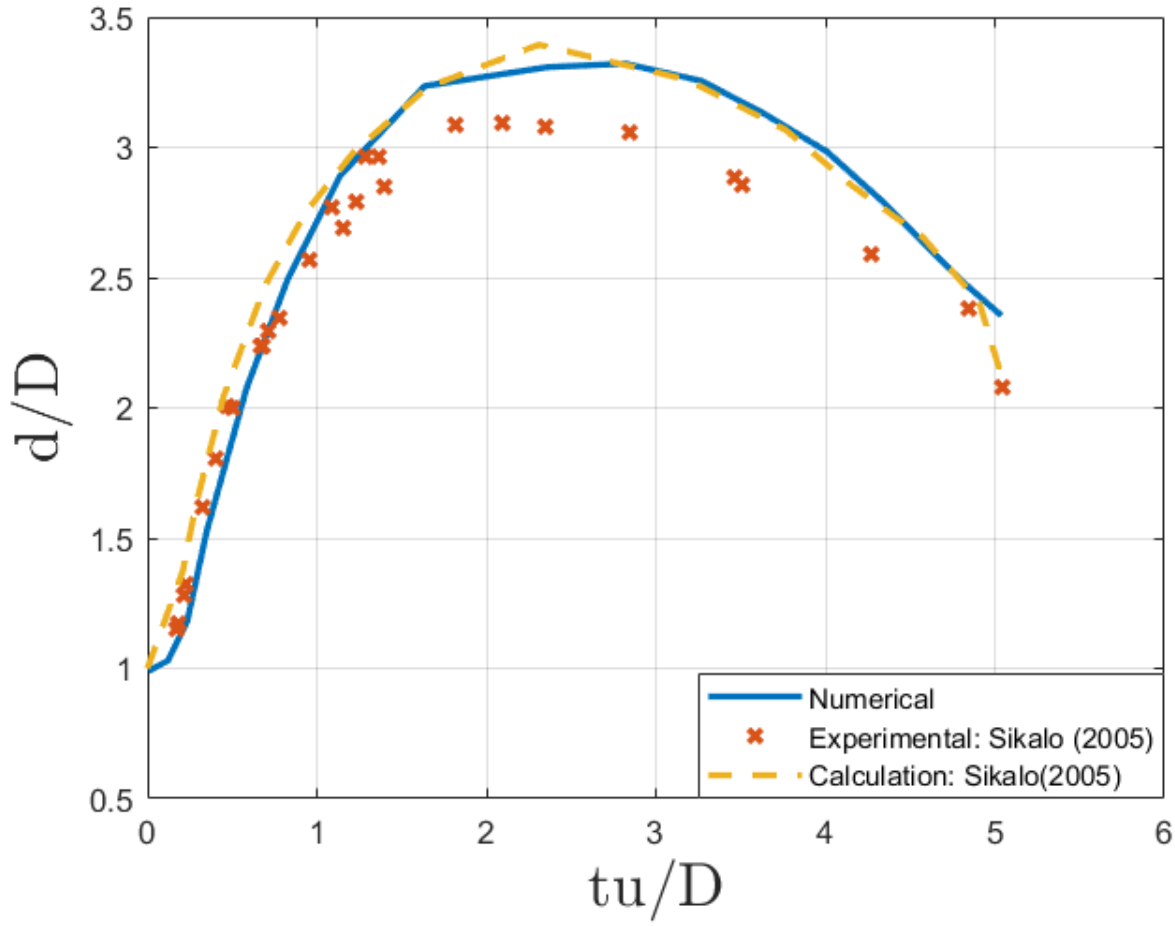

Figure 3.2: Comparison of time-varying experimental diameter ratio with numerical simulation and Sikalo's calculations

simulation has been able to capture the droplet diameter evolution to a very good extent and predicts the spreading and receding characteristics almost as well as Sikalo's calculations.

The graph in figure 3.3 depicts the droplet height evolution over time, with the non-dimensional time plotted with respect to the non-dimensional droplet height variation. This can also be used to quantitatively compare the numerical simulation with the experimental data.

Observation from the graph in figure 3.3 shows a similar trend between the experiments

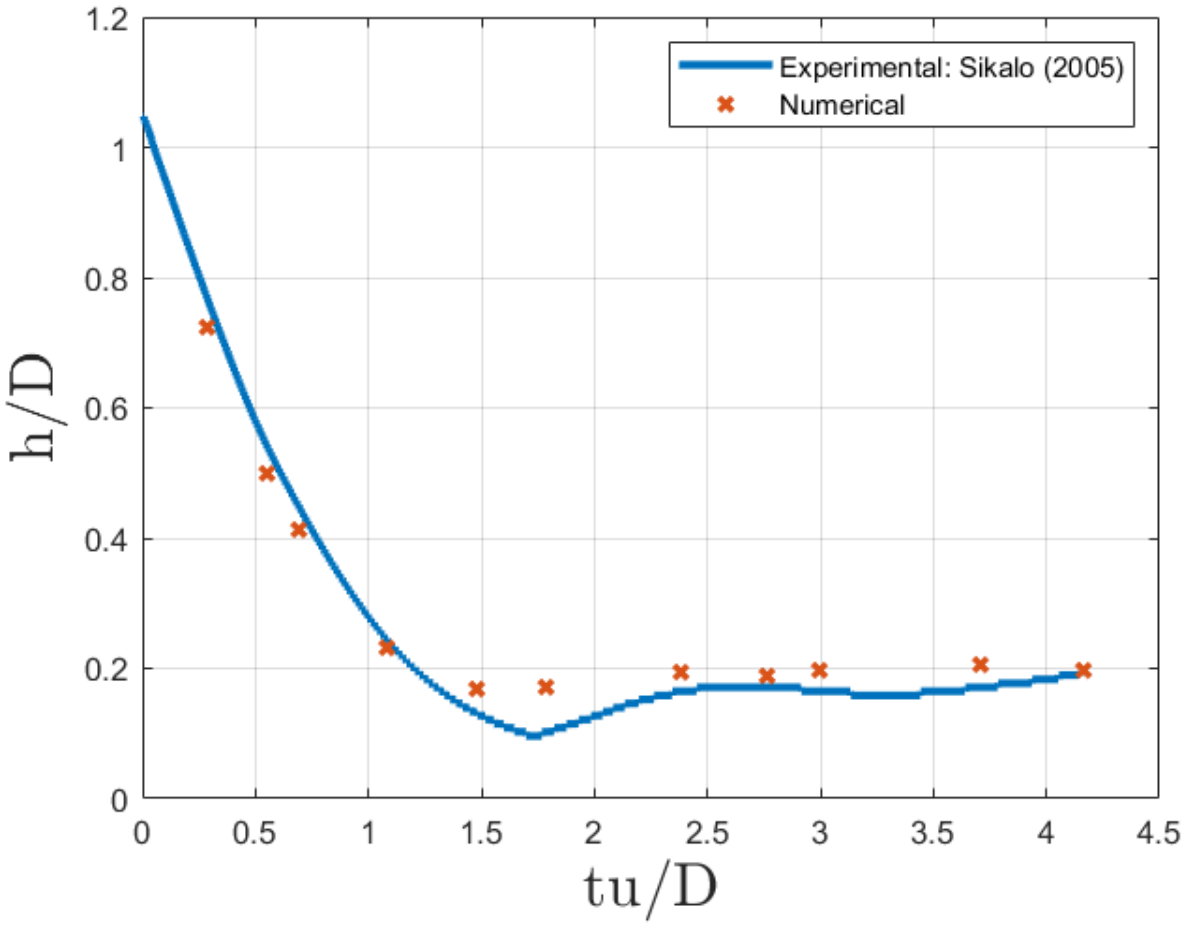

Figure 3.3: Comparison of time-varying experimental height ratio with numerical simulation

(x) and the numerical simulation (blue curve), with the numerical simulation showing a good agreement with the experimental data. A similar method to the one used in the droplet diameter comparison is used to calculate the absolute percentage error between the experimental data and the numerical simulation for the droplet height evolution. The error between the Numerical and Experimental data is found to be 3.05%, showing the capability of the solver to capture the droplet height evolution and its characteristics to good measure.

3.3 Methodology for parametric variation

Chapter 2 showed the development of the model and its default settings implemented in comparison to Sikalo's experimental data. The computational model shows good agreement with the baseline experiments and can further be studied and altered to make it more robust for general application. Variations of the CFL condition and the Grid refinement is expected to impact the results from the simulation and vary the impact behavior that is observed.

3.3.1 Variation of CFL condition

As seen in table 3.4, the numerical simulation setup is tabulated to reflect the variation in the CFL condition. The CFL is varied from 0.1 to 0.8. The CFL numbers being considered are 0.1,0.2,0.4,0.6 and 0.8. As formulated in equations 3.1, re-iterated below, the change in CFL condition and adaptive grid refinement technique, there will be a variation in the time-step throughout the simulation, which will be governed by the HRIC scheme.

$$CFL = u\frac{\Delta t}{\Delta x} \tag{3.1a}$$

Where Co is the courant number and ϕ is the adaptive time-step criterion. In StarCCM+ the Time Step Condition for the VOF function depends on the volume fraction of each cell due to which the adaptive time stepping and the grid sizes can be expressed as equations 3.1b and 3.1c respectively:

$$\phi = CFL \cdot \overline{\phi}_t \tag{3.1b}$$

Where, $\overline{\phi_t}$ is the local rate of change of volume fraction. The final equation for the adaptive

Table 3.4: Modeling parameters for numerical simulation setup for vary CFL Conditions

Category	Parameters	Case1	Case2	Case3	Case4	Case5
Domain	Domain Size (mm^3)	29x7x12	29x7x12	29x7x12	29x7x12	29x7x12
Adaptive Time Step Size	Min. time-step size	$1e-6$	$1e-6$	$1e-6$	$1e-6$	$1e-6$
	Max. time-step size	$5e-6$	$5e-6$	$5e-6$	$5e-6$	$5e-6$
Adaptive Mesh Refinement	Transition width	5	5	5	5	5
	Refinement level	3	3	3	3	3
	Min. adapted cell size	$1e-6$	$1e-6$	$1e-6$	$1e-6$	$1e-6$
HRIC Scheme	Sharpening factor	0	0	0	0	0
	CFL Lower Limit	0.1	0.1	0.1	0.1	0.1
	CFL Upper Limit	0.5	0.5	0.5	0.5	0.5
CFL	Target CFL condition number	0.1	0.2	0.3	0.4	0.5

grid sizing for unit magnitude velocity can be expressed as:

$$\Delta x_{adaptive} = \frac{\Delta t \cdot \overline{\phi}_t}{\phi} \tag{3.1c}$$

The solver is implicit and hence, these conditions are updated every time step, meaning at every time step the grid adapts and the time-step varies. While the CFL condition is varied, other parameters are kept constant so as to not be influential in the result, as changing any parameter will have an adverse effect on the outcome of the simulation. A grid refinement

level of 3 is fixed for all cases with this configuration of CFL variation, hence using the simulation data, quantitative comparisons can be made between the baseline experiment and the numerical model.

This configuration involves keeping constant values for the maximum and minimum time step values and the minimum adapted cell size for all CFL values causing any numerical parametric change to be attributed to the variation of the CFL condition. This variation of CFL can be compared to identify the ideal CFL condition to move forward with for testing the effect of variation of the Grid Refinement Level.

3.3.2 Variation of Grid Refinement Level

As seen in table 3.5, the numerical simulation setup tabulated explains the numerical parameters used in setting up cases for varied Grid Levels. Grid refinement levels of 3,4 and 5 are evaluated with maximum cell counts of x,y and z respectively. The change in the grid refinement levels vary the time-step condition similar to the CFL but is directly proportional to it as seen in equation 3.1c.

While the CFL condition is varied, other parameters are kept constant so as to not be influential in the result , as changing any parameter will have an adverse effect on the outcome of the simulation. A CFL condition number of 0.1, has been fixed for these simulations as a result of the calculations performed to determine the effect of the CFL condition, which can be seen in the graph in figure 3.7, using the data from these simulations with varied grid refinement levels, qualitative and quantitative analysis can be performed, with comparisons that can be made to the baseline experiment to determine the robustness of the model with different configurations.

This configuration involves keeping constant values for the maximum and minimum time

Table 3.5: Modeling parameters for numerical simulation setup for vary CFL Conditions

Category	Parameters	Case1	Case2	Case3	Case4
Domain	Domain Size (mm^3)	29x7x12	29x7x12	29x7x12	29x7x12
Adaptive Time Step Size	Min. time-step size	$1e-6$	$1e-6$	$1e-6$	$1e-6$
	Max. time-step size	$5e-6$	$5e-6$	$5e-6$	$5e-6$
Adaptive Mesh Refinement	Transition width	5	5	5	5
	Refinement level	2	3	4	5
	Min. adapted cell size	$1e-6$	$1e-6$	$1e-6$	$1e-6$
HRIC Scheme	Sharpening factor	0	0	0	0
	CFL Lower Limit	0.1	0.1	0.1	0.1
	CFL Upper Limit	0.5	0.5	0.5	0.5
CFL	Target CFL condition number	0.1	0.1	0.1	0.1

step values and the minimum adapted cell size for all CFL values causing any numerical parametric change to be attributed to the variation of the grid refinement. This variation of refinement level can be used to compare the difference in results and understand the computational cost and effectiveness of the model.

3.4 Effect of varying CFL Condition

3.4.1 Qualitative Comparison

Qualitative comparisons can be made based on the time evolution of the droplet morphology that will be compared to the experimental data quantitatively, to determine the accuracy of the trends observed.

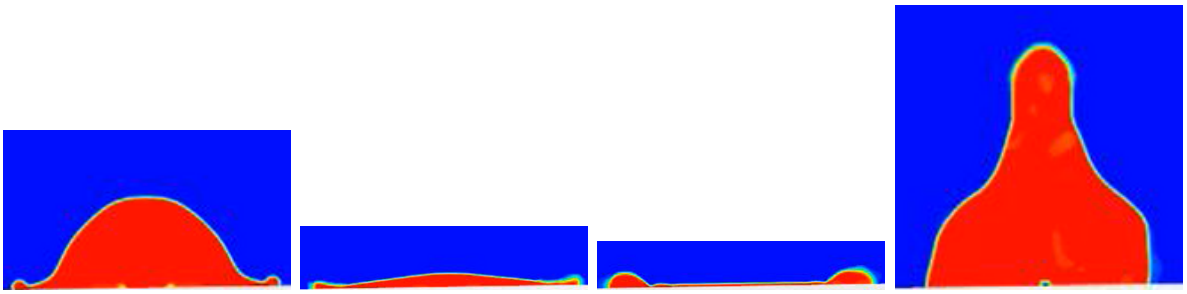

(a) 0.6 ms (b) 2.0 ms (c) 5.0 ms (d) 11.0 ms

Figure 3.4: Visualization of the droplet evolution on impact for CFL Condition number 0.1

Observations from these images in figure 3.4 suggest a good agreement of the case with the experimental data that can be seen in figure 3.3, with figure 3.4a capturing the impact stage, figure 3.4b showing the spreading stage, figure 3.4c showing the beginning of the receding phase and figure 3.4d showing the final stage of the droplet where due to the inertia, it reaches a momentum where it tries to partially rebound but is not able to due to the surface tension force which overcomes the inertia and binds the droplet to the solid substrate.

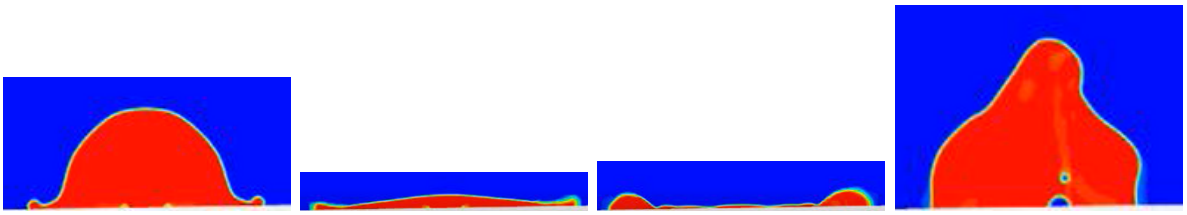

(a) 0.6 ms (b) 2.0 ms (c) 5.0 ms (d) 11.0 ms

Figure 3.5: Visualization of the droplet evolution on impact for CFL Condition number 0.4

Looking closely at the images in figure 3.5 for CFL 0.4, during the impact and spreading phase, the behavior of the droplet resembles that of the experiments and the numerical results from CFL 0.1. When the droplet starts to recede as seen in figure 3.5c, there is a slight breakup in the droplet lamella, where the fluid is pushed towards the rims (edge) of the droplet, which reduces the overall momentum. As a result of this fluid moving to the rims, in figure 3.5d, the droplet fails to have enough momentum to resemble the scenario of a partial jet, which is observed in the experiments and the numerical simulation with CFL 0.1.

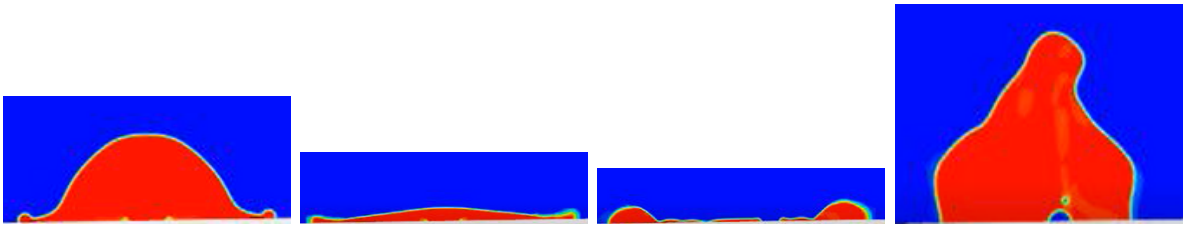

(a) 0.6 ms (b) 2.0 ms (c) 5.0 ms (d) 11.0 ms

Figure 3.6: Visualization of the droplet evolution on impact for CFL Condition number 0.8

A similar behavior to what was observed in the case of CFL 0.4 in figures 3.5, is observed in the case of CFL 0.8 as seen in figures 3.6. In the case of CFL 0.8, there is more breakup earlier and the momentum transfer is quicker, thereby still having enough energy to be able to create a jet (seen in figure 3.6d) with a height greater than that observed in figure 3.5d, but still not as accurate as in the case of CFL 0.1, in figure 3.4d.

3.4.2 Quantitative Comparison

Focusing on the variation of the CFL condition between values of 0.1 to 0.8, comparing their results both qualitatively and quantitatively provides a great estimate in determining the robustness of the model. As seen in figure 3.7, CFL condition numbers (CN) are compared with the experimental results from the baseline and the calculation from the baseline, aiding

in understanding the effect of the variation.

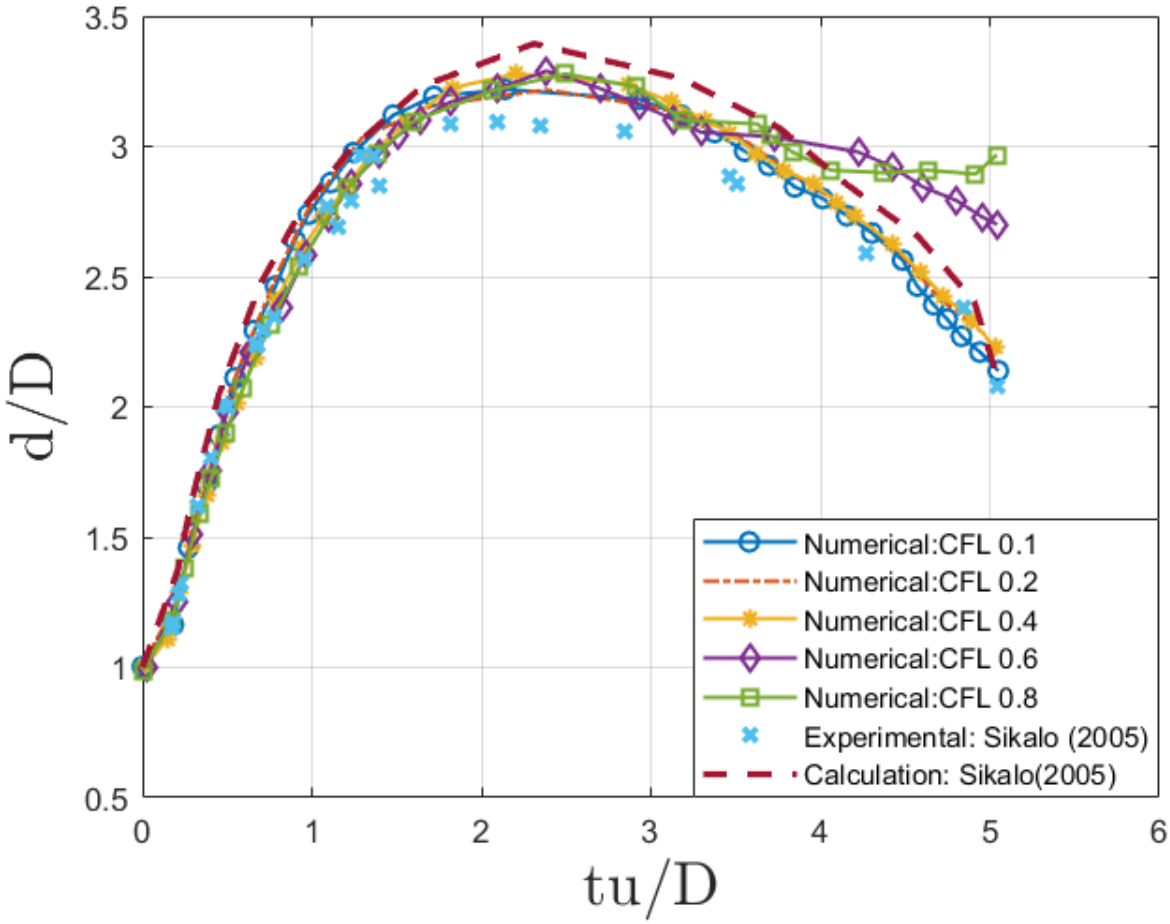

Figure 3.7: Droplet diameter ratio evolution over time compared to baseline experiment for different CFL Condition Numbers(CN)

Droplet Diamater Evolution

As seen above in figure 3.7 the variation in CN has an effect on the droplet diameter evolution. The minimal difference in diameter ratio at the beginning of the simulation portrays the ability of the model to capture the spreading characteristics in the advancing stage to a very good extent in most cases. The difference although arises when the droplet settles and

begins to recede, during this phase as mentioned in the literature (paper), previous models struggle to recreate the dynamics during the receding phase, but in this case, the case of the CN 0.1, agrees with the experimental results during both, advancing and receding stages with an overall absolute percentage error of about 8.14% as seen in table 3.2. An increasing trend in the absolute percentage error is observed between the CN-varied numerical diameter ratio with respect to the experimental diameter, where the error increases to 9.60%, 10.28%, 15.96% and 17.87% for CN 0.2, 0.4, 0.6 and 0.8 respectively.

In terms of computational cost and Wall-time, there is not a significant difference between the CFL values for 0.1 and 0.2 that provide for a more accurate representation and comparison for the droplet diameter ratio, when compared to the baseline experiment. This is suggestive of the fact that CFL condition number of 0.1 can be used for simulations moving forward in order to achieve better accuracy without a significant increase in computational cost.

Droplet Height Variation

As seen in figure 3.8, the variation in CN has minimal effect on the droplet height evolution. The difference in droplet height ratio at the beginning is almost negligible when comparing the different numerical CN variation curves with the baseline experimentation.

However, as observed in the case of the droplet diameter evolution, the droplet height variation also undergoes a noticeable difference for varied CN values during the receding phase, where CN 0.2, has the least absolute percentage error of 3.44% when compared to the baseline experiment, which is followed closely by CN 0.1 with an error of 3.88%, these differences in errors portrays an increasing trend with increase in CN with CN 0.8 having an error of 4.73%. Although the trend in error is increasing with an increase in CN, the percentage error across the varied CN values is under 5%, pointing to the fact that variation of CN did

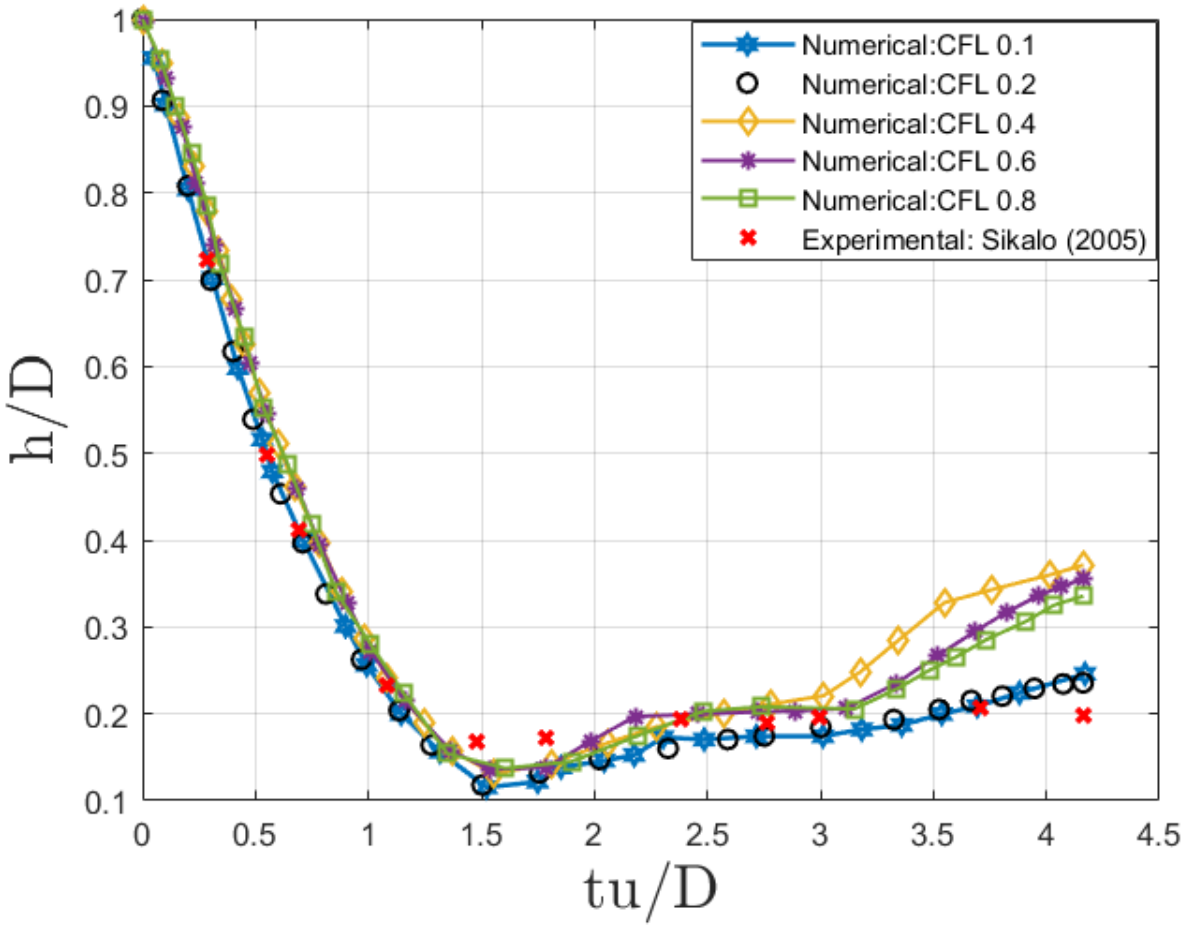

Figure 3.8: Droplet Height Ratio evolution over time compared to baseline experiment for different CFL Condition Numbers (CN)

not have much of an effect on the prediction of the droplet height variation in the numerical simulation.

In terms of the effectiveness of the droplet height variation as a parameter for validation of the model, there is not much variation when the CFL is varied with cases of no rebound. Hence, droplet height variation as a parameter would be useful only when modeling droplet impact behavior where we have a complete rebound.

Table 3.6: Absolute percentage error comparison of Numerical diameter and height data with experimental diameter and height for varying CFL Condition numbers

CFL Condition	**0.1**	**0.2**	**0.4**	**0.6**	**0.8**
Numerical Diameter Error (%)	8.14	9.60	10.28	15.96	17.87
Numerical height error(%)	3.88	3.44	4.66	4.44	4.73

3.5 Effect of varying Grid Refinement Level

3.5.1 Qualitative Comparison

Qualitative comparisons can be made on the droplet evolution based on the grid refinement levels that are simulated to identify the effect of variation of the refinement levels. With each grid level change, the initial number of cells created in the domain changes as the grid refinement level increases, the refinement level is then managed with the help of the adaptive grid refinement technique that has been explained in chapter 2 using equation 3.1c.

Observing the droplet meshing characteristics during the initial impact stages in figure 3.9, refinement level 2 can be seen to have the least number of cells formulated at the interface as seen in figure 3.9a. The number of cells at the interface shows an increasing trend as we increase the level of refinement with grid refinement level 4 showing the maximum level of refinement at the interface, as seen in figures 3.9b and 3.9c, which is expected and will be analyzed further from the quantitative comparison. Figure 3.10 shows a zoomed-in view of the interface region of refinement level 2 (3.10a) and refinement level 4 (3.10b), which

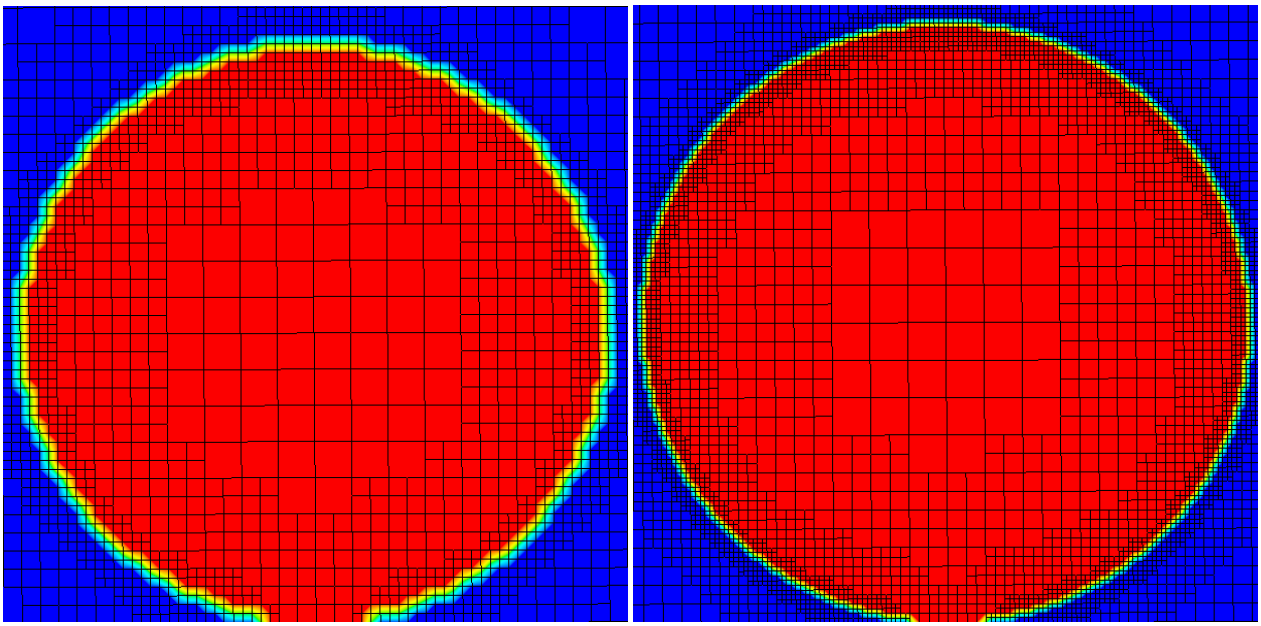

(a) Initial droplet meshing at Grid Refinement Level 2

(b) Initial droplet meshing at Grid Refinement Level 3

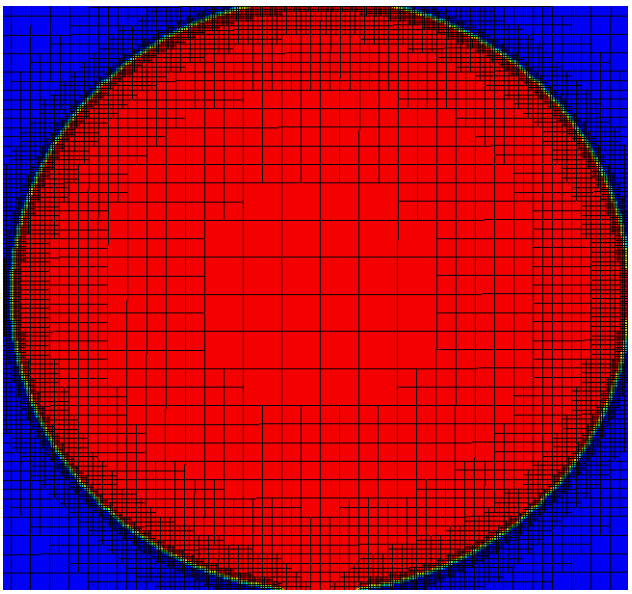

(c) Initial droplet meshing at Grid Refinement Level 4

Figure 3.9: Visualization of the droplet meshing at the different refinement levels at time 0ms

further demonstrates the difference in the refinement levels due to the prominence of the HRIC scheme for free-surface refinement at higher refinement levels. The cell counts can be

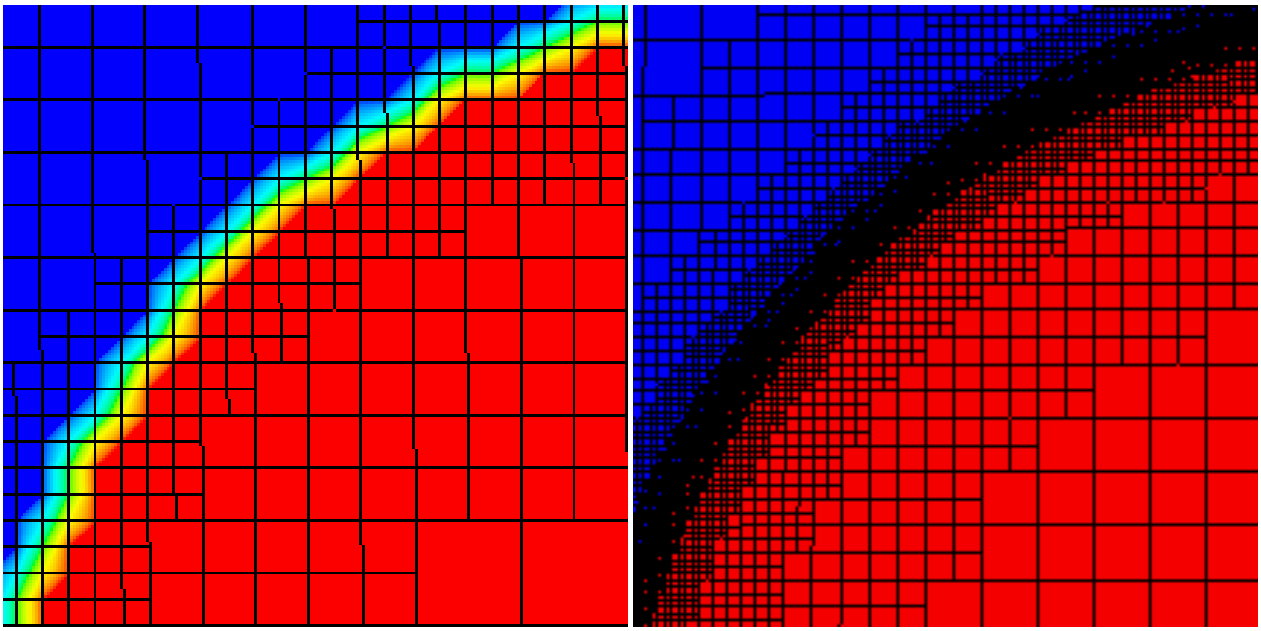

(a) Zoomed in view of initial droplet meshing at Grid Refinement Level 2

(b) Zoomed in view of initial droplet meshing at Grid Refinement Level 5

Figure 3.10: Zoomed in view of initial droplet meshing at the interface for refinement level 2 (left) and refinement level 5 (right)

observed during the beginning of the simulation from table 3.7, which further asserts the direct relation between the refinement level and the number of cells at the interface.

An important point to be noted is the fact that these cell counts and grid refinement variations are performed at a fixed CFL condition number of 0.1, as expressed through table 3.5.

3.5.2 Quantitative Comparison

A quantitative comparison of the variation of grid refinement is performed keeping in mind limitations such as the computational cost and the accuracy of the simulation, grid refinement levels of 2, 3, and 4 are chosen to simulate the behavior of the impact dynamics at a constant CFL condition number of 0.1. Qualitative observations show that the higher refinement levels

Table 3.7: Variation of the cell count at time t=0 ms, for different refinement levels

Refinement Level	2	3	4
Cell Count	66892	276786	1110282

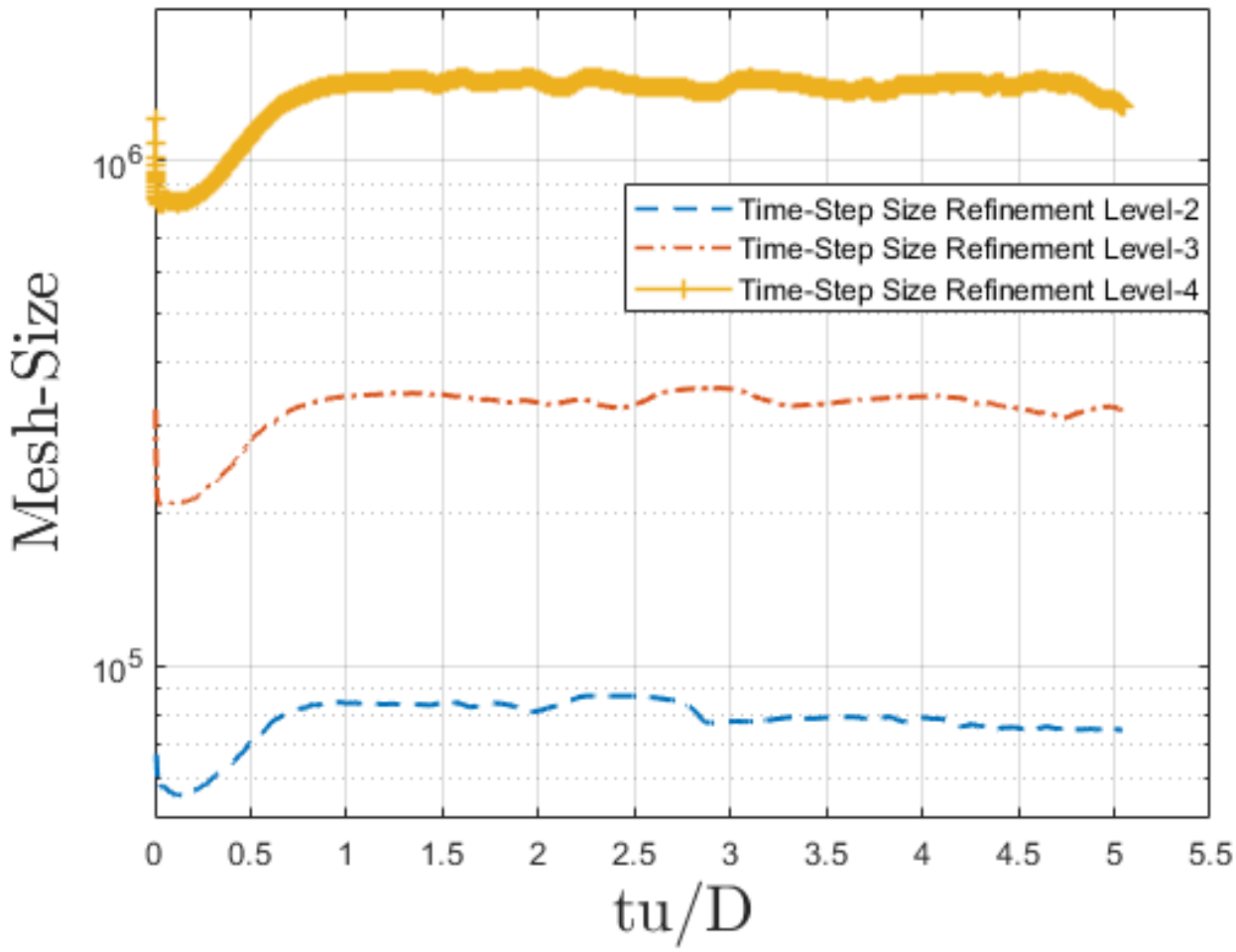

Figure 3.11: Mesh size evolution over non-dimensional time for different refinement levels

perform better in capturing the physical characteristics and behavior of the droplet compared to the lower refinement levels, although there is enough evidence to suggest that refinement

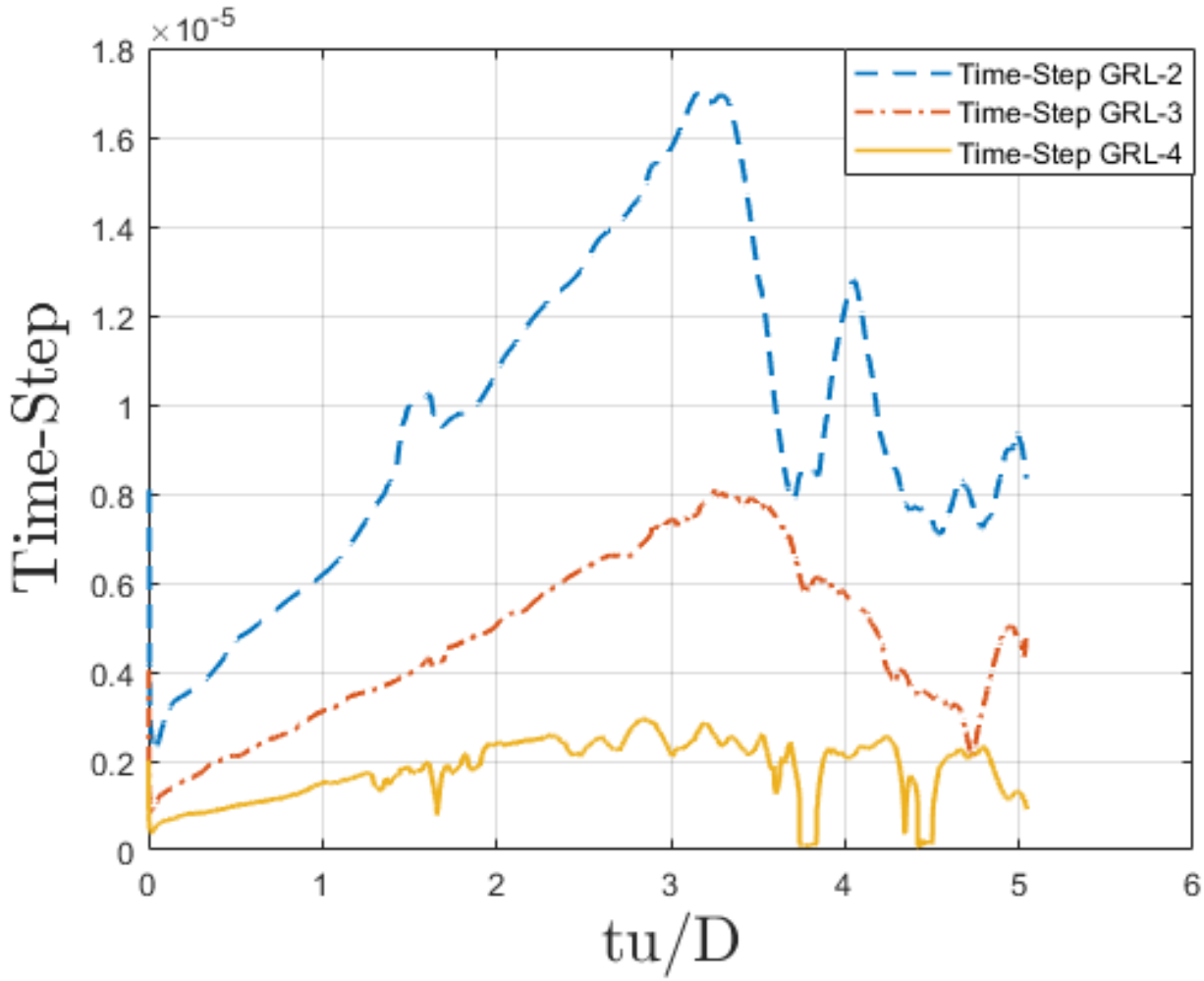

Figure 3.12: Time-Step size evolution over non-dimensional time for different refinement levels

level 3 is accurate enough in capturing the details for the droplet impact as seen in the cases of CFL variation. Plots shown in figures 3.11 and 3.12 are clear and obvious in pointing out this trend, where the time step size and the number of cells in the mesh vary proportionally for most parts, depending on the volume fraction averaged over all the cells, which is given by equation 3.1c, re-iterated below.

$$\Delta x_{adaptive} = \frac{\Delta t \cdot \overline{\phi}_t}{\phi}$$

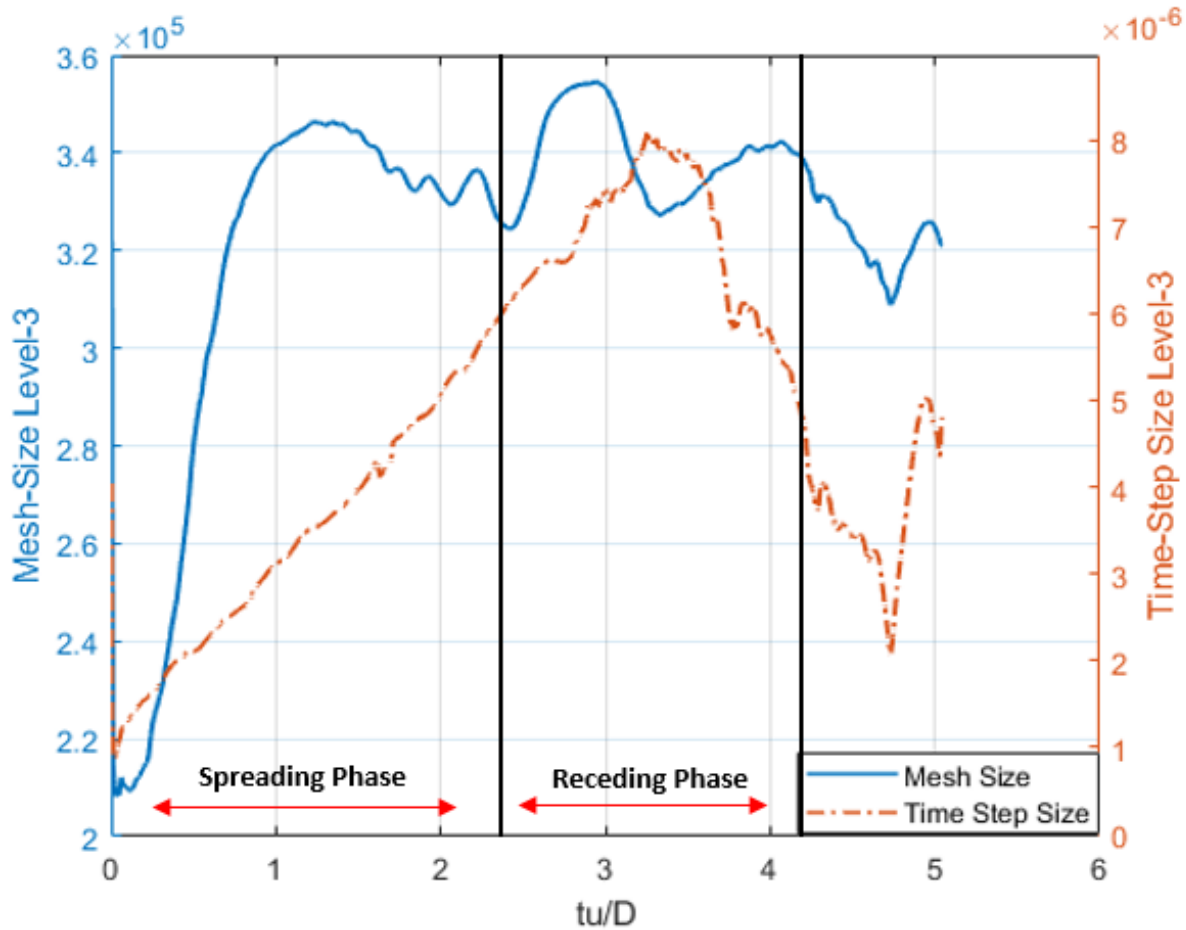

Figure 3.13: Mesh size and time-step size plot comparison showing the phases of the droplet impact varied over time τ

This trend is observed across all the refinement levels but fluctuations reduce as the refinement increases, showing that the solution gathers more stability with the increase in the number of cells.

At time $\tau \sim 2.2$, the droplet begins to recede, as seen in figure 3.13 where the spreading phase and the receding phase are shown based on the time evolution. At this time the mesh sizes can be seen stabilizing, numerically meaning that there is a sufficient number of

cells required to capture the physics of the droplet, as the mesh size more or less remains consistent throughout the simulation from here on. At $\tau \sim 3$, the droplet recedes and the momentum from the rims is transferred to the center of the droplet, it forms a jet, which is attached to the substrate. During this regime, the time-step casts a different trend where it begins to reduce meaning it takes more time for convergence. This could be attributed to the complexity of the flow at that point, with the VOF function and governing equations (continuity and 3D- momentum) requiring more iterations for convergence.

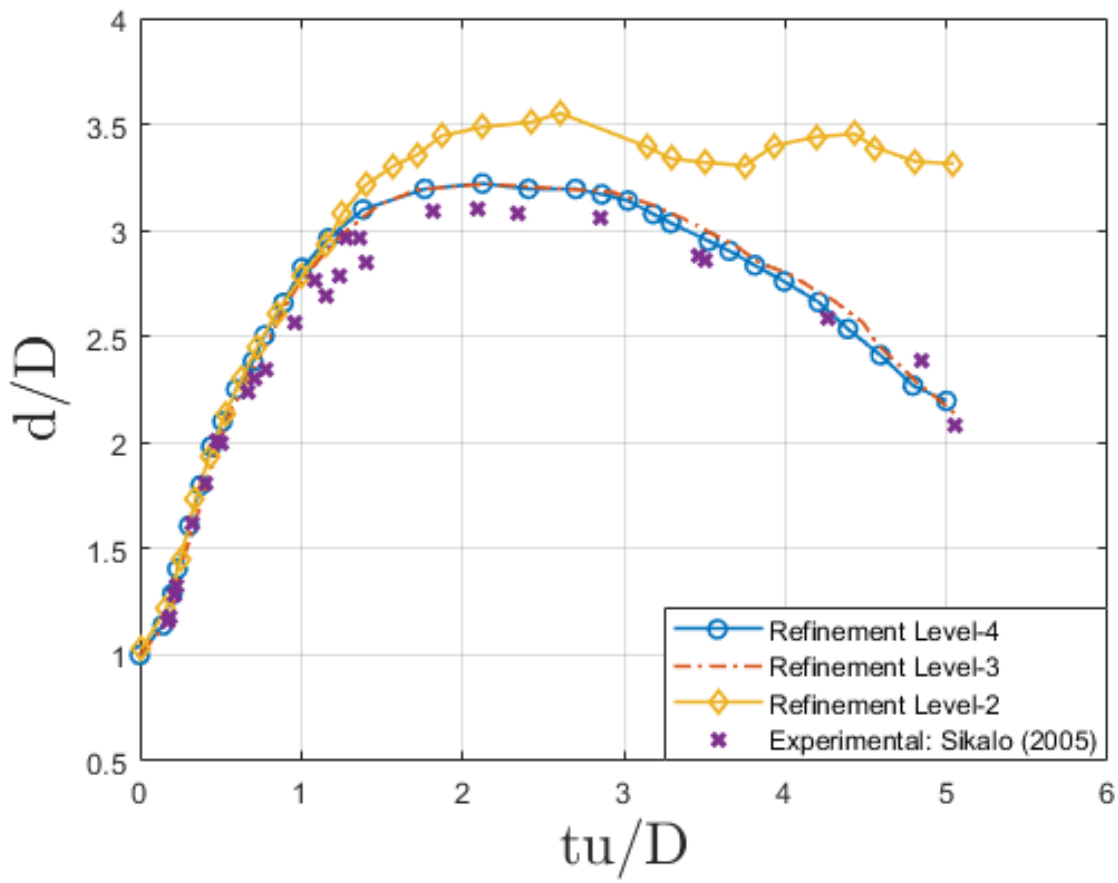

Figure 3.14: Evolution of the Droplet diameter ratio over non-dimensional time for different refinement levels compared with the baseline experiments

Looking at the droplet diameter comparison for the different refinement levels in 3.14, we see

Refinement Level	2	3	4
Numerical Diameter Error (%)	29.37	8.06	7.81

Table 3.8: Numerical error percentage for droplet diameter evolution from simulation compared to the baseline experiment

a decreasing trend in the absolute percentage error between the numerical simulation corresponding to each refinement level to that of the experimental data i.e., as the refinement level increases the error in the diameter evolution measured by the simulation decreases, which can be seen table 3.8 where the error in calculating the diameter is 29.37% for refinement level 2 and reduces down to 7.81% for refinement level 4, with a reduction in the error being drastic between level 2 and 3 but not showing much of a variation between level 3 and 4. This means that for the particular case in consideration, a refinement level of 3 does a good job of simulating the droplet impact behavior.

3.6 Chapter Summary

A comparison of CFL numbers and Grid refinement levels was performed for the baseline experiments with the numerical simulation developed in-house. Comparisons reveal the effect of CFL is major when it comes to determining the accuracy of the simulation but does not play a major role in the overall computational cost. Whereas the grid refinement level seems to capture well even at level 3 but has higher accuracy with higher grid refinement levels, as seen from table 3.8, the error in simulation is 29.27%, 8.06% and 7.81% for refinement levels 2,3 and 4 respectively. Although the accuracy is better, the increase in grid refinement levels leads to a significant increase in the computational cost. From the graphs depicting the time-step size along with the number of cells in the mesh in figures 3.11 and 3.12 respectively, it is

understood that the complexity of the flow and the volume fraction change across the domain alter the time-step sizes significantly and the mesh size to an extent. During the receding phase, where the flow is complex, the number of cells remains high for all refinement levels at $\tau = 3$ and the time-step size reduces, indicating more iterations per time-step and a longer duration for convergence of the solution. Hence, a refinement level of 3 and over can be ideal in the simulation of droplet impact on solid substrates, with a constant CFL condition number of 0.1, a refinement level can be decided based on computational cost, with a minor compromise in accuracy when choosing level 3 over level 5 to reduce the computational cost.

Chapter 4

In-house experimentation and data acquisition

4.1 Introduction

Having validated the model with the experiments from Sikalo (2005), this chapter will talk about the comparison of the experimental data obtained from the multiphase flow lab at Virginia Tech for three different cases with the numerical model. Details about the configurations for the experimental setup, data acquisition technique, and measurements are explained in brief to provide an idea of the uncertainty that might be associated with the data obtained from the experiments. Simulation data is qualitatively and quantitatively observed and compared with the experiments to draw conclusions from the comparative study. Parameters such as the Droplet spreading rate β, droplet diameter ratio (D/D_p), the splashing threshold, and dynamic contact angles are part of the comparative study in determining the robustness of the model and validity of the experiments.

4.2 Experiments

4.2.1 Experimental Set-up

Experiments performed with Joe in-house focused on finding the contact angles (ACA and RCA) along with the droplet diameter evolution over time for different surfaces. Set-up is

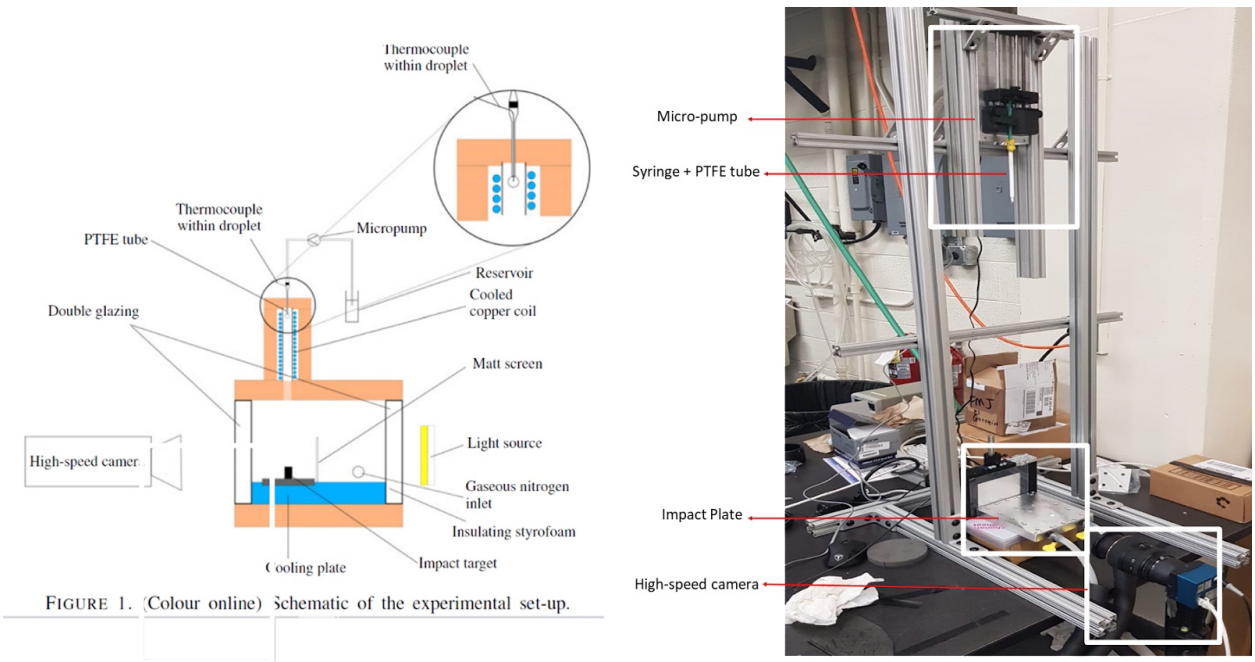

Figure 4.1: Experimental Setup from Multiphase Flow Lab (right) and experimental set-up schematic as seen in Roisman [43] (left)

similar to the one described in chapter 2 where there is a syringe along with a micro-pump that will release the fluid to form the droplet. An impact plate is located at the bottom where the droplet morphology is visualized by a high-speed camera capturing slow-motion videos. This basic setup helps analyze the droplet impact dynamics and calculate stagnant contact angles. The height from which the droplet is released can be altered which will result in a change in its impact velocity that is crucial in determining the droplet spreading and receding characteristics.

4.2.2 Configurations

Experiments were performed on three solid surfaces of different materials, where the behavior observed in each case was found to be unique. The materials used and their properties can be seen in the table below:

Table 4.1: Experimental cases with materials properties

Material	**Roughness (Ra)** (μ**m**)	**Impact Velocity** ($\mathbf{V_0}$) **(m/s)**	**Droplet Diameter** ($\mathbf{D_0}$) **(mm)**
Glass	0.4	1.1321	2.05
Aluminum	0.4	0.494	1.99
PETG	0.4	0.490	2.08

Three different materials show unique behavior even though their roughness is similar, this can be attributed to the fact that roughness is not the only factor contributing to the wettability and that, the contact angle of the surface depends on the surface tension as explained in equation 2.19, weighs in heavily when it comes to determining the behavior of the droplet on impact.

Hence, we must also look at the contact angle of the droplet on impact to understand the effect of the surface tension forces that are acting on the droplet. Initial droplet diameter will be a factor that will vary the velocity, which might also be a factor that will alter the behavior of the droplet on impact. Conclusions will be drawn from the results obtained from the data which will then be compared to the results obtained from the numerical simulation.

4.3 Data Acquisition

Explanation of the experimental setup enforces many variables that need to be taken into consideration while setting up data acquisition. Hence, it is important that measurement techniques be understood before data is acquired.

4.3.1 Methodology

Experimental data acquisition techniques are discussed briefly with information on the importance and use of each measurement. Contact angle measurement, droplet diameter, and velocities are measured by processing the images from the experiments.

Crucial to acquiring data is capturing images during the droplet evolution phase, this involves the use of a high-speed camera (Phototron Fastcam SA1.1) with a zoom lens (Navitar 6000). The general specifications for capturing images were as follows:

Frame Rate (fps)	**Resolution (px)**	**Shutter Speed (s)**
10000	726x726	1/17000

Table 4.2: Camera common configurations used in data acquisition

Droplet Diameter Measurement

The droplet diameter measurement is crucial in defining the location of the droplet and comparison with simulations. The diameter in case of impact is constantly varying, the time-evolution of the diameter is hence captured using the high-speed camera video, which is then post-processed using image processing techniques. As seen in figure 4.2, points are identified on the droplet, looking at the blue and red curves, which identify the contact lines

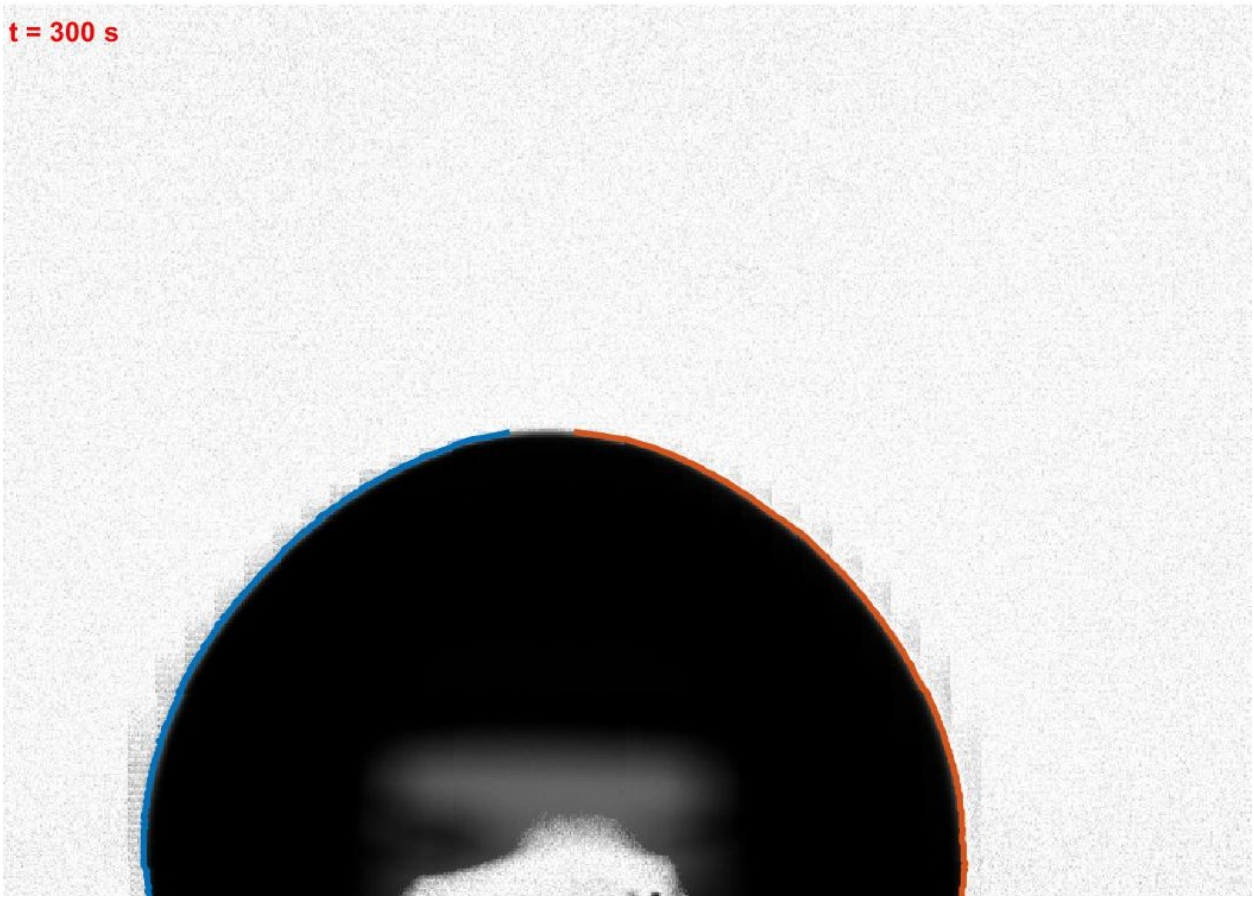

Figure 4.2: Droplet Diameter measurement tool using image processing

and the interface between the liquid and the vapor using a differentiation between dark and light pixels.

Contact Angle Measurements

The significance of measuring the contact angle comes from Young's equation (2.19) reiterated below:

$$\gamma_{sv} = \gamma sl + \gamma_{lv} \cdot cos\theta$$

The term governing the surface tension of the liquid (water) with respect to the vapor (air) involves the use of the angle θ, which is the contact angle, in calculating the surface tension

forces. While measuring contact angles, it is often not sufficient to measure the stagnant contact angle which does not account for the global energy confirming the stability of the droplet. Multiple factors come into the picture when measuring ACA and RCA, such as

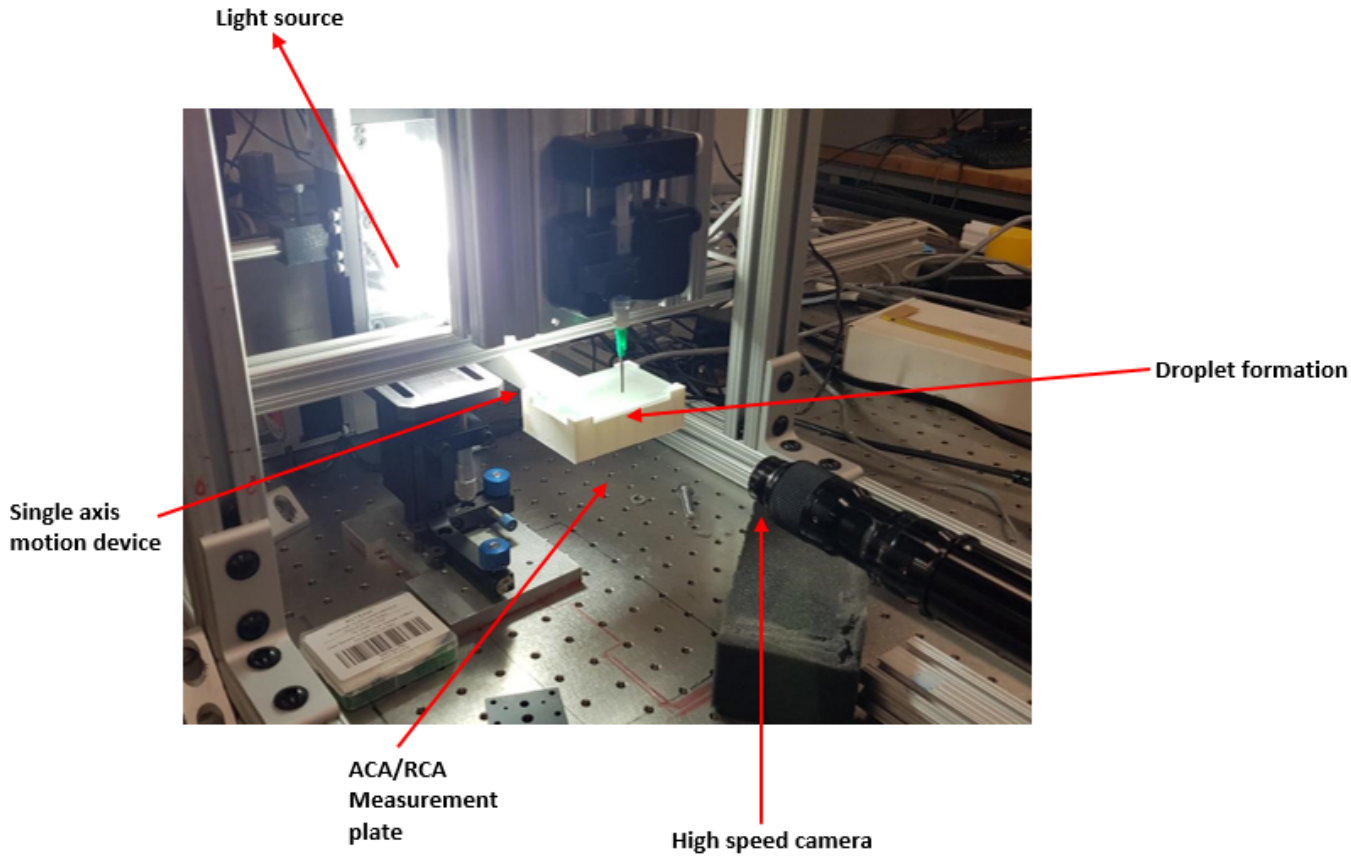

Figure 4.3: Experimental ACA/RCA and stagnant contact angle measurement setup

the uniformity of roughness, hydrophobicity of the surface, and any volatility present on the substrate. To measure stagnant contact angles, the droplet is deposited on the surface and kept stagnant, until a constant contact angle is reached (Huhtamäki et al. [20]), certain techniques involve retracting the droplet back with the needle to measure RCA, which did not accurately capture the contact line. ACA and RCA measurements involve a different technique, with a single-axis motion rotating column, that consists of a droplet deposition plate at one end. The droplet is deposited on the surface as in the case of the stagnant contact

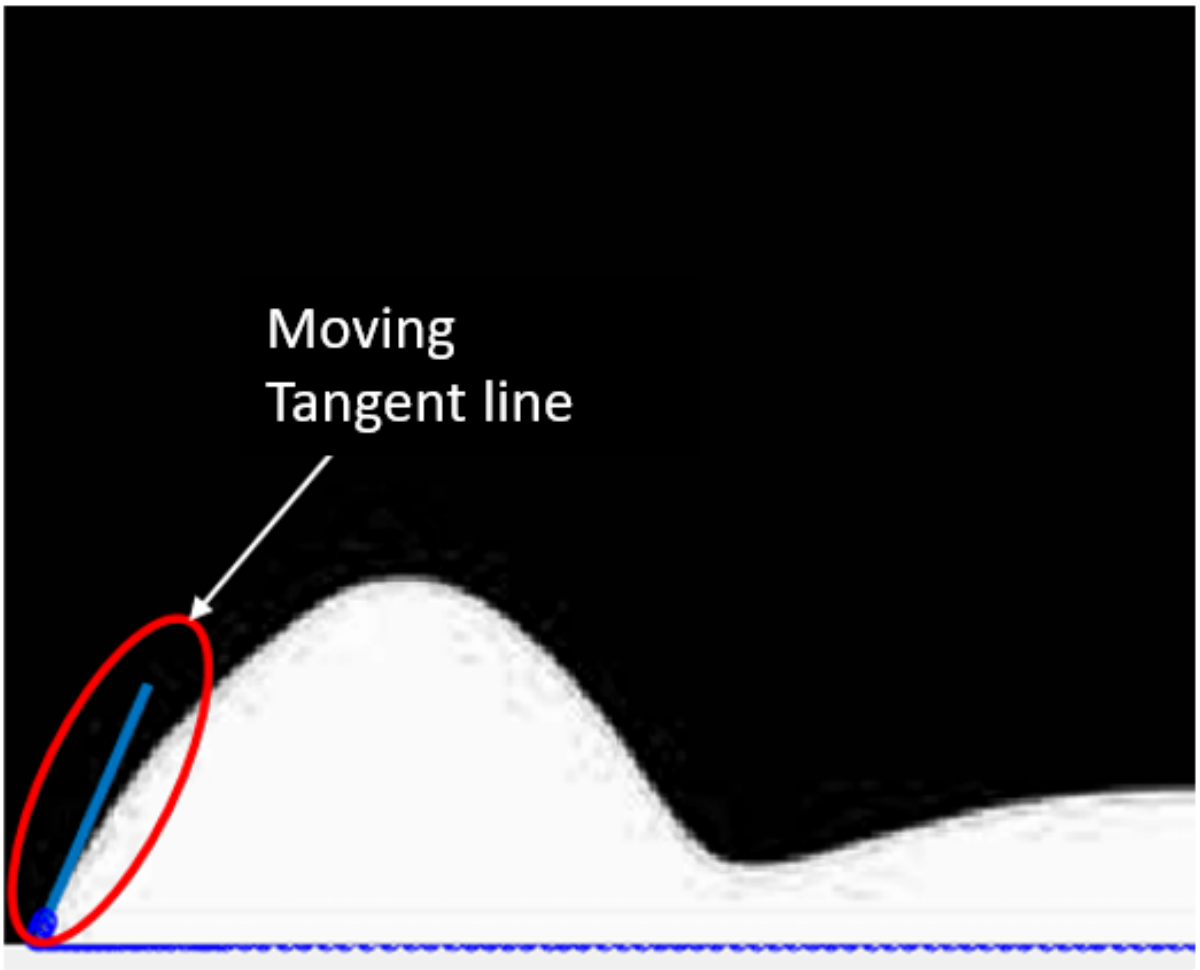

Figure 4.4: Experimental ACA/RCA and stagnant contact angle measurement setup*

angle technique but in this case, the column is tilted to an angle where the droplet begins to slide and the angle on the side of the tilt is known as the ACA and the angle opposite to it is the RCA. The angle at which the droplet starts sliding depends on various factors such as the roughness, surface tension, or droplet diameter, but its physical significance points towards the fact that the gravitational force overcomes the surface tension force, thereby imparting motion to the droplet. Experimental data obtained is post-processed using image processing techniques for which a code is developed. This in-house code is used in determining the moving contact line of the fluid during the spreading and receding phases as seen in figure

4.4, where the blue line denotes the tangent that the moving contact line forms with the substrate. A point-wise interpolation scheme is used to track this MCL as the droplet evolves, with the help of a threshold for the droplet interface determined by the presence of dark and light pixels in the image. The advancing and receding contact angles are calculated based on the position of the droplet in the frame, this data can be compared to the simulation.

Alternative Method

In some cases (mainly for reflective surfaces) where the images from the experimentation consist of a lot of disturbance in resolution or in terms of shadow formation and reflection, an alternative method to the moving tangent line is utilized, which involves the processing of images using the software "ImageJ".

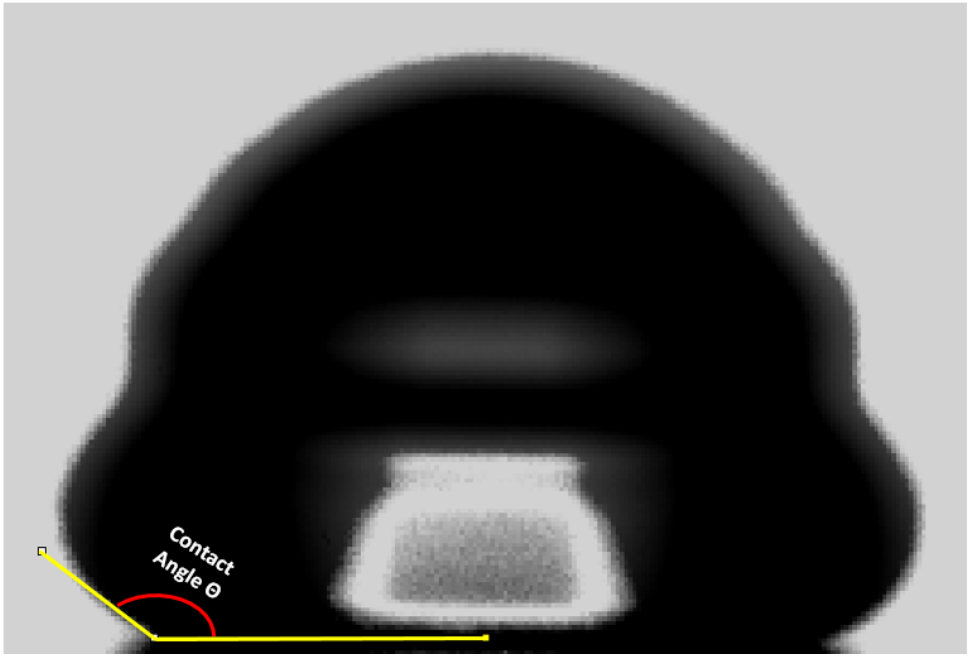

Figure 4.5: Measurement of contact angle of experimental data using image processing tool as an alternative method

As seen in figure 4.5, the method involves the use of the image processing tool where an angle

is created between the surface and the interface between the liquid and vapor. This angle is more accurate than post-processing using "MATLAB" due to the presence of a reflective surface (Aluminum), which hampers the ability of the code to determine the dynamic variation of the contact angle. This methodology involves capturing 5 contact angles at each time interval (total 10 intervals) and averaging them, with uncertainty as seen in tables 4.4 and 4.5 below.

4.3.2 Results

Results obtained from the experiments can be divided into three sub-sections based on the substrate material. As discussed above in the methodology, the behavior of the droplet on the impact on each of these surfaces is unique, which can be classified using the table below.

Table 4.3: Droplet behaviors observed on substrates of different materials

Material	Glass	Aluminum	PETG
Behavior	Deposition	Complete Rebound	Ejection of drop

Uncertainties

Factoring in the uncertainties is an important step in classifying experimental data. Droplet diameter, ACA and RCA are going to be input for the simulation which implies, quantifying their uncertainties from the experiments is crucial to determining their agreement with the simulation. The uncertainties for the mentioned data are specified in the table below:

From the above table 4.4, percentage uncertainties can be estimated for the respective materials.

Table 4.4: Uncertainty quantification of experimental data taken with respect to measurement on the three different materials

Material	**Diameter (mm)**	**ACA (θ_a)**	**RCA(θ_r)**
Glass	2.05 ± 0.05	116.60° ± 2°	66.46° ± 2°
Aluminum	1.99 ± 0.05	145.01° ± 2°	143.08° ± 2°
PET-G	2.08 ± 0.05	123.14° ± 2°	87.37° ± 2°

Table 4.5: Percentage uncertainty of experimental data taken with respect to measurement on different materials

Material	**Diameter Uncertainty**	**ACA Uncertainty**	**RCA Uncertainty**
Glass	2.4%	1.7%	3.0%
Aluminum	2.5%	1.4%	1.4%
PET-G	2.4%	1.6%	2.3%

As seen from table 4.5, all uncertainties lie within a 3% error range which will aid in comparison of the experimental data with the simulations for the three different configurations as seen in table 4.1.

Impact Behavior on Glass

The following table 4.6 describes the experimental configuration specific to droplet impact observed on glass:

On the glass, the expected behavior is observed when there is no etching. This behavior

Table 4.6: Impact parameters results obtained from experiments for glass

Initial Droplet Diameter (mm)	**Initial Droplet Velocity (m/s)**	**ACA** (θ_a)	**RCA** (θ_r)	**Calibration (mm/px)**
2.0593	1.1321	116.6029°	66.46°	0.007973072

majorly corresponds to the contact angle and droplet diameter as will be seen in the series of images in figure 4.6 below.

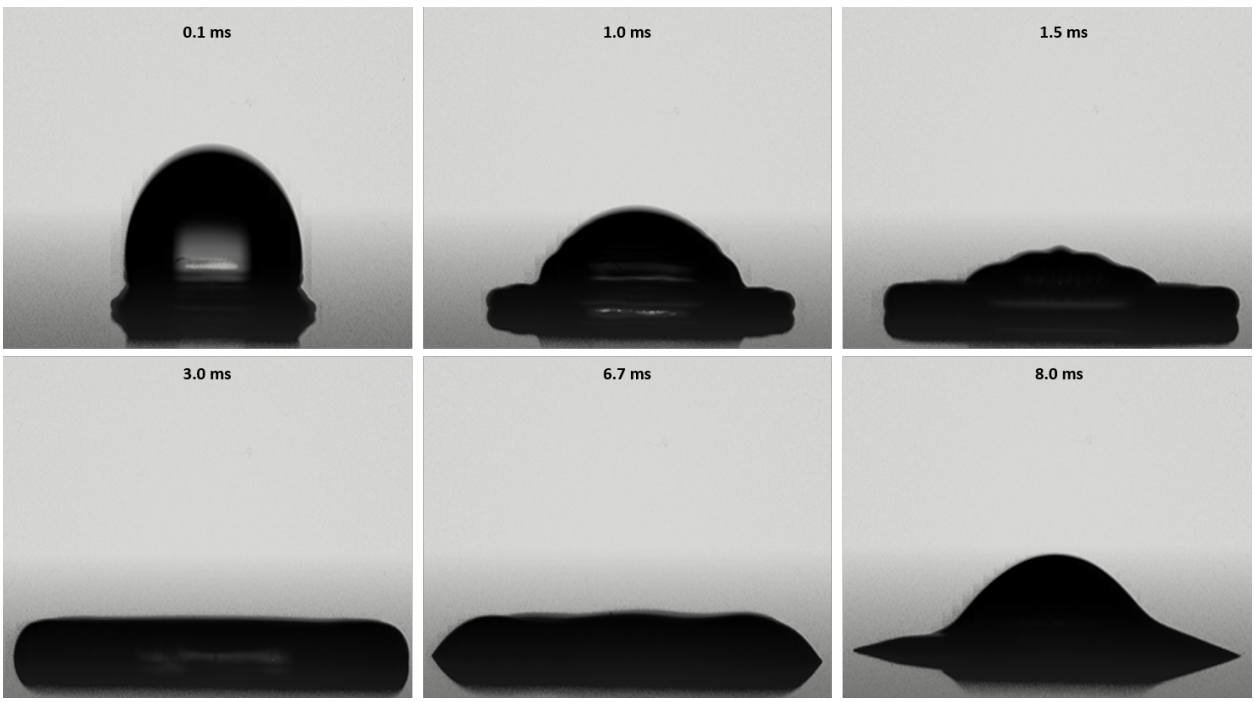

Figure 4.6: Droplet evolution on glass substrate observed in experiments

During the early stages of impact, the droplet spreads as expected on any surface. Before the receding phase begins, the droplet forms a pancake shape, as seen in the image at timestamp 5.0ms, which signifies the maximum diameter of spread for the droplet. The droplet starts to recede and eventually due to the lack of momentum and failure to overcome the surface tension forces, deposits on the substrate as seen at time 11.0ms.

Impact behavior on Aluminum plate

The following table 4.7 describes the experimental configuration specific to droplet impact observed on an aluminum plate: On the aluminum plate, the droplet behavior is similar

Table 4.7: Impact parameters results obtained from experiments for aluminum

Initial Droplet Diameter (mm)	**Initial Droplet Velocity (m/s)**	**ACA** (θ_a)	**RCA** (θ_r)	**Calibration (mm/px)**
1.9999	0.494	145.0164°	143.0890°	0.005270157

to that of a hydrophobic surface, where the droplet does not spread much, thereby keeping its momentum and inertial energy, which allows it to overcome the surface tension adhesive force and rebound completely as seen in figure 4.7 The droplet hence has obtuse contact

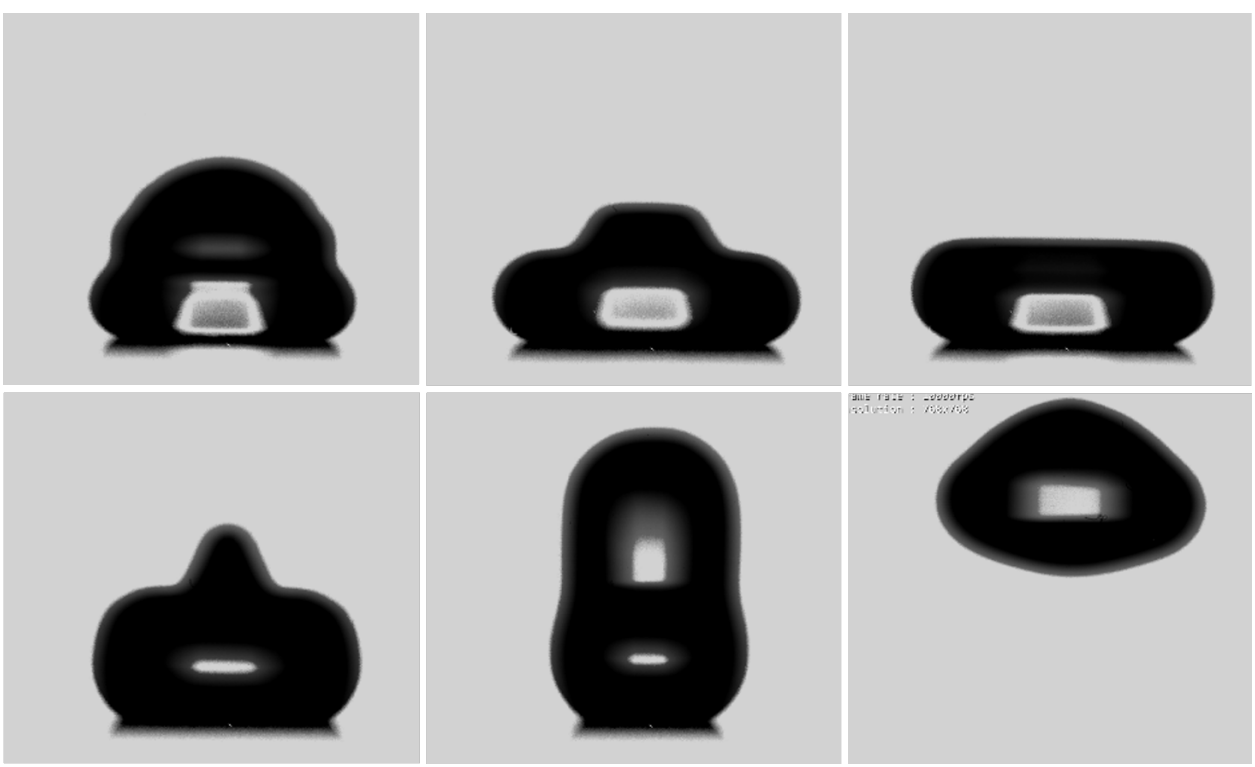

Figure 4.7: Droplet evolution on coated aluminum substrate observed in experiments

angles with the substrate making the surface hydrophobic and low in terms of wettability. This will be compared in chapter 5, where the contact angles obtained from the numerical simulation will be compared to the experiments.

Impact behavior on PET-G plate

The following table 4.8 describes the experimental configuration specific to droplet impact observed on an aluminum plate:

Table 4.8: Impact parameters results obtained from experiments for PET-G

Initial Droplet Diameter (mm)	**Initial Droplet Velocity (m/s)**	**ACA** (θ_a)	**RCA** (θ_r)	**Calibration (mm/px)**
2.0844	0.4902	123.1400°	87.3700°	0.011142018

On the PETG plate, the droplet behavior is similar to the glass until the receding phase. The plastic substrate does not allow the droplet to spread as much as on the glass substrate, thereby maintaining a relatively low droplet diameter and higher contact angles. When receding the droplet has enough inertia and momentum to overcome the viscous forces, but not enough to overcome the surface tension entirely. When the droplet recedes, the momentum from the rim carries into the center which causes a jetting behavior, that leads to a drop ejection as seen in figure 4.8. This phenomenon will be compared in chapter 5 with the numerical simulation.

4.4 Chapter Summary

The experimental set-up derived from the literature explains the different components involved in performing the droplet impact experiment on solid substrates of different materials.

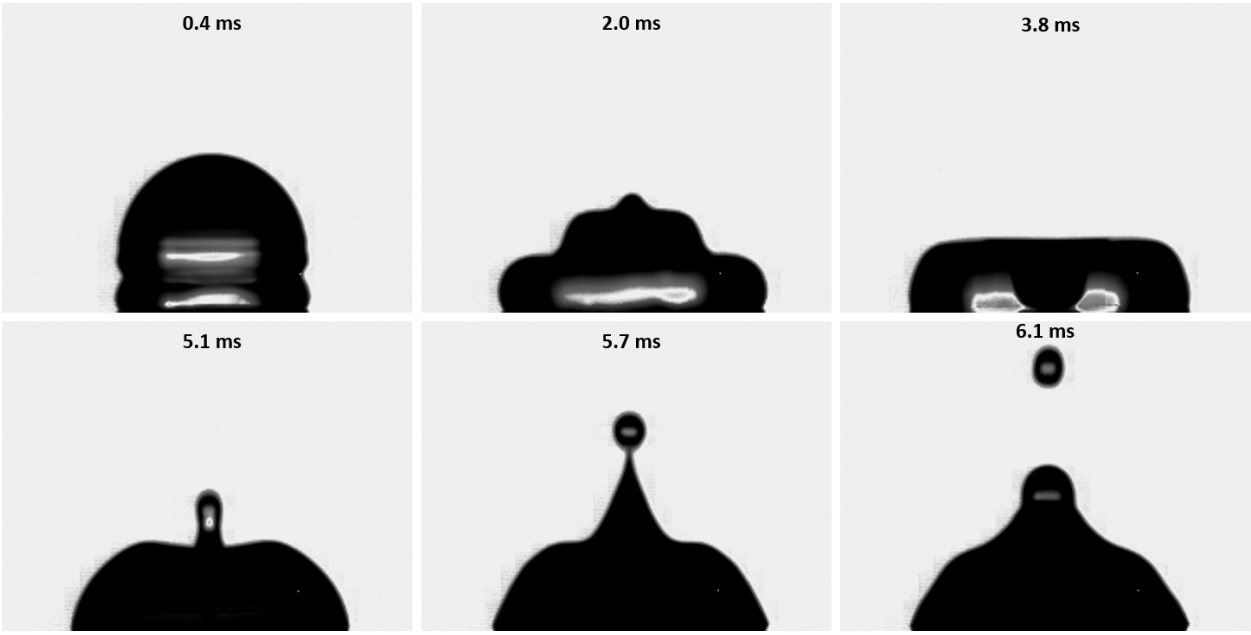

Figure 4.8: Droplet evolution on PET-G substrate observed in experiments

Experimental configurations to be simulated are illustrated and described briefly as seen in table 4.1 along with the methodology used in the processing and acquiring the experimental data seen in figures 4.2, 4.3 and 4.4. Uncertainty quantification performed for the key parameters which will act as input for the numerical simulation reveal errors within a 3% margin as seen in table 4.4, which will help quantify and compare the data obtained from the numerical simulation. Overall, the behavior of droplet impact on three different substrates was observed qualitatively using experimental data and post-processing it. This revealed some interesting results, where in the case of glass there was only deposition of the droplet on the surface of the substrate with lower contact angles on impact when compared to aluminum where a complete rebound was observed with contact angles over 90° throughout and for PETG, where there was an ejection of a drop after the receding phase.

Chapter 5

Numerical Simulation based on in-house experimentation

5.1 Introduction

In this chapter, the numerical simulation developed on StarCCM+, using the methodology mentioned in chapter 2 will be compared with the in-house experimental data. The results of the simulations will be plotted in terms of the diameter evolution, contact angle hysteresis, and droplet spread rate, which will be compared to the literature and the experiments. The model having been validated with Šikalo et al. [67] is expected to perform well and capture the required physical behavior of the droplet in the three different configurations used in gathering the in-house experimental data.

5.2 Numerical Simulation results: Glass

Observations can be made based on the qualitative analysis and comparison of the results obtained from the in-house experiments and numerical simulation on the glass plate.

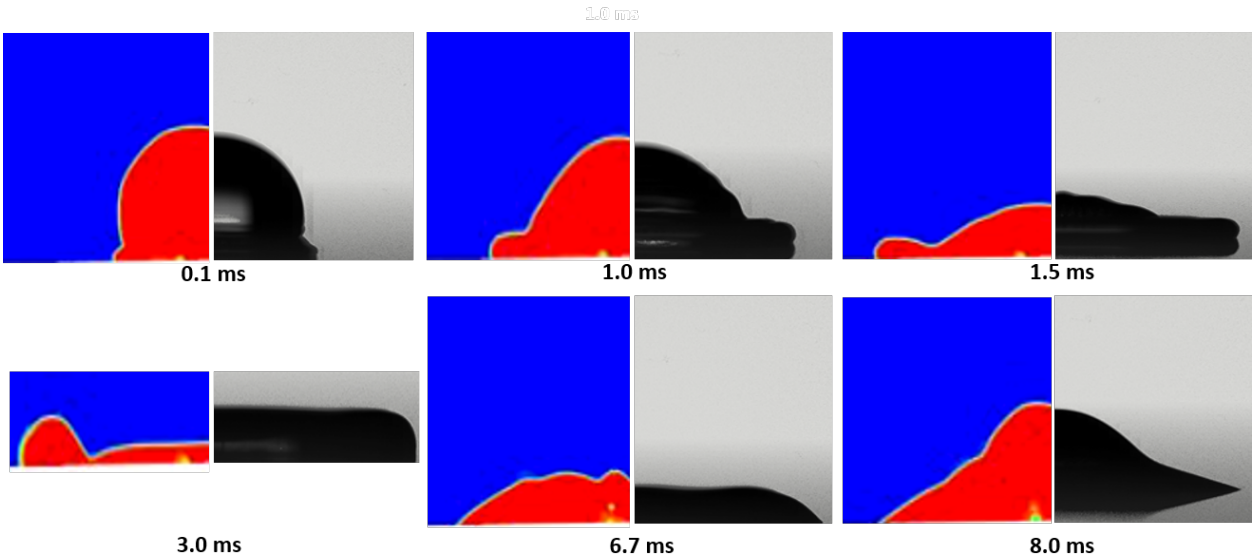

Figure 5.1: Droplet evolution regime based on numerical simulation on glass substrate compared with the experiments at similar time intervals

Qualitative Analysis

Qualitatively observing figures 4.5 and 5.1, images from the corresponding time stamps show similar behavior in both experiments and numerical simulation. Different droplet morphology such as, during the spreading phase, the pancaking on the droplet is seen with the formation of the rims at t = 3.0 ms in the case of the simulation, whereas looking at figure 5.1 at t = 3.0ms formation of rims does take place but due to the position of the camera the center of the droplet is not visible, where the 3D image, does have a rim formation at the edges and a thin lamella at the center. As time progresses the droplet recedes in both cases and eventually deposits on the surface at t = 8.0 ms, proving the conclusion from the experiment about the lack of momentum and inertia when the droplet recedes, which is not able to overcome the surface tension forces, leading to the droplet depositing on the surface of the glass.

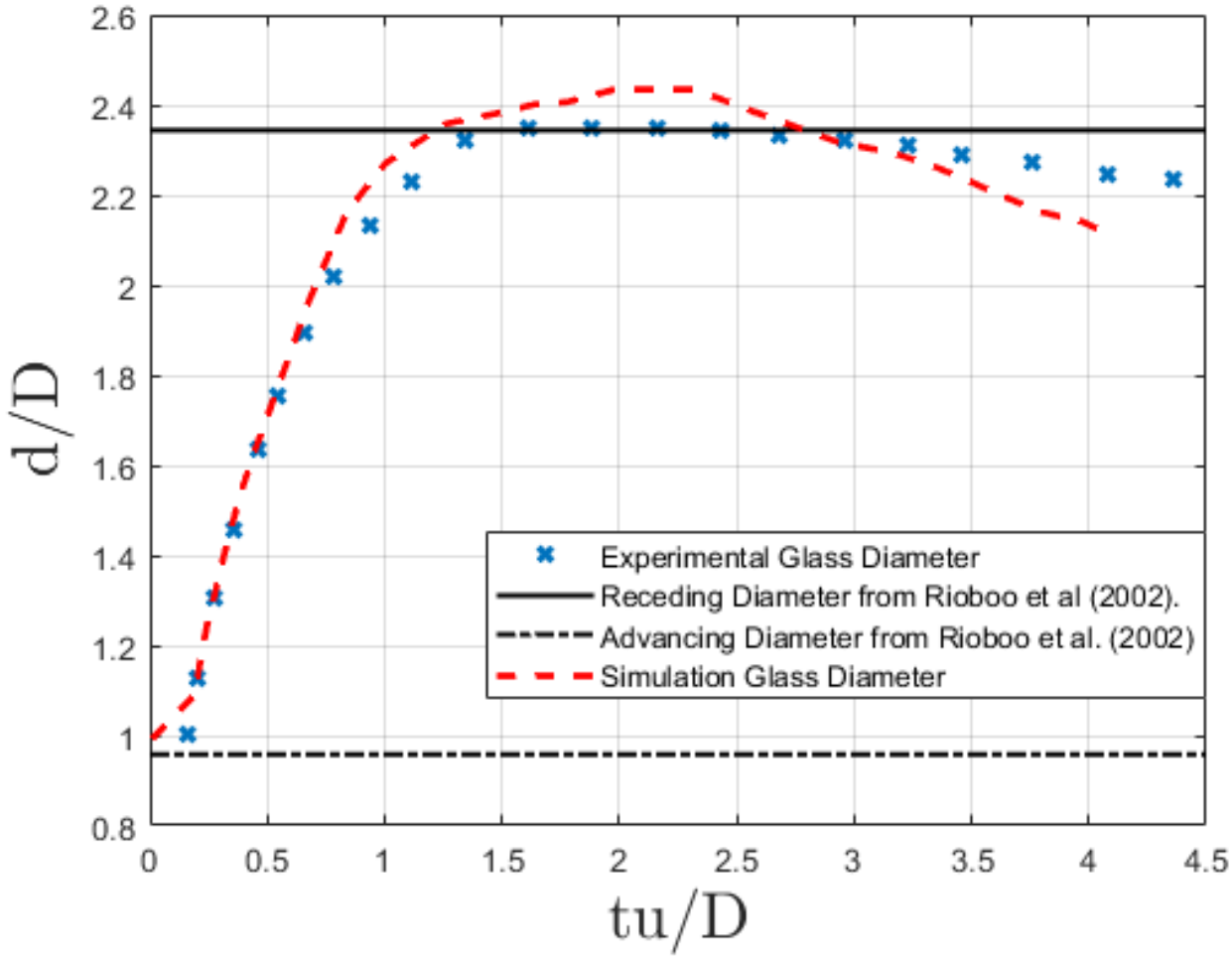

Figure 5.2: Diameter evolution comparison between in-house experiment and numerical simulation for glass substrate

Quantitative Analysis

Quantification of the results obtained from the experiments and numerical simulation will further support the conclusion derived from the qualitative analysis.

As seen in figure 5.2, the diameter evolution from the numerical simulation compares well with the experimental glass diameter evolution for the parametric case specified in table 4.5. Quantitatively speaking an absolute percentage error of 5.52% is found between the

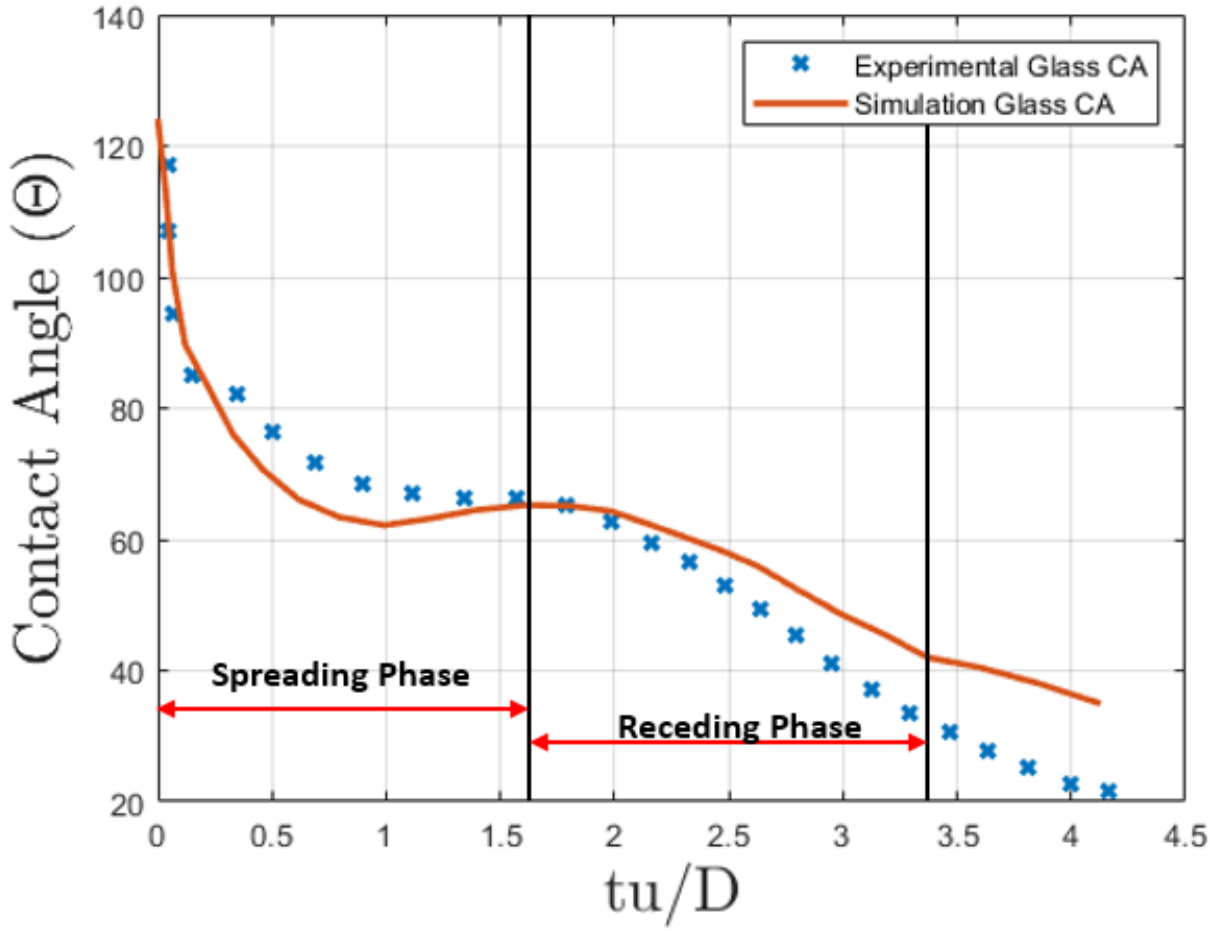

Figure 5.3: Contact Angle evolution comparison between in-house experiment and numerical simulation for glass substrate

simulation and data from the experiment, which shows a good agreement qualitatively and quantitatively, especially considering the propagation of error in the experimental data from the uncertainties as seen in table 4.4. The diameter ratio gives an idea about the spreading and receding of the droplet and does a good job of justifying the evolution of the droplet on impact, another parameter that will be useful in understanding the evolution on different substrates would be the dynamically varying contact angle, which is observed in figure 5.3. The contact angle variation captured by the numerical simulation matches well with the experiments until the receding phase, which explains the similar trend observed in the

evolution images in figure 5.1. As the droplet settles at about $\tau = 3.4 \sim 8.0$ ms, the simulation has the droplet acquire a more traditional deposition with a higher contact angle compared to that of the experiment where the diameter is larger than the simulation which is correlated with the plot in figure 5.2 Similar conclusions to the ones made with respect to the diameter plot are evident in the contact angle plot as well, where it is seen that the contact angle steadies during the spreading stage as the droplet diameter increases, this can be correlated with images in figure 5.1 and the diameter evolution plot in figure 5.2.

Table 5.1: Non-Dimensional parameters evaluated to calculate the maximum spread rates

Non-Dimensional Parameter	We	Re	Oh	Adv. Diameter (d_a)	Rec. Diameter(d_r)
Value	36.2044	2420.7814	0.0025	0.9579	2.3439

Table 5.2: Different maximum spread (β) rate empirical models from the literature compared to the maximum spread rate from numerical simulation

$\boldsymbol{\beta}$	Scheller Bousfield	Pasandideh-Fard et al.	Ukiwe Kwok	Clanet et al.	Roisman	Eggers et al.	**Numerical Model**
Value (d/D)	3.0145 3.1356	2.5720	2.4845	2.4530	2.6328	7.6203	**2.4344**

Further analysis in comparison to the literature asserts the robustness of the model in simulating conditions on a glass substrate. Table 5.4 shows the different empirical maximum spread rate models from the literature that can be used to compare the result obtained from the numerical simulation. The maximum spread rate obtained from the numerical model is 2.4344, which corresponds well with most models except the model formulated by Eggers et al. [16] re-iterated below:

$$\beta = Re^{1/5} f(P)$$

where,

$$P = WeRe^{-2/5}$$

P here is called the impact number, which is affected by the higher We and Re numbers that correspond to ranges at the extremes of the testing configurations mentioned in Eggers et al. [16]. Observing the graph in figure 5.2, the experimental diameter data and the numerical simulation capture the advancing and receding diameters with good precision, however, there is a variation in both diameter and contact angle measurement obtained from the simulation in comparison to the experimental data.

This difference can be attributed to the viscosity of the fluid and the capillary number that is governed by the surface tension and is an important parameter in the simulation. The error in viscosity could be due to the ambient temperature of the surroundings being lower than the room temperature (which is considered in the simulation) and is more prominent due to the low velocity of the impact. The capillary number consists of both viscosity and surface tension forces with the velocity as seen in equation 1.5, contributing to the error in measurement which is visible in the last image at time t = 8.0 ms in figure 5.1, validating the variation in contact angles measured by the numerical simulation and the experiments.

5.3 Numerical Simulation Results: Aluminum plate

Simulation agrees well with the experimental data and produces a complete rebound in the case of the aluminum substrate.

Qualitative Analysis

Qualitatively observing the image sequences in figures 4.7 and figure 5.4, images at the corresponding time-stamps show behavior that resembles each other. Droplet contacts the surface and starts advancing at time t = 1.0 ms and continues to advance until t $\sim$ 4.7 ms, whilst having contact angles greater than 90° throughout the advancing stage. The diameter of the droplet captured by the simulations is observed to be relatively lower than the simulation which will be analyzed and investigated quantitatively. During the receding phase, the droplet significantly reduces in diameter in both cases, which points towards excess momentum and the force of inertia that is overcoming the surface tension and viscous forces to aid the droplet to recede quicker. This quick receding motion of the droplet propagates into the center and causes a jet which due to the surface being hydrophobic leads to a complete rebound of the droplet as seen at time t = 13.2 ms in figure 5.4. Quantitatively

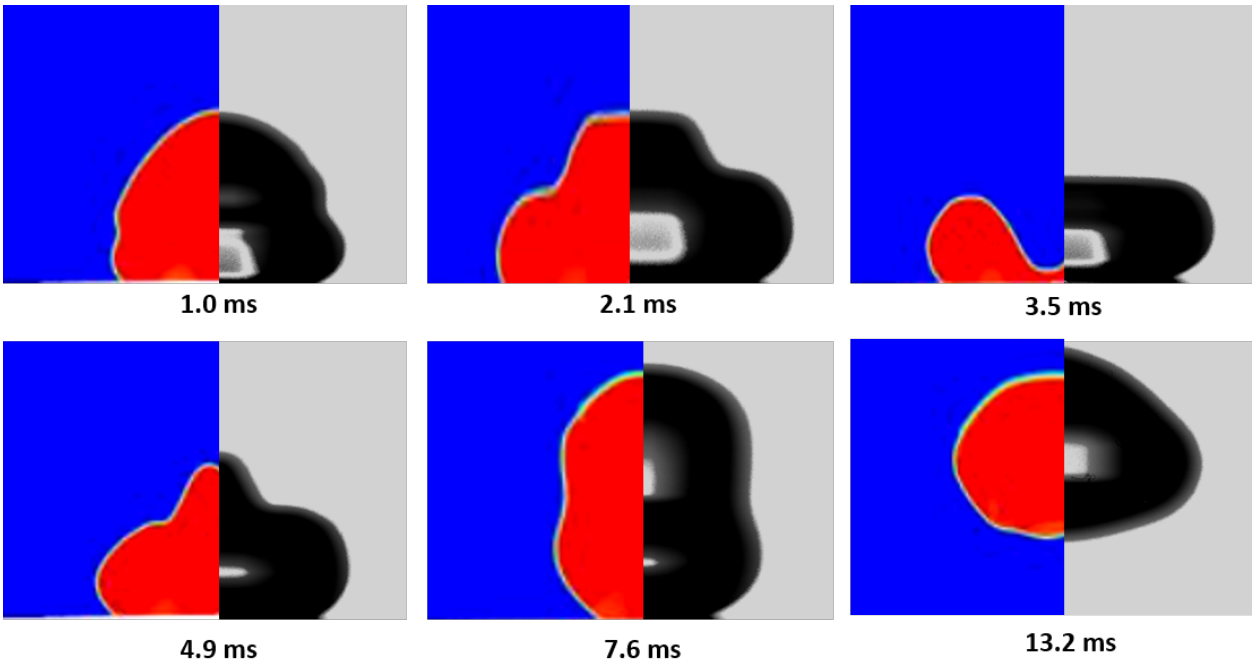

Figure 5.4: Droplet evolution regime based on numerical simulation on aluminum substrate compared with the experiments at similar time intervals

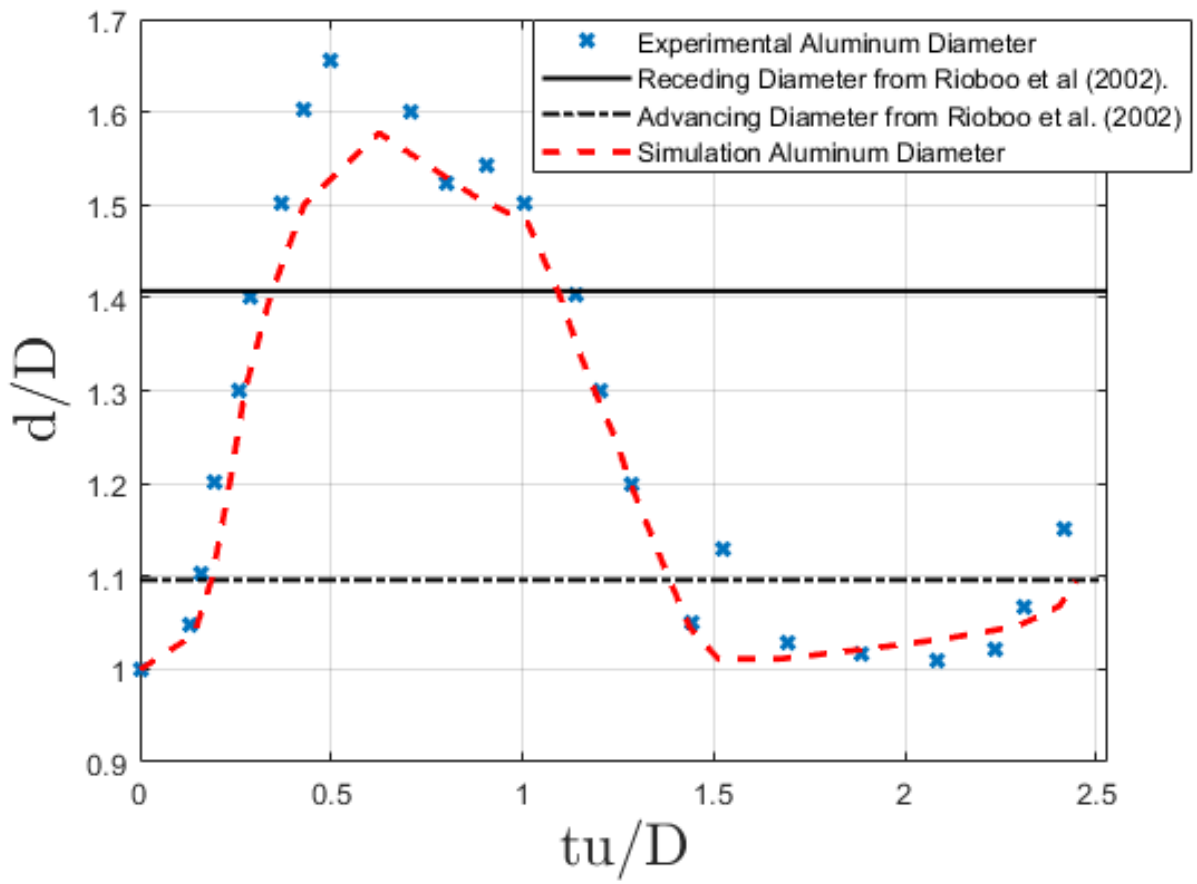

Figure 5.5: Diameter evolution comparison between in-house experiment and numerical simulation for aluminum substrate

looking at the data will reveal further details about the physics of the behavior and the effectiveness of the model in replicating the behavior.

Quantitative Analysis

As observed from figure 5.4, the evolution of the droplet is captured to a close degree by the simulation which can be seen in terms of the diameter variation over time from the graph in figure 5.5. Droplet diameter evolution data obtained from the simulation follows a similar trend to that of the experiments showing good agreement in both advancing and

receding stages. The data for the receding droplet diameter and the advancing droplet diameter obtained from the literature (Rioboo et al. [40]) reveals that the droplet must start advancing at d/D = 1.1, which is the case in terms of both the simulation and the experiment, however, both simulation and experiment fail to agree with the literature in terms of the receding phase diameter of d/D = 1.4073. There are multiple factors that come into the picture when considering the receding diameter that has not been included by Rioboo et al. [40] in the empirical relation (equation 1.8, re-iterated below) provided in the literature -

$$\frac{d_i}{D} = 2[\frac{sin^3\theta_i}{2(1-cos\theta_i)(2-cos\theta_i-cos^2\theta_i)}]^{1/3}$$

The equation does not account for the material properties such as the viscosity and density of the fluid, it is known that any slight change in temperature drastically changes the magnitude of dynamic viscosity, which could be a factor that affects the behavior of the droplet. Apart from the viscosity, the velocity of the droplet plays a major role in this case where, a slight variation in the velocity will have an impact on the inertial energy imparted to the droplet on impact, which is not accounted for by Rioboo et al. [40].

The diameter of the droplet reduces from $\tau = 1$, all the way until $\tau = 1.5$ which shows the receding phase and combined work of the surface tension and inertial forces. However, at $\tau = 1.5$, the diameter begins to increase again as the droplet forms a shape as seen at time t = 7.6 ms in figure 5.4, as a result of the excess energy imparted to the center of the droplet. The diameter increases to a value of d/D $\sim$ 1.1, before it detaches from the surface at $\tau = 2.5$. Contact angle variation portrays similar impact behavior of the droplet both in the case of the experiment and numerical simulation. The contact angle is seen to be rising steadily throughout the simulation and experiments which is the case when looking at the time evolution of the droplet in figure 5.4. The overall trend of the contact angle matches well with the experimental data although fluctuations can be seen in the data obtained

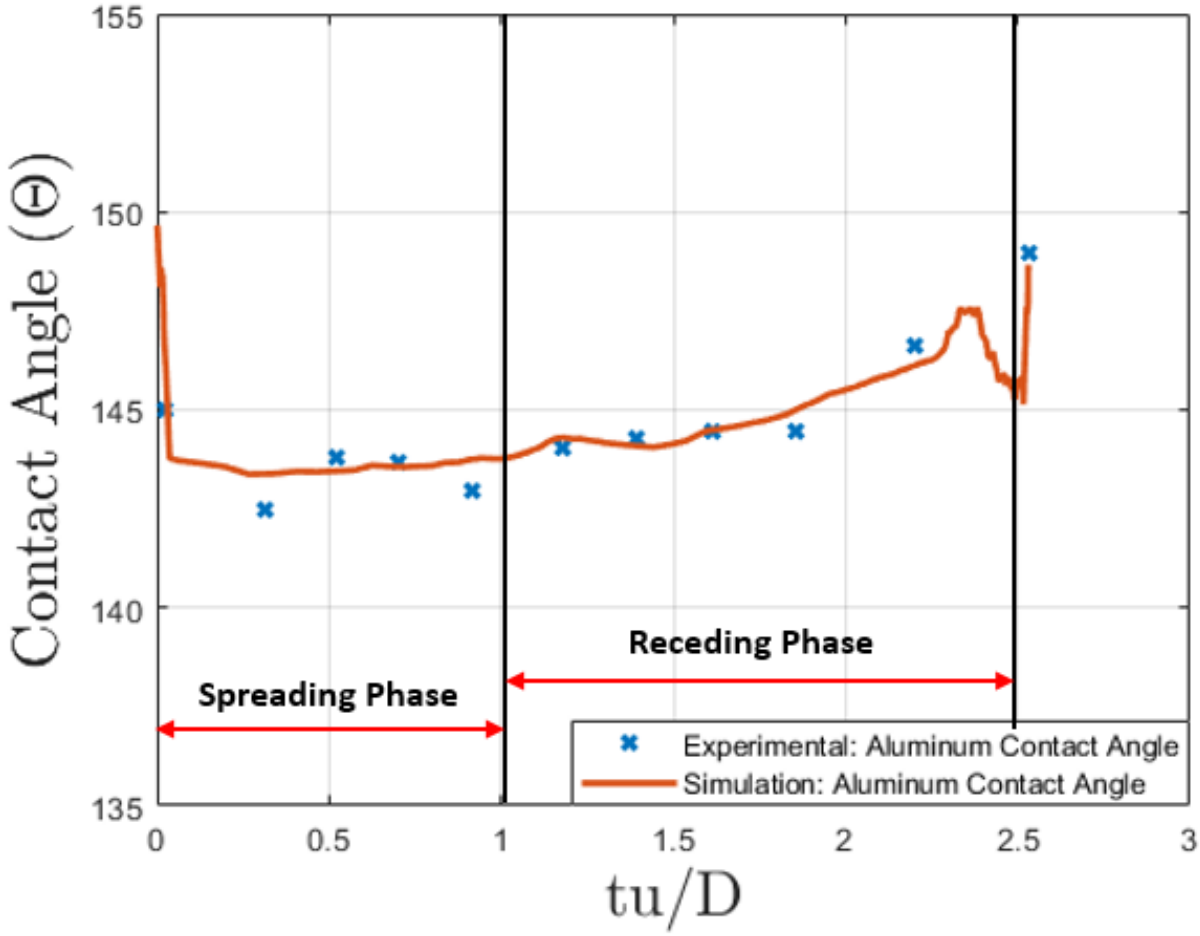

Figure 5.6: Contact Angle evolution comparison between in-house experiment and numerical simulation for aluminum substrate

from the numerical simulation between $\tau = 2.2$ to $\tau = 2.6$. These fluctuations lie within the error experimental error bounds obtained from the uncertainty quantification from table 4.5, where a fluctuation of around 2° is within an acceptable range. The trend shown by the contact angle further supports the observations made qualitatively and supports the droplet diameter evolution data obtained from the numerical simulation.

Table 5.3: Non-Dimensional parameters evaluated to calculate the maximum spread rates

Non-Dimensional Parameter	We	Re	Oh	Adv. Diameter (d_a)	Rec. Diameter(d_r)
Value	6.6917	1025.8559	0.0025	1.0962	1.4073

Table 5.4: Different maximum spread rate(β) empirical models from the literature compared to the maximum spread rate from numerical simulation

$\boldsymbol{\beta}$	Scheller Bousfield	Pasandideh-Fard et al.	Ukiwe Kwok	Clanet et al.	Roisman	Eggers et al.	**Numerical Model**
Value (d/D)	2.2696 2.1104	1.7233	1.4455	1.6084	1.0055	1.6725	**1.5774**

The maximum spread rates obtained from the literature are in good agreement with the maximum spread rate obtained from the numerical simulation which is $\beta = 1.5774$. As observed in the case of the glass substrate, Ukiwe and Kwok [56]'s, Clanet et al. [11] and Pasandideh-Fard et al. [33] are a good match with the numerical simulation, Eggers et al. [16] also resembles the maximum spread rate obtained from the numerical simulation, showing that it might be a good model for impacts at lower We numbers and higher contact angles.

5.4 Numerical Simulation Results: PETG plate

PETG shows the unique behavior of droplet jetting in the experiments but is not captured accurately in the simulation. This behavior will be important in determining the major effects of the contact angle variation on the evolution of the droplet.

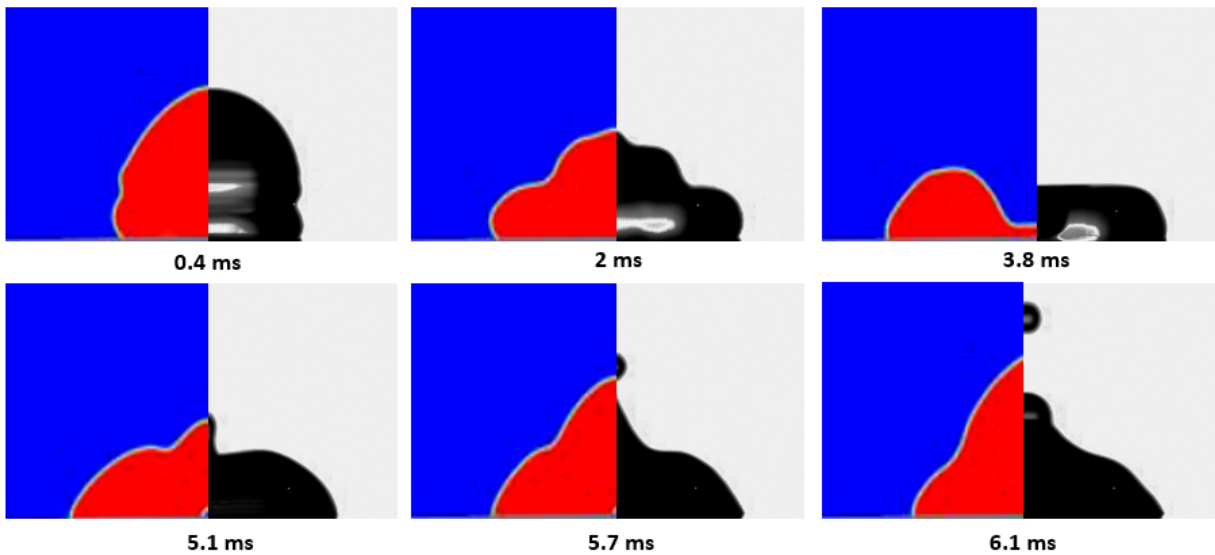

Figure 5.7: Droplet evolution regime based on numerical simulation (color) on PET-G substrate compared with the experiments (grayscale) at similar time intervals

Qualitative Comparison

Observing the time variation in figure 5.7, the numerical simulation compares relatively well with the experiments in the advancing phase where the droplet is spreading. At time t = 2 ms, the droplet observed in the experiment is almost identical to the simulation, showing the robustness of the numerical model during the spreading phase. However, as the droplet reaches its maximum spread (β), it begins to recede at about t = 5 ms, where observations from figure 5.7 show an evidently lower diameter in case of the simulation, which propagates throughout the receding phase and begins to make a difference in the behavior of the droplet

as the experiment observes a jetting behavior. The droplet behavior in the numerical simulation points to the fact that the droplet did not have enough energy to overcome the resistive forces which would be the viscous and surface tension force. The difference in behavior is quantitatively looked at in the next section where the droplet diameter evolution, contact angle evolution, and the Max spread diameter are compared to the experiment and literature respectively.

Quantitative Comparison

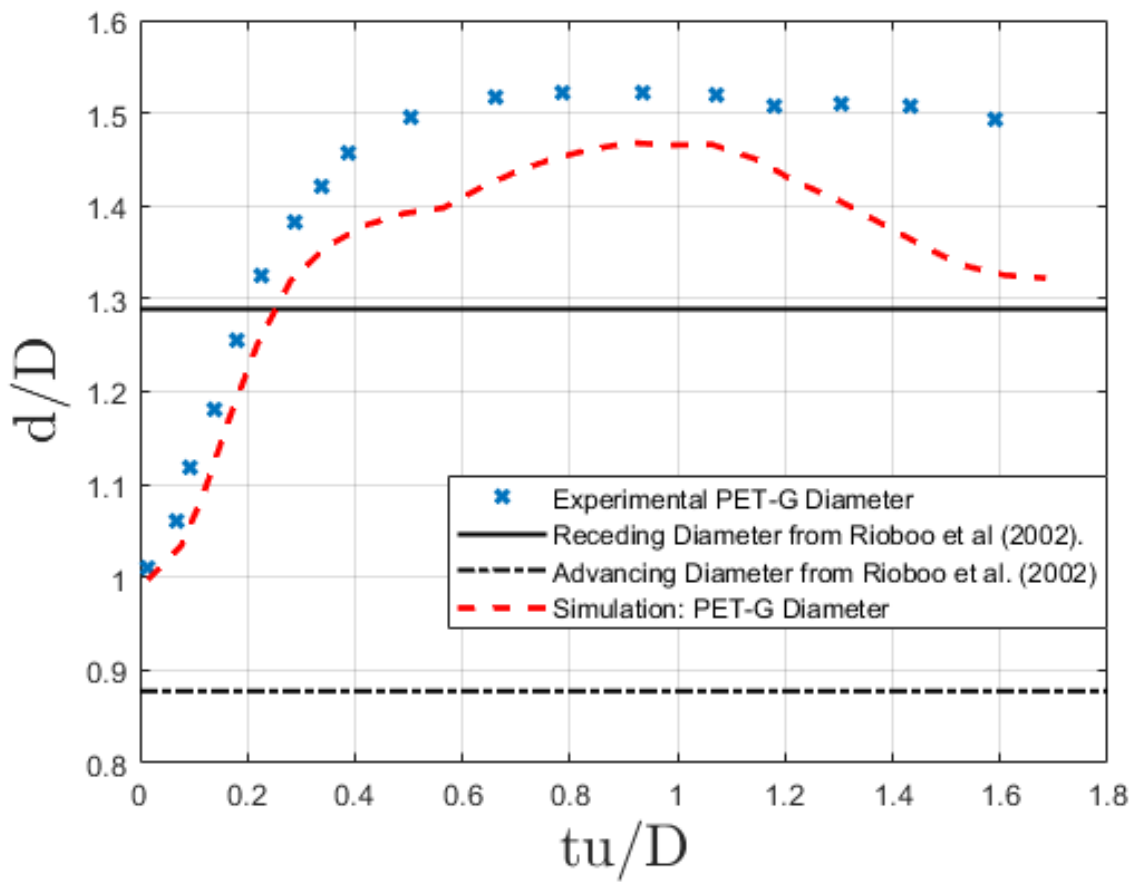

Figure 5.8: Diameter evolution comparison between in-house experiment and numerical simulation for PET-G substrate

Similar to the case of aluminum the surface of PET-G has an initial advancing contact angle of close to 130°, which does not allow easy wetting of the surface by the droplet. However, the surface is not hydrophobic considering, the $\Delta\theta$ between the advancing and receding contact angle to be high, which is around 36°, meaning the surface is wettable after the initial contact with the droplet.

Observing the trend from figure 5.8 for the droplet diameter evolution plotted for the experiment and the numerical simulation, the droplet shows a steady rise in diameter throughout the spreading phase, which is validated when compared to the images shown in figure 5.7. The variation in droplet diameter could be due to multiple factors, including the contact angle and velocity of the droplet on impact. With uncertainty in quantifying the diameter data obtained from the experiments a difference between the numerical simulation and the experiment is expected, which propagates throughout the simulation. A 6% variation is observed between the numerical diameter and the experimental data, during the spreading phase, which is deemed to be a combination of the variation in input parameters and the uncertainty in measurement from the experiments, due to the lower resolution and shadows formed on the surface on capturing the image.

Table 5.5: Non-Dimensional parameters evaluated to calculate the maximum spread rates for PET-G substrate

Non-Dimensional Parameter	We	Re	Oh	Adv. Diameter (d_a)	Rec. Diameter(d_r)
Value	6.9776	1069.2005	0.0025	0.8774	1.2888

Table 5.5 shows the non-dimensional parameters that are crucial in determining the physics behavior of the simulation. As was seen in the case of aluminum, the droplet impact in the case of PET-G is also performed at a lower We number and correlating to the findings from the case of aluminum, Ukiwe and Kwok [56] and Clanet et al. [11] are the empirical models

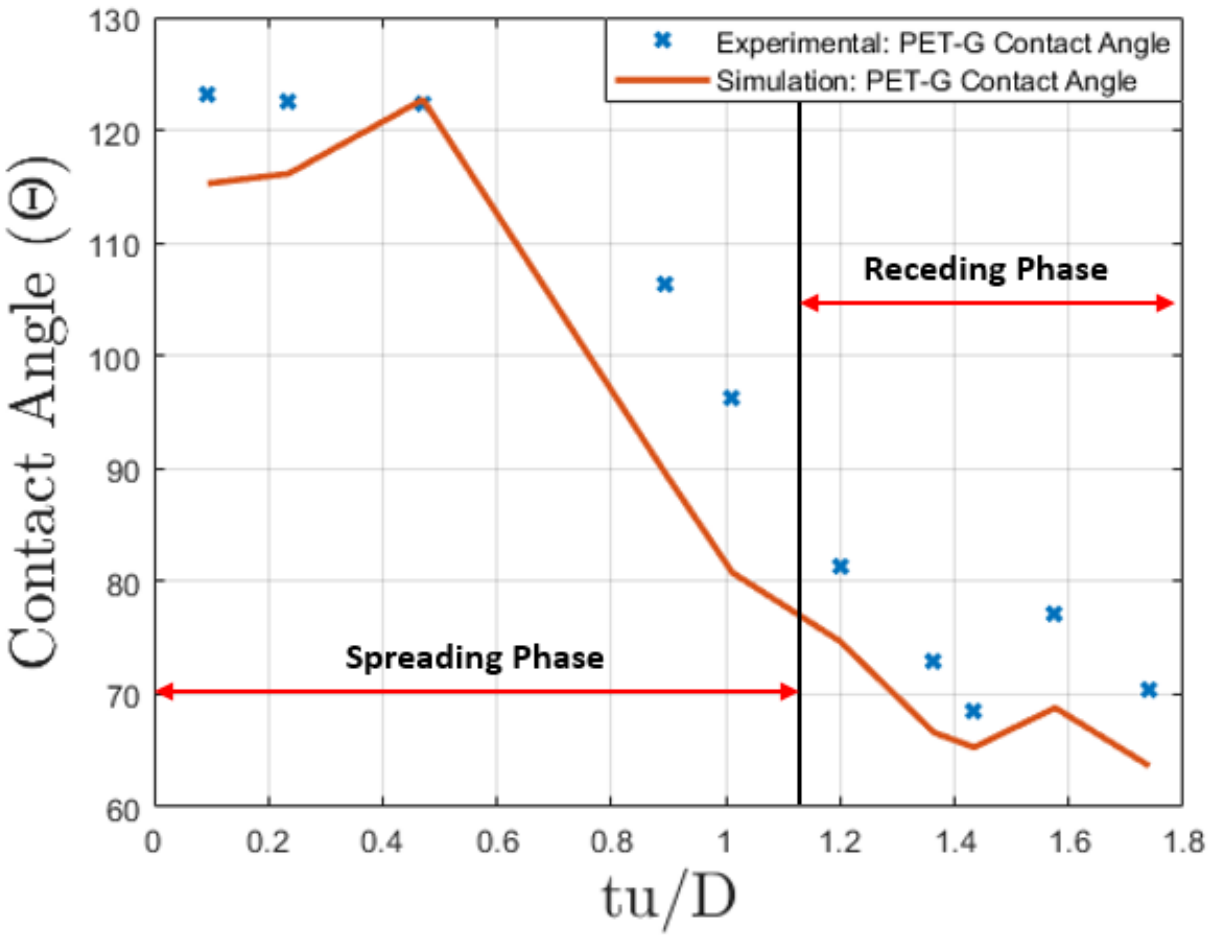

Figure 5.9: Contact Angle evolution comparison between in-house experiment and numerical simulation for PET-G substrate

Table 5.6: Different maximum spread rate(β) empirical models from the literature compared to the maximum spread rate from numerical simulation for PET-G substrate

β	Scheller Bousfield	Pasandideh-Fard et al.	Ukiwe Kwok	Clanet et al.	Roisman	Eggers et al.	**Numerical Model**
Value (d/D)	2.2934 2.1371	1.8586	1.5936	1.6253	1.0451	1.7294	**1.5218**

from literature that closely resemble the maximum spread obtained from the numerical simulation, showing their capability to be able to determine the maximum spread for a

larger range of We numbers, when compared to the other models. The advancing and receding diameter are derived by Rioboo et al. [40] (equation 1.8) based on the advancing and receding contact angles. As discussed in the previous section, conclusions regarding the advancing and receding diameter can not be made independent of the physical and material properties of the fluid such as the viscosity, velocity, diameter of the droplet, etc., adding to errors in input parameters.

Looking at figure 5.9 further justifies the point where the droplet begins to change its behavior in the simulation when compared to the experiment, where a drop ejection occurs. This phenomenon is consistent with the graph in figure 5.8 for the droplet diameter where the simulation under-predicts the diameter meaning there is a resistive force that prevents the droplet from spreading any further than the receding diameter of ~ 1.52. A similar behavior is observed in the graph in figure 5.9 for the contact angle variation, where the angles are lower in the case of the simulation when compared to the experiments, which points to the fact that there is lower energy present in the system after the spreading phase. As described in section 5.2, the Capillary number plays a major role in the determination of the contact number which consists of the velocity, surface tension, and dynamic viscosity of the fluid, all of which parameters are kept constant. The variation of the environment in which the experiments have been performed leads to a significant change in viscosity as established previously, making it a major source of error. The trend observed for the diameter evolution and the contact angle evolution between the experiment and the simulation is identical as seen in figures 5.8 and 5.9. However, it is known that the viscosity acts as an opposing force during the spreading and receding phases of the droplet, which explains the lower overall diameter and contact angles. Due to the loss in energy to the opposing viscous force, the droplet in the numerical simulation loses momentum that it can impart to the center of the droplet and is not able to capture the jetting behavior that is observed in the experiments.

5.5 Chapter Summary

Three different materials are experimented upon and simulations are carried out to observe the impact behavior of droplets on these substrates. Unique behavior is observed on all three substrate materials with the droplet depositing on the surface of the glass, rebounding completely on the aluminum, and providing a partial drop ejection in the case of the PET-G substrate. Observations show good agreement between the simulation and the experiments when taking into consideration the ACA and RCA for cases of glass and aluminum. This suggests the effectiveness of the blended Kistler method in modeling droplet evolution on any substrate where input parameters and material properties are accurately specified. However, in the case of PET-G, the numerical simulation is unable to capture the droplet evolution in the receding phase, which is attributed to the uncertainty in viscosity, impact velocity, ACA, and RCA along with uncertainty in material properties due to the change in the experimental environment (as all experiments were not performed at the same time).

Chapter 6

Conclusion and Future Work

6.1 Conclusion

The analysis of droplet impacts on solid substrates as stated before is considered a prerequisite for understanding the phenomenon of the droplets impacting on super-cooled surfaces that will be crucial in developing more effective methods for de-icing.

The experiments performed are to understand the effect of various different surfaces and their wettability on the behavior of the droplets on impact. Different behaviors were observed when a droplet of approximately the same diameter was impacted on the surface.

Part - I

Before, understanding the effect of these droplets impacting on different materials, the computational model developed in-house was compared to experimental data obtained by Šikalo et al. [67]. The model involved the use of the VOF function to model multiphase flows coupled with an MCL model, the Blended-Kistler model which uses the ACA and RCA to calculate the dynamically varying contact angle with respect to time. Preliminary validation of the model successfully performed revealed a good match between the experimental data obtained from Šikalo et al. [67], the numerical calculation by Šikalo et al. [67] with the numerical simulation performed on StarCCM+. Validation performed involved the variation

of CFL and grid refinement as seen in tables 3.4 and 3.5. The following tables assist in concluding the effect of CFL on the accuracy of the solution. It is observed that a CFL number of 0.1, is most accurate in capturing the droplet diameter evolution in comparison to the experiments. In the case of the droplet height, all CFL numbers are within an error range of 5%, making it redundant for comparison purposes.

Similarly, table 3.8 shows the error between the numerical simulation and the experiments when the grid refinement level is varied. Conclusions can be made on the level of refinement that would be most computationally effective and viable in the validation of the model. It is seen that refinement level 2 has an error of 29.37% when compared to refinement levels 3 and 4 where, the percentage error reduces to 8.06% and 7.81%, putting them in a similar range to that observed with CFL 0.1. Thus, it can be concluded that a refinement level of 3 or higher must be used in order to accurately model the physical behavior of the droplet. All simulations were run using 8 Nodes and 32 CPUs per node. Following were the wall times observed for the various CFL iterations:

Table 6.1: Wall-time variation of the simulation case for different CFL numbers

CFL	0.1	0.2	0.3	0.4	0.5
Wall-Time (Hrs.: Mins.)	7:24	4:14	3:57	3:48	3:22

The CFL number is kept constant at 0.1, for all the variations in grid refinement levels that have been simulated as seen in table 6.2 below.

Table 6.2: Wall-time variation of the simulation case for different refinement levels

Refinement Level	2	3	4
Wall-Time (Hrs. : Mins.)	2:33	7:18	16:02

Hence, looking at the wall times from the tables above, it is evident that a CFL of 0.1, coupled

with a grid refinement level of 3 accounts for the best set-up in terms of computational cost and accuracy of the simulation. This is the set-up that is suggested for usage in terms of low-velocity droplet impacts on most solid substrates that are non-hydrophobic in nature. Meaning, the use of refinement level 4 might be beneficial to simulate impact behaviors that resemble complex flow patterns such as jetting or rebounding.

Part - II

After setting up the model and completing its preliminary validation, numerical simulations were performed to simulate the impact behavior of in-house experiments performed at the cavitation and multi-phase flow laboratory at Virginia Tech. This aided in understanding the robustness of the model when it comes to capturing droplet impact behavior of different types. Three different cases have been considered as seen in table 4.1.
Each of these three cases portrays different behavior on impact with a case causing droplet deposition (Glass), a case of droplet rebounding completely (Aluminum), and a case consisting of a drop ejection (PET-G).

For the Glass substrate, the droplet is able to identify and capture the characteristics of impact to a good degree, with a similar trend observed in both the droplet diameter evolution and the contact angle variation between the simulation and the experiments as seen in the figures 5.2 and 5.3. The numerical model reveals a maximum spread diameter of d/D = 2.4344, which is in good agreement with the literature sources as seen in table 5.4, with a receding diameter $d_r/D = 2.3439$ and advancing diameter of $d_a/D = 0.9579$, that also agree well with the results obtained from the simulation. Overall, the model captures the droplet evolution on a glass substrate with great accuracy until the drop deposition begins, where a wedge-type shape is formed at time t = 8.0 ms, as seen in figure 5.1, which attributes to the variation in the droplet diameter and contact angle measurements between the simulation

and the experiments at that time level. This error originates mainly from the tool used to analyze the contact angle, diameter, and measurement technique used in capturing droplet images on a glass substrate. All of these factors contribute to the error propagating into the simulation with average uncertainties of 2.38% for glass, 1.76% for aluminum, and 2.09% for PET-G.

For the Aluminum substrate, there is again good agreement between the simulation and the experiments as seen in the droplet evolution images that are compared side by side for the experiment and the numerical simulation in figure 5.4. However, it is evident that the numerical simulation somewhat under-predicts the diameter of the droplet which leads to certain fluctuations in capturing the contact angles during the receding phase. For the case of aluminum, the maximum spread diameter obtained from the numerical simulation is 1.5774, which is in agreement with most models and within the range provided in the literature, meaning the behavior of the droplet is simulated to a good extent. The receding diameter in the case of the simulation is higher in comparison to the diameter of 1.4073, obtained from the literature, while the advancing diameter is lower when compared to the literature. The model's empirical models do not account for the physical properties such as dynamic viscosity and surface tension forces that might be acting on the surface, this can lead to the variation that is seen between the experiments, simulation, and the literature as explained in the results section.

For the PET-G substrate, the simulation captures the advancing stage of the droplet on impact to a good degree of accuracy but obtains slightly different results when compared to the experiments as seen in the droplet evolution image in figure 5.7. The quantitative comparison shows the numerically obtained maximum spread $\beta = 1.5218$, which is in agreement with three of the models in the literature that accurately captured the droplet impact behavior on the previous two substrates of glass and aluminum. This means the simulation

does a good job of predicting the maximum spread rate but fails to exactly replicate the behavior of the droplet during the receding phase. Observations from figure 5.8 and 5.9 show that the trend observed between the experiments and the simulations are similar but there is a variation in the diameter and contact angles, which are correlated with the loss in inertial energy during the receding phase, the droplet does not expand as much as expected in the literature and points to the presence of a resistive force. The capillary number is a major factor in providing the simulation with the contact angle variations that govern the models. Capillary number as a function of dynamic viscosity, surface tension, and velocity causes the difference in behavior, with viscosity being a major contributor as established in the results section.

Overall, the model captures the essence of the droplet impact behavior with accurate trends for generic cases. The model is robust enough to perform complex calculations for different cases while capturing accurate trends. It can be concluded that the model seems to differ in accuracy when compared to the experiments for cases with impact on hydrophobic surfaces where the importance of surface tension and viscosity play a major role in determining the impact behavior of droplets on solid substrates.

6.2 Future Work

The phenomenon of aircraft icing is a major hurdle still in the aviation industry and understanding the physics of how droplets impact surfaces, its advantages, and disadvantages can be classified to determine efficient methods to aid in the development of de-icing or anti-icing techniques. An experiment can be designed to modify the existing set-up in-order to incorporate the thermal effects of the surroundings and the surface on the behavior of the droplet when impacted. This technique will help understand scenarios of when a droplet freezes

and classify the effect of temperature. The current computational model can be modified to incorporate the thermal effects with the addition of super-cooled surfaces, which will get the project closer to its goal of simulating an actual icing environment where SLDs are impacted on solid substrates. A de-icing technique currently being looked at in the lab involves the use of vibrations to atomize droplets immediately on contact with the surface, it will be interesting to observe the effect of these vibrations at different frequencies and amplitudes in effectively being able to atomize the whole droplet. Comparison for the numerical model can also be made to the vibrations set-up, vibrations can be induced into the domain, to mimic that of a cantilever beam, and simulations can be performed to understand the effect of vibrations on the droplet impact. Furthermore, a coupled experiment with vibrations and thermal effects can be performed to determine different scenarios that can be simulated to observe droplet behavior on impact with variations of temperature, frequency of vibration, and amplitude. These steps will lead to a closer approximation to the actual environment observed in the case of aircraft icing. The major inhibitor currently is the impact velocity that does not reach realistic levels of droplet impact velocities when aircraft icing occurs at higher altitudes and speeds.

Bibliography

[1] S. Afkhami and M. Bussmann. Height functions for applying contact angles to 2d vof simulations. *International Journal for Numerical Methods in Fluids*, 57:453–472, 6 2008. ISSN 02712091. doi: 10.1002/fld.1651.

[2] S. Afkhami, S. Zaleski, and M. Bussmann. A mesh-dependent model for applying dynamic contact angles to vof simulations. *Journal of Computational Physics*, 228: 5370–5389, 8 2009. ISSN 10902716. doi: 10.1016/j.jcp.2009.04.027.

[3] Kai Bao, Yi Shi, Shuyu Sun, and Xiao Ping Wang. A finite element method for the numerical solution of the coupled cahn-hilliard and navier-stokes system for moving contact line problems. *Journal of Computational Physics*, 231:8083–8099, 10 2012. ISSN 10902716. doi: 10.1016/j.jcp.2012.07.027.

[4] Ilker S. Bayer and Constantine M. Megaridis. Contact angle dynamics in droplets impacting on flat surfaces with different wetting characteristics. *Journal of Fluid Mechanics*, 558:415–449, 7 2006. ISSN 14697645. doi: 10.1017/S0022112006000231.

[5] James C. Bird, Rajeev Dhiman, Hyuk Min Kwon, and Kripa K. Varanasi. Reducing the contact time of a bouncing drop. *Nature*, 503:385–388, 2013. ISSN 14764687. doi: 10.1038/nature12740.

[6] Daniel Bonn, Jens Eggers, Joseph Indekeu, and Jacques Meunier. Wetting and spreading. *Reviews of Modern Physics*, 81:739–805, 5 2009. ISSN 15390756. doi: 10.1103/RevModPhys.81.739.

[7] P. Brunet, F. Lapierre, F. Zoueshtiagh, V. Thomy, and A. Merlen. To grate a liquid

into tiny droplets by its impact on a hydrophobic microgrid. *Applied Physics Letters*, 95, 2009. ISSN 00036951. doi: 10.1063/1.3275709.

[8] S. Chandra and C. T. Avedisian. On the collision of a droplet with a solid surface. *Proceedings of the Royal Society of London. Series A: Mathematical and Physical Sciences*, 432(1884):13–41, 1991. doi: 10.1098/rspa.1991.0002. URL https://royalsocietypublishing.org/doi/abs/10.1098/rspa.1991.0002.

[9] Yuming Chen, Rainer Mertz, and Rudi Kulenovic. Numerical simulation of bubble formation on orifice plates with a moving contact line. *International Journal of Multiphase Flow*, 35:66–77, 1 2009. ISSN 0301-9322. doi: 10.1016/J.IJMULTIPHASEFLOW.2008.07.007.

[10] K. N. Christodoulou and L. E. Scriven. Discretization of free surface flows and other moving boundary problems. *Journal of Computational Physics*, 99:39–55, 3 1992. ISSN 0021-9991. doi: 10.1016/0021-9991(92)90273-2.

[11] CHRISTOPHE Clanet, CÉDRIC BÉGUIN, DENIS RICHARD, and DAVID QUÉRÉ. Maximal deformation of an impacting drop. *Journal of Fluid Mechanics*, 517:199–208, 2004. doi: 10.1017/S0022112004000904.

[12] G E Cossali, A Coghe, and M Marengo. The impact of a single drop on a wetted solid surface, 1997.

[13] D. Deganello, A. J. Williams, T. N. Croft, A. S. Lubansky, D. T. Gethin, and T. C. Claypole. Level-set method for the modelling of liquid bridge formation and break-up. *Computers Fluids*, 40:42–51, 1 2011. ISSN 0045-7930. doi: 10.1016/J.COMPFLUID.2010.08.002.

[14] Hang Ding and Peter D.M. Spelt. Inertial effects in droplet spreading: A comparison

between diffuse-interface and level-set simulations. *Journal of Fluid Mechanics*, 576: 287–296, 2007. ISSN 14697645. doi: 10.1017/S0022112007004910.

[15] Jean Baptiste Dupont and Dominique Legendre. Numerical simulation of static and sliding drop with contact angle hysteresis. *Journal of Computational Physics*, 229: 2453–2478, 4 2010. ISSN 10902716. doi: 10.1016/j.jcp.2009.07.034.

[16] Jens Eggers, Marco A. Fontelos, Christophe Josserand, and Stéphane Zaleski. Drop dynamics after impact on a solid wall: Theory and simulations. *Physics of Fluids*, 22, 2010. ISSN 10706631. doi: 10.1063/1.3432498.

[17] Alexander I. Fedorchenko, An-Bang Wang, and Yi-Hua Wang. Effect of capillary and viscous forces on spreading of a liquid drop impinging on a solid surface. *Physics of Fluids*, 17(9):093104, 2005. doi: 10.1063/1.2038367. URL https://doi.org/10.1063/1.2038367.

[18] José Manuel Gordillo, Guillaume Riboux, and Enrique S. Quintero. A theory on the spreading of impacting droplets. *Journal of Fluid Mechanics*, 866:298–315, 5 2019. ISSN 14697645. doi: 10.1017/jfm.2019.117.

[19] Nicolas G. Hadjiconstantinou and Anthony T. Patera. A variationally consistent finite element approach to the two-fluid internal contact-line problem. *International Journal for Numerical Methods in Fluids*, 34:711–727, 12 2000. ISSN 02712091. doi: 10.1002/1097-0363(20001230)34:8<711::AID-FLD77>3.0.CO;2-5.

[20] Tommi Huhtamäki, Xuelin Tian, Juuso T. Korhonen, and Robin H.A. Ras. Surface-wetting characterization using contact-angle measurements. *Nature Protocols*, 13:1521–1538, 7 2018. ISSN 17502799. doi: 10.1038/s41596-018-0003-z.

[21] C. Josserand, L. Lemoyne, R. Troeger, and S. Zaleski. Droplet impact on a dry surface:

Triggering the splash with a small obstacle. *Journal of Fluid Mechanics*, 524:47–56, 2 2005. ISSN 00221120. doi: 10.1017/S0022112004002393.

[22] Andrzej Latka, Ariana Strandburg-Peshkin, Michelle M. Driscoll, Cacey S. Stevens, and Sidney R. Nagel. Creation of prompt and thin-sheet splashing by varying surface roughness or increasing air pressure. *Physical Review Letters*, 109, 7 2012. ISSN 00319007. doi: 10.1103/PhysRevLett.109.054501.

[23] Minhee Lee, Young Soo Chang, and Ho Young Kim. Drop impact on microwetting patterned surfaces. *Physics of Fluids*, 22:1–7, 2010. ISSN 10706631. doi: 10.1063/1.3460353.

[24] E. Q. Li and S. T. Thoroddsen. Time-resolved imaging of a compressible air disc under a drop impacting on a solid surface. *Journal of Fluid Mechanics*, 780:636–648, 9 2015. ISSN 14697645. doi: 10.1017/jfm.2015.466.

[25] Tingyi "Leo" Liu and Chang-Jin "CJ" Kim. Turning a surface superrepellent even to completely wetting liquids. *Science*, 346:1096–1100, 2014. doi: 10.1126/science.1254787. URL https://www.science.org/doi/abs/10.1126/science.1254787.

[26] James Lowndes. The numerical simulation of the steady movement of a fluid meniscus in a capillary tube. *Journal of Fluid Mechanics*, 101:631–646, 1980. ISSN 14697645. doi: 10.1017/S0022112080001838.

[27] S. Manservisi and R. Scardovelli. A variational approach to the contact angle dynamics of spreading droplets. *Computers and Fluids*, 38:406–424, 2 2009. ISSN 00457930. doi: 10.1016/j.compfluid.2008.05.001.

[28] Marco Marengo, Carlo Antonini, Ilia V. Roisman, and Cameron Tropea. Drop collisions with simple and complex surfaces, 8 2011. ISSN 13590294.

[29] Lisa Moevius, Yahua Liu, Zuankai Wang, and Julia M. Yeomans. Pancake bouncing: Simulations and theory and experimental verification. *Langmuir*, 30:13021–13032, 11 2014. ISSN 15205827. doi: 10.1021/la5033916.

[30] Chr Mundo, M Sommerfeld, and C Tropea. Droplet-wall collisions: Experimental studies of the deformation and breakup process, 1995.

[31] Metin Muradoglu and Savas Tasoglu. A front-tracking method for computational modeling of impact and spreading of viscous droplets on solid walls. *Computers and Fluids*, 39:615–625, 4 2010. ISSN 00457930. doi: 10.1016/j.compfluid.2009.10.009.

[32] Jun Kwon Park and Kwan Hyoung Kang. Numerical analysis of moving contact line with contact angle hysteresis using feedback deceleration technique. *Physics of Fluids*, 24, 4 2012. ISSN 10706631. doi: 10.1063/1.4707703.

[33] M. Pasandideh-Fard, Y. M. Qiao, S. Chandra, and J. Mostaghimi. Capillary effects during droplet impact on a solid surface. *Physics of Fluids*, 8(3):650–659, 1996. ISSN 10706631. doi: 10.1063/1.868850.

[34] Andrea Pros and Hasan N Oguz. The impact of drops on liquid surfaces and the underwater noise of rain, 1993. URL www.annualreviews.org.

[35] Kai Range and François Feuillebois. Influence of Surface Roughness on Liquid Drop Impact. *Journal of Colloid and Interface Science*, 203(1):16–30, 7 1998. ISSN 0021-9797. doi: 10.1006/JCIS.1998.5518.

[36] Michael Renardy, Yuriko Renardy, and Jie Li. Numerical simulation of moving contact line problems using a volume-of-fluid method. *Journal of Computational Physics*, 171 (1):243–263, 2001. ISSN 0021-9991. doi: https://doi.org/10.1006/jcph.2001.6785. URL https://www.sciencedirect.com/science/article/pii/S0021999101967853.

[37] Y. Renardy, S. Popinet, L. Duchemin, M. Renardy, S. Zaleski, C. Josserand, M. A. Drumright-Clarke, D. Richard, C. Clanet, and D. Quéré. Pyramidal and toroidal water drops after impact on a solid surface. *Journal of Fluid Mechanics*, 484:69–83, 6 2003. ISSN 00221120. doi: 10.1017/S0022112003004142.

[38] M. Reyssat, F. Pardo, and D. Quéré. Drops onto gradients of texture. *EPL*, 87, 8 2009. ISSN 12864854. doi: 10.1209/0295-5075/87/36003.

[39] Guillaume Riboux and José Manuel Gordillo. Erratum: Experiments of drops impacting a smooth solid surface: A model of the critical impact speed for drop splashing (physical review letters (2014) 113 (024507)), 10 2014. ISSN 10797114.

[40] R. Rioboo, M. Marengo, and C. Tropea. Time evolution of liquid drop impact onto solid, dry surfaces. *Experiments in Fluids*, 33:112–124, 2002. ISSN 07234864. doi: 10.1007/s00348-002-0431-x.

[41] Romain Rioboo, Marco Marengo, and Cameron Tropea. Outcomes from a drop impact on solid surfaces. *ATOMIZATION AND SPRAYS*, 11:155–166, 03 2001. doi: 10.1615/AtomizSpr.v11.i2.40.

[42] I. V. Roisman, L. Opfer, C. Tropea, M. Raessi, J. Mostaghimi, and S. Chandra. Drop impact onto a dry surface: Role of the dynamic contact angle. *Colloids and Surfaces A: Physicochemical and Engineering Aspects*, 322:183–191, 6 2008. ISSN 09277757. doi: 10.1016/j.colsurfa.2008.03.005.

[43] Ilia V. Roisman. Inertia dominated drop collisions. ii. an analytical solution of the navier-stokes equations for a spreading viscous film. *Physics of Fluids*, 21, 2009. ISSN 10706631. doi: 10.1063/1.3129283.

[44] Ilia V. Roisman, Romain Rioboo, and Cameron Tropea. Normal impact of a liquid

drop on a dry surface: Model for spreading and receding. *Proceedings of the Royal Society A: Mathematical, Physical and Engineering Sciences*, 458:1411–1430, 6 2002. ISSN 13645021. doi: 10.1098/rspa.2001.0923.

[45] Ilia V. Roisman, Andreas Lembach, and Cameron Tropea. Drop splashing induced by target roughness and porosity: The size plays no role, 8 2015. ISSN 00018686.

[46] R. P. Sahu, S. Sett, A. L. Yarin, and B. Pourdeyhimi. Impact of aqueous suspension drops onto non-wettable porous membranes: Hydrodynamic focusing and penetration of nanoparticles. *Colloids and Surfaces A: Physicochemical and Engineering Aspects*, 467:31–45, 2 2015. ISSN 0927-7757. doi: 10.1016/J.COLSURFA.2014.11.023.

[47] Brian L. Scheller and Douglas W. Bousfield. Newtonian drop impact with a solid surface. *AIChE Journal*, 41:1357–1367, 1995. ISSN 15475905. doi: 10.1002/aic.690410602.

[48] Stefano Schiaffino and Ain A. Sonin. Molten droplet deposition and solidification at low weber numbers. *Physics of Fluids*, 9:3172–3187, 1997. ISSN 10706631. doi: 10.1063/1.869434.

[49] Thomas M. Schutzius, Gustav Graeber, Mohamed Elsharkawy, James Oreluk, and Constantine M. Megaridis. Morphing and vectoring impacting droplets by means of wettability-engineered surfaces. *Scientific Reports*, 4:7029, 2014. ISSN 20452322. doi: 10.1038/srep07029.

[50] David N. Sibley, Andreas Nold, Nikos Savva, and Serafim Kalliadasis. The contact line behaviour of solid-liquid-gas diffuse-interface models. *Physics of Fluids*, 25, 9 2013. ISSN 10706631. doi: 10.1063/1.4821288.

[51] S. Sikalo, Marco Marengo, Cameron Tropea, and E. N. Ganic. Analysis of impact of

droplets on horizontal surfaces. pages 347–352. Begell House, 3 2001. doi: 10.1615/ichmt.2000.thersieprocvol2thersieprocvol1.460.

[52] Jacco H. Snoeijer and Bruno Andreotti. Moving contact lines: Scales, regimes, and dynamical transitions, 1 2013. ISSN 00664189.

[53] Peter D.M. Spelt. A level-set approach for simulations of flows with multiple moving contact lines with hysteresis. *Journal of Computational Physics*, 207(2):389–404, 2005. ISSN 0021-9991. doi: https://doi.org/10.1016/j.jcp.2005.01.016. URL https://www.sciencedirect.com/science/article/pii/S0021999105000343.

[54] Cacey S. Stevens. Scaling of the splash threshold for low-viscosity fluids. *EPL*, 106, 2014. ISSN 12864854. doi: 10.1209/0295-5075/106/24001.

[55] Y. Sui and Peter D.M. Spelt. An efficient computational model for macroscale simulations of moving contact lines. *Journal of Computational Physics*, 242:37–52, 6 2013. ISSN 0021-9991. doi: 10.1016/J.JCP.2013.02.005.

[56] Chijioke Ukiwe and Daniel Y. Kwok. On the maximum spreading diameter of impacting droplets on well-prepared solid surfaces. *Langmuir*, 21(2):666–673, 2005. doi: 10.1021/la0481288. URL https://doi.org/10.1021/la0481288. PMID: 15641837.

[57] D. C. Vadillo, A. Soucemarianadin, C. Delattre, and D. C. D. Roux. Dynamic contact angle effects onto the maximum drop impact spreading on solid surfaces. *Physics of Fluids*, 21(12):122002, 2009. doi: 10.1063/1.3276259. URL https://doi.org/10.1063/1.3276259.

[58] Randy L. Vander Wal, Gordon M. Berger, and Steven D. Mozes. The splash/non-splash boundary upon a dry surface and thin fluid film. *Experiments in Fluids*, 40:53–59, 1 2006. ISSN 07234864. doi: 10.1007/s00348-005-0045-1.

[59] Mark C.T. Wilson, Jonathan L. Summers, Yulii D. Shikhmurzaev, Andrew Clarke, and Terence D. Blake. Nonlocal hydrodynamic influence on the dynamic contact angle: Slip models versus experiment. *Physical Review E - Statistical, Nonlinear, and Soft Matter Physics*, 73, 2006. ISSN 15393755. doi: 10.1103/PhysRevE.73.041606.

[60] Lei Xu, Wendy W. Zhang, and Sidney R. Nagel. Drop splashing on a dry smooth surface. *Physical Review Letters*, 94, 5 2005. ISSN 10797114. doi: 10.1103/PhysRevLett.94.184505.

[61] Lei Xu, Loreto Barcos, and Sidney R. Nagel. Splashing of liquids: Interplay of surface roughness with surrounding gas. *Physical Review E*, 76, 12 2007. ISSN 1539-3755. doi: 10.1103/physreve.76.066311.

[62] A L Yarin. Drop impact dynamics: Splashing, spreading, receding, bouncing.... 2006. doi: 10.1146/annurev.fluid. URL www.annualreviews.org.

[63] Yong Han Yeong, James Burton, Eric Loth, and Ilker S. Bayer. Drop impact and rebound dynamics on an inclined superhydrophobic surface. *Langmuir*, 30:12027–12038, 10 2014. ISSN 15205827. doi: 10.1021/la502500z.

[64] Kensuke Yokoi. Numerical studies of droplet splashing on a dry surface: Triggering a splash with the dynamic contact angle. *Soft Matter*, 7:5120–5123, 6 2011. ISSN 1744683X. doi: 10.1039/c1sm05336a.

[65] Kensuke Yokoi, Damien Vadillo, John Hinch, and Ian Hutchings. Numerical studies of the influence of the dynamic contact angle on a droplet impacting on a dry surface. *Physics of Fluids*, 21, 2009. ISSN 10706631. doi: 10.1063/1.3158468.

[66] Pengtao Yue and James J. Feng. Wall energy relaxation in the cahn-hilliard model for

moving contact lines. *Physics of Fluids*, 23, 1 2011. ISSN 10706631. doi: 10.1063/1.3541806.

[67] Š Šikalo, H. D. Wilhelm, I. V. Roisman, S. Jakirlić, and C. Tropea. Dynamic contact angle of spreading droplets: Experiments and simulations. *Physics of Fluids*, 17:1–13, 2005. ISSN 10706631. doi: 10.1063/1.1928828.

Appendices

Appendix A

Simulation Set-up

A sample simulation set-up is explained in brief to understand the procedure involved. A step-by-step guide is given for each sub-element in the simulation tree to aid the user.

Model Geometry

The first step is to model the geometry - consisting of two specific parts as part of the domain. The two parts include the Drop zone and the Splash zone for which the dimensions are specified. For example in figures A.2 and A.3, the dimensions are specified as functions of the droplet diameter.

Simulation Physics

The simulation continua involves the setting up of the physical parameters influencing the simulation. Here, the various different models in use are incorporated as seen in figure A.4

Most models utilize default parametric setup, the main focus here is on the Adaptive mesh, adaptive time-step and Volume of Fluid models. The set-up for the adaptive mesh model is shown in figure A.5, where the refinement level and minimum adaptation cell size are the major parameters affecting the simulation.

The set-up for the adaptive time-step model is shown in figure A.6. The time-step is defined

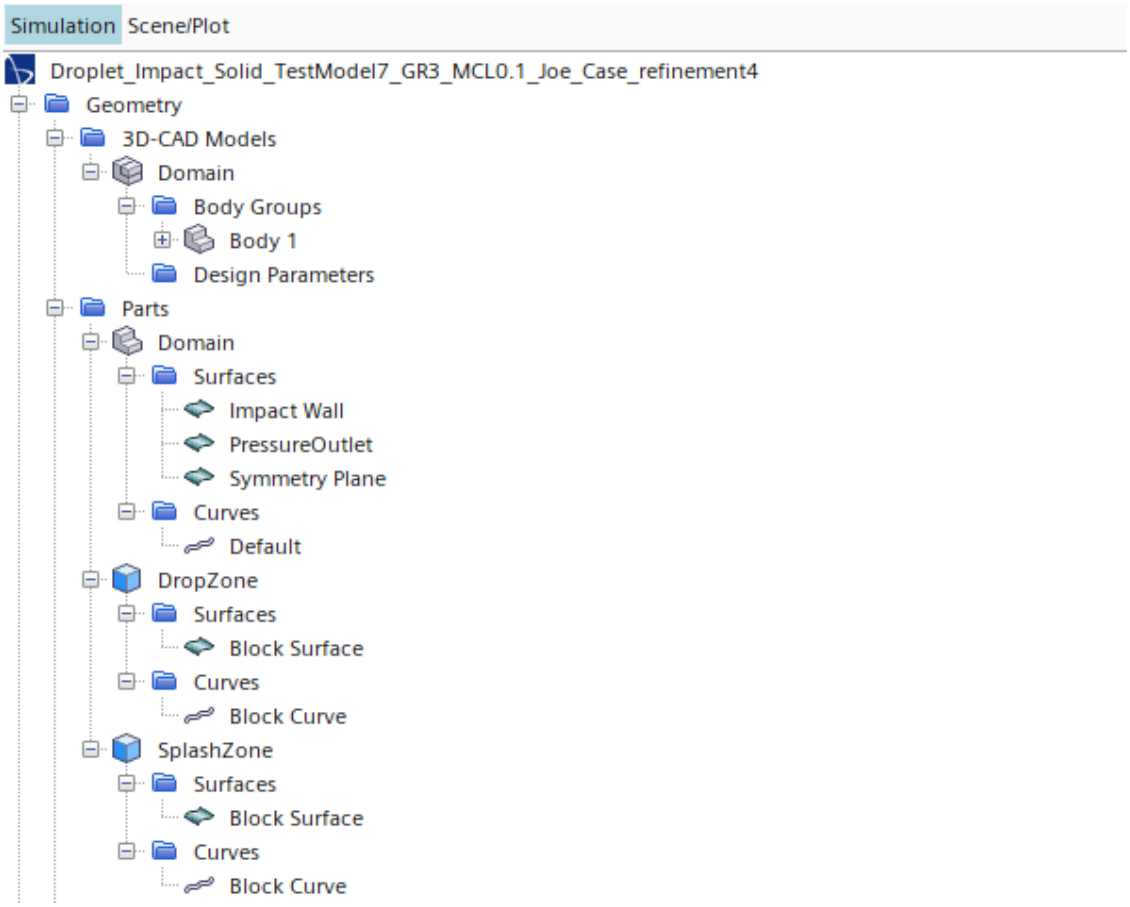

Figure A.1: Image showing the tree for geometry of the model

by the CFL condition and varied with the help of the Max. condition limit parameter. The multiphase equation of state model defines the interfacial artificial viscosity and the surface tension as seen in figure A.7 - an important material property for the simulation.

The volume of fluid model helps in tracking the interface and the motion of the droplet. The model involves the use of the High Resolution Interface Capturing scheme that solves the VOF function. The setup for the VOF model is seen in figure A.8

The next step is to set-up the reference conditions for the solver. This is done by setting the values for gravity, max. allowable absolute pressure, min. allowable absolute pressure, reference altitude, reference density and reference pressure as seen in figure A.9 The physics

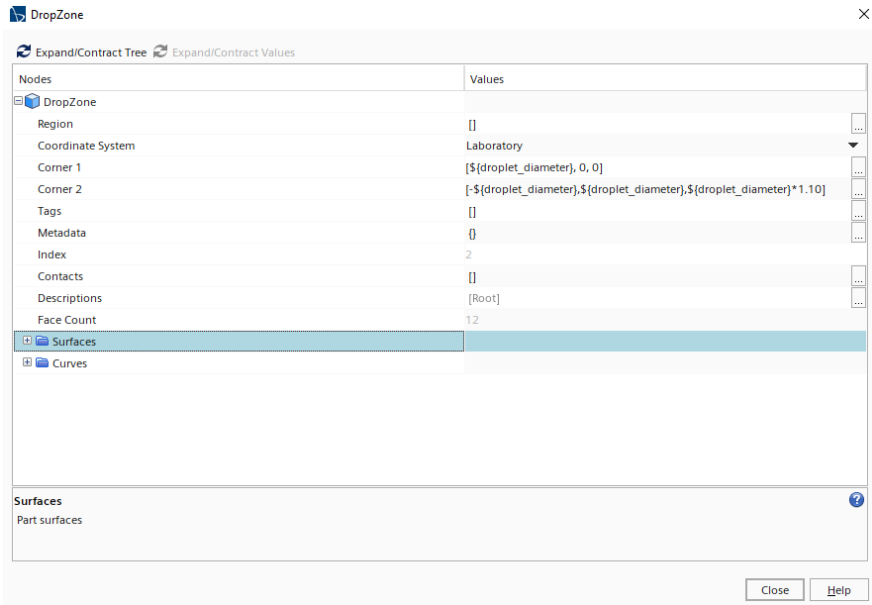

Figure A.2: Image showing the different input parameters required in defining the drop zone

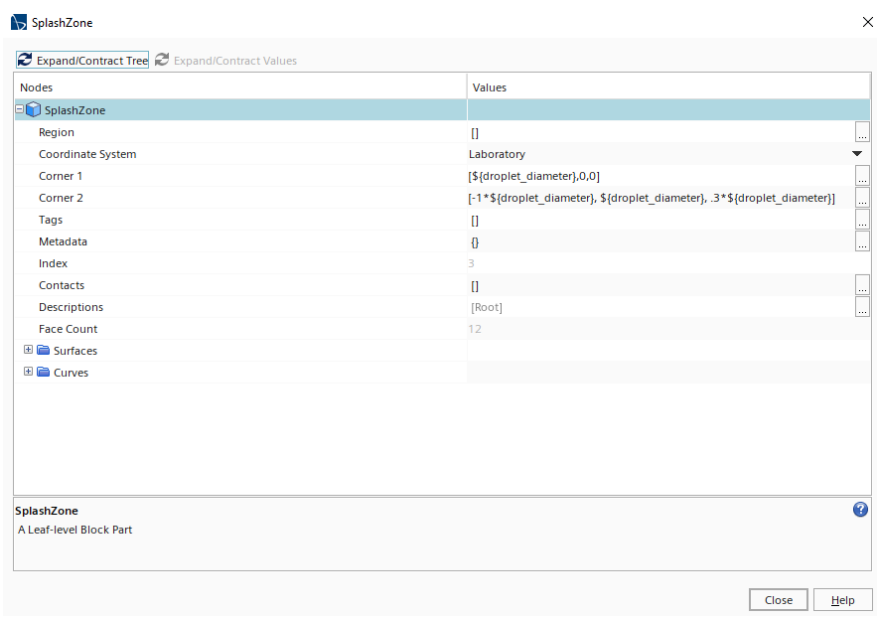

Figure A.3: Image showing the different input parameters required in defining the splash zone

setup is concluded with the setting up of the initial conditions as seen in figure A.10

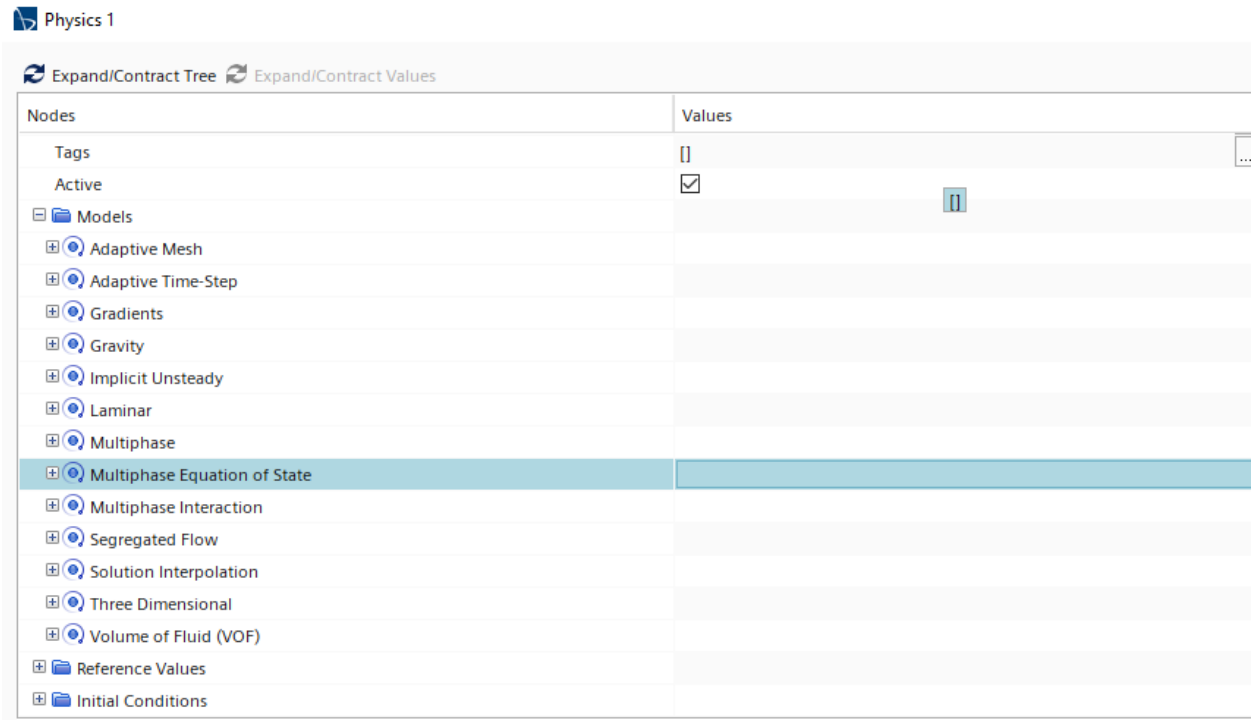

Figure A.4: Image showing the different steps in setting up the model

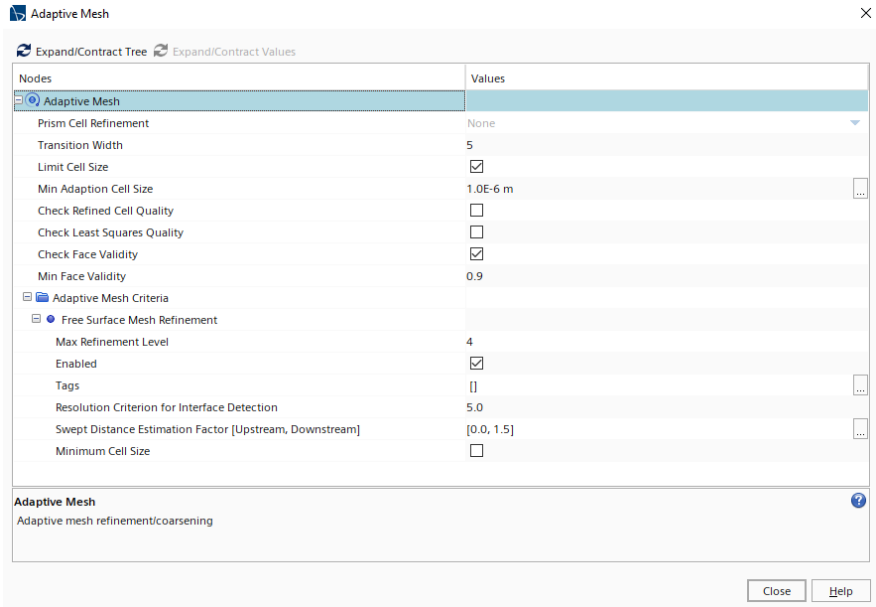

Figure A.5: Image shows the setup for an adaptive mesh model

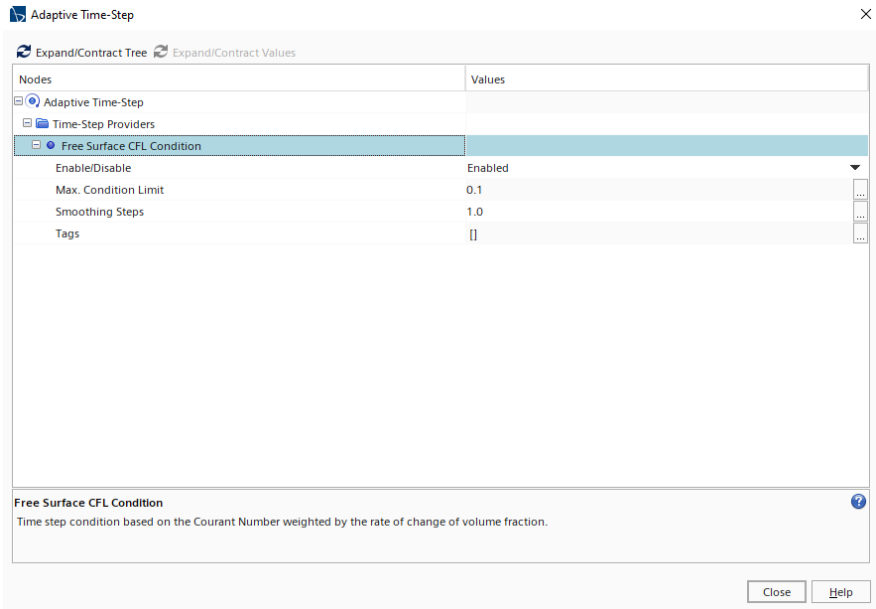

Figure A.6: Image shows the setup for an adaptive time-step model

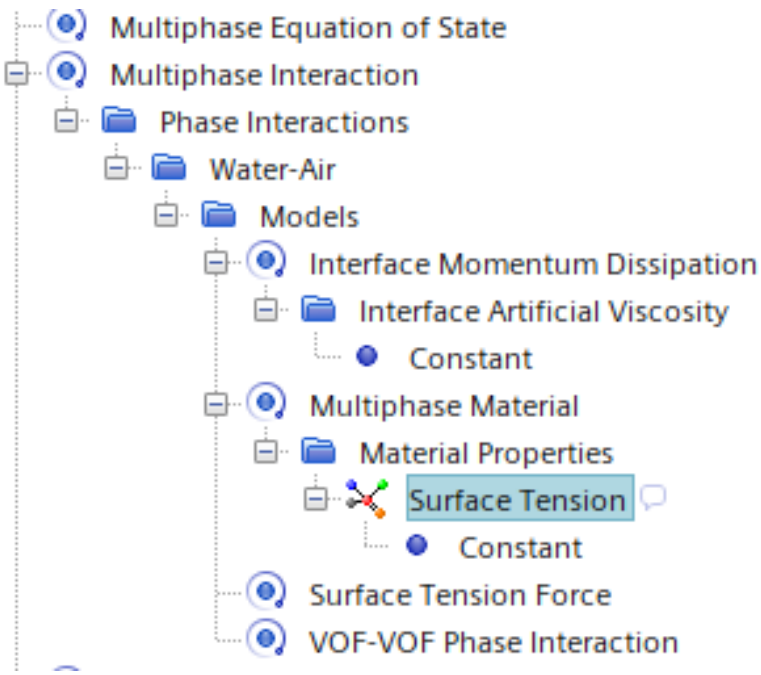

Figure A.7: Image shows the setup for the multiphase equation of state model

Regions

Setting up the region involves definition of the contact angle at the interface. ACA, RCA, equilibrium contact angle and capillary number are the inputs for setting up the blended

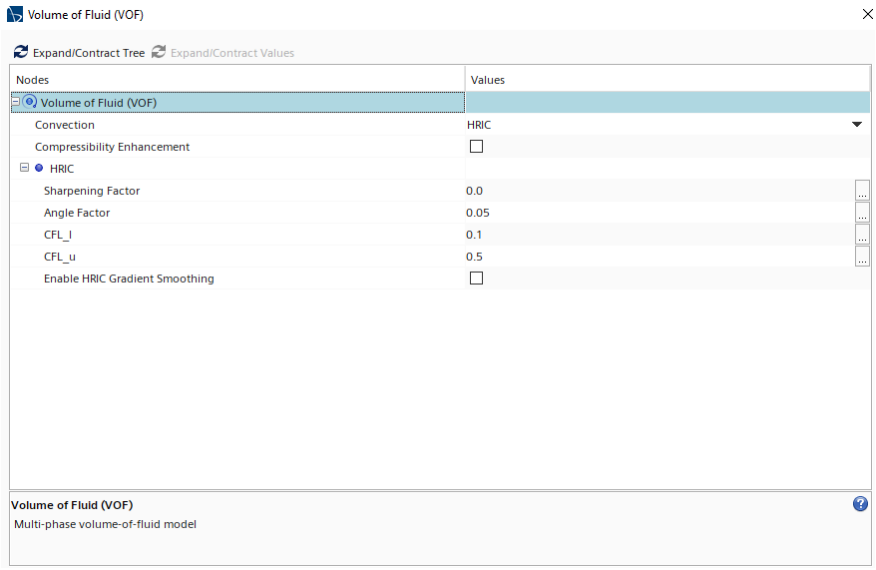

Figure A.8: Image shows the setup for the volume of fluid model

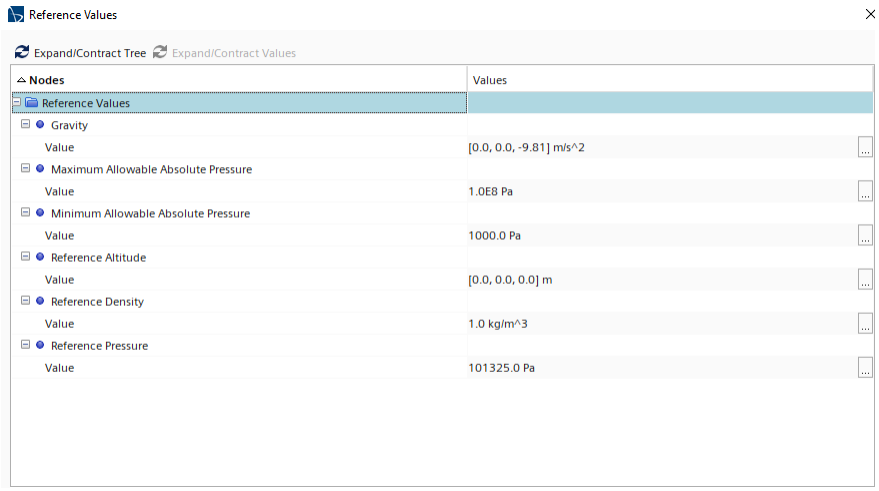

Figure A.9: Image shows the definition of the reference parameters

Kistler model as seen in figure A.11

Default settings are incorporated throughout all other sub-elements except the physics conditions, where the shear stress is specified as the No-Slip method.

Initial Conditions

Expand/Contract Tree Expand/Contract Values

Nodes	Values
Pressure	
Method	Constant
Value	0.0 Pa
Dimensions	Pressure
Velocity	
Method	Composite
Dimensions	Velocity
Coordinate System	Laboratory
Composite	
X Component	
Y Component	
Z Component	
Method	Constant
Value	-1*${impact_velocity}
Dimensions	Velocity
Volume Fraction	
Method	Composite
Dimensions	Dimensionless

Figure A.10: Image shows the definition of the initial conditions

Regions

Expand/Contract Tree Expand/Contract Values

Nodes	Values
Allow Per-Surface Values	☐
Phase Conditions	
Water-Air	
Type	Wall
Tags	[]
Physics Values	
Contact Angle	
Method	Blended Kistler
Dimensions	Angle
Blended Kistler	
Equilibrium Contact Angle	90.0 deg
Equilibrium Capillary Number	0.001
Advancing/Receding	
Advancing Contact Angle	147.99 deg
Receding Contact Angle	146.37 deg
Physics Conditions	
Domain.PressureOutlet	
Index	2

Contact Angle
Contact angle profile

Figure A.11: Image shows the definition of the contact angle modeling

Derived Parts

The derived parts involve the specification of the threshold values between the interface. Defining the thresholds for volume fraction and velocity magnitudes as seen in figure A.12.

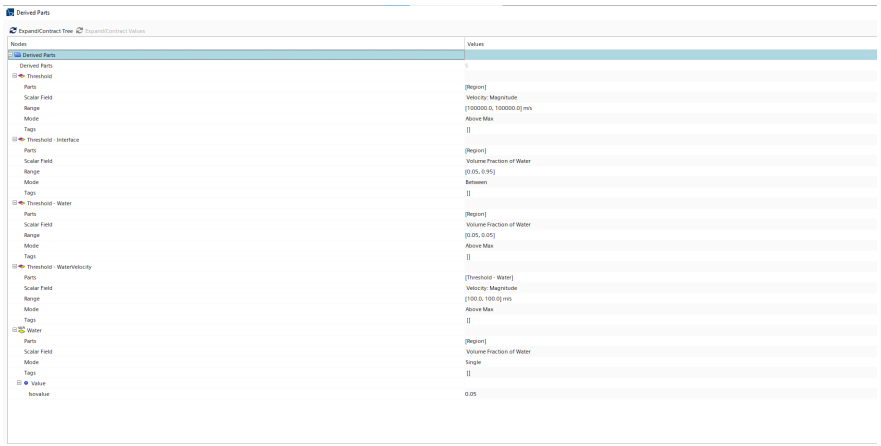

Figure A.12: Image shows the definition of the thresholds defined in the derived parts

Solvers

Implicit unsteady, adaptive time-stepping, adaptive meshing, partitioning, segregated flow, segregated VOF and multi-stepping are the different solvers that are coupled together to solve this interfacial problem of droplet impact.

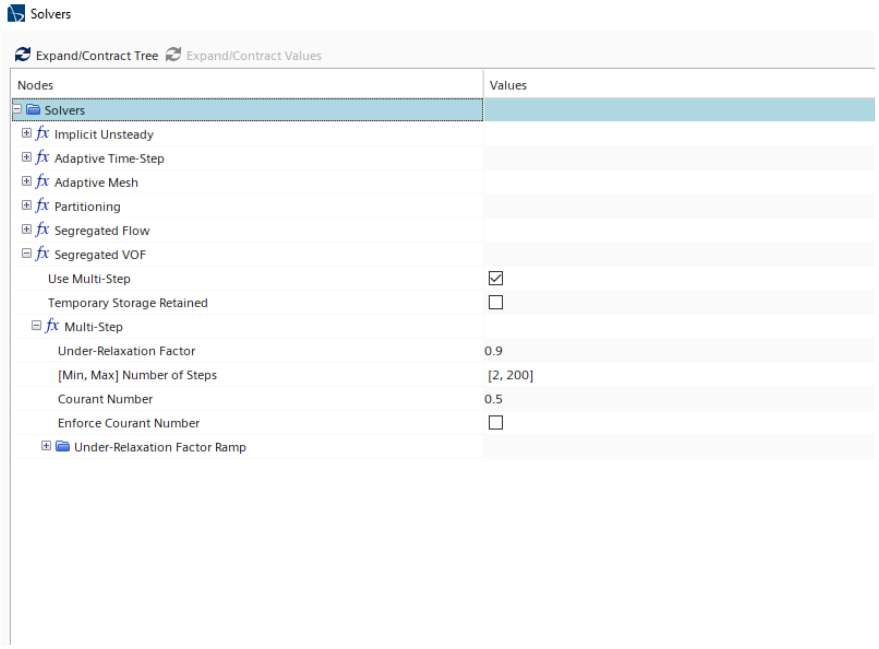

Figure A.13: Image shows the definition of the VOF and multi-stepping methods

The image above in figure A.13 shows the use of the segregated VOF function and the multi-step function. Multi-stepping in enabled with an under-relaxation factor of 0.9 and defined within a range of 2 to 200 steps.

Stopping Criteria

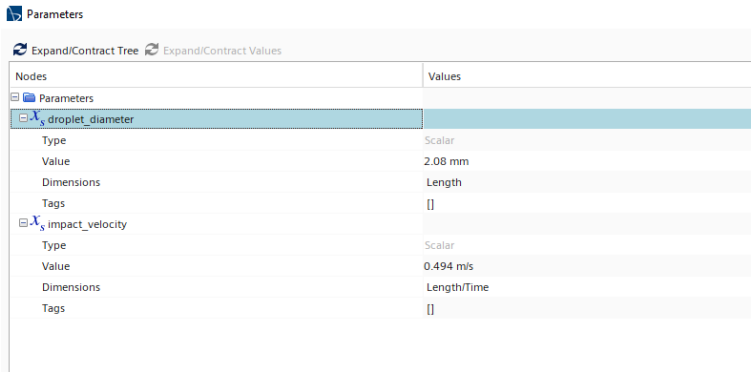

Figure A.14: Image shows the definition of the droplet parameters

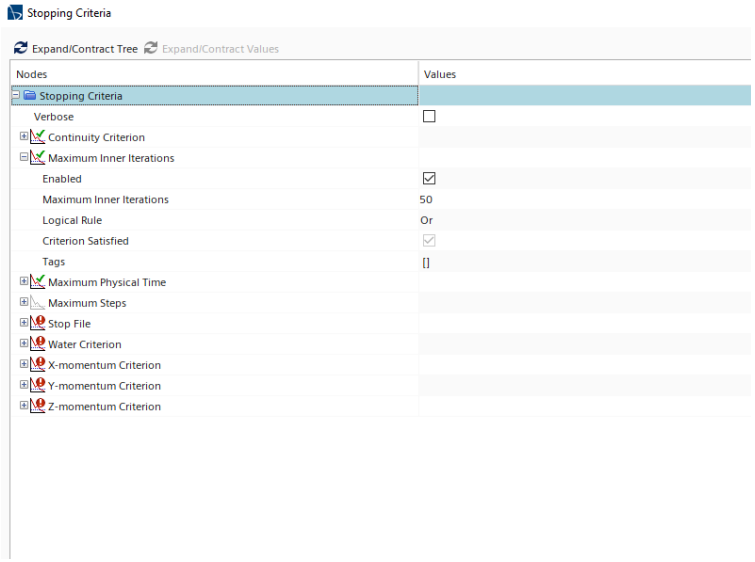

Figure A.15: Image shows the definition of the maximum inner iterations as part of the stopping criterion

The final step in setting up the simulation, involves the specification of the stopping criteria that defines the logic conditions and upper limits to decide when the solver must advance a

time-step or stop the simulation. The model solves the continuity equation, x-momentum, y-momentum, z-momentum and the water criterion. Convergence criteria with a minimum limit of 10^{-4} is set for all parameters with an AND logic gate, meaning all parameters must converge to a minimum value of 10^{-4} for the simulation to proceed to the next time-step. The droplet diameter and velocity are defined in the parameters tab found under the tools sub-section of the tree as seen in figure A.15. The maximum inner iterations acts as an OR condition, meaning the simulation must move on to the next time step every 50 inner iterations regardless of the convergence of the governing equations. The stopping criterion plays a major role in defining the ability of the model to solve the equations and converge to the most accurate solution. This concludes a basic set-up for the simulation.

Appendix B

Appendix B

B.1 Mistakes to Avoid

During the course of the setting up of the model and experimentation, there were plenty of roadblocks with information that is not available regarding the background of the solver, effectiveness of the experimental set-up and design. Multiple parameters were to be captured, which increased the complexity of the result gathering, post-processing and simulation of the droplet impact behavior. General mistakes to be avoided in future include - Firstly, it is important to understand the basics of the equations involved and their parameters that can affect the outcome of the simulation. It is highly recommended that the StarCCM+ tutorial be completely read through, for understanding the effective use of the governing equations.

Secondly, from a Simulation point of view, it is crucial that setup parameters must not all be altered at once, verification must be conducted on the parameters being varied and their overall effect on the simulation must be noted down. This will help quantify any mistakes in the simulation and also portray how dominant the effect of minor variations in certain parameters are on the results obtained from the simulation.

Furthermore, techniques used in post-processing results must be validated with conventional methods or the literature. This would help in avoiding any post-processing errors that are difficult to quantify as generally the source is unknown. It becomes even more important to

perform an analysis for the uncertainties involved in measurements, that will help quantify the errors that might be present in the results.

Lastly, it is recommended that the experiments be performed at controlled environments with constant physical parametric properties for the fluid and substrate. This will avoid errors in calculation of the input parameters for the numerical simulation, which will play a major role in how the solver interprets the behavior and will eventually lead to a propagation of error (if any), leading to discrepancy in results.